21807

NATIONAL LIBRARY
OTTAWA

CANADA

BIBLIOTHÈQUE NATIONALE
OTTAWA

NAME OF AUTHOR.....Moustafa Abdel Salam EL-Gabaly

TITLE OF THESIS....Exact Study on MSM Baritt diodes

UNIVERSITY.....Alberta

DEGREE FOR WHICH THESIS WAS PRESENTED.....Ph.D.

YEAR THIS DEGREE GRANTED.....1974

Permission is hereby granted to THE NATIONAL LIBRARY OF CANADA to microfilm this thesis and to lend or sell copies of the film.

The author reserves other publication rights, and neither the thesis nor extensive extracts from it may be printed or otherwise reproduced without the author's written permission.

(Signed).....M. A.S. Elgabaly

PERMANENT ADDRESS:
544 Michener Park
Edmonton, Alberta
Canada

DATED.....Oct 11, 1974.....1974

NL-91 (10-68)

THE UNIVERSITY OF ALBERTA

EXACT STUDY ON MSM BARITT DIODES

by

© MOUSTAFA A.S. EL-GABALY

A THESIS

SUBMITTED TO THE FACULTY OF GRADUATE STUDIES AND

RESEARCH IN PARTIAL FULFILMENT OF THE REQUIREMENTS FOR

THE DEGREE OF DOCTOR OF PHILOSOPHY

DEPARTMENT OF ELECTRICAL ENGINEERING

EDMONTON, ALBERTA

FALL, 1974

THE UNIVERSITY OF ALBERTA

FACULTY OF GRADUATE STUDIES AND RESEARCH

The undersigned certify that they have read, and recommend to the Faculty of Graduate Studies and Research, for acceptance, a thesis entitled EXACT STUDY ON MSM BARITT DIODES submitted by Moustafa A.S. El-Gabaly in partial fulfilment of the requirements for the degree of Doctor of Philosophy.

.....
Supervisor

.....
Supervisor

.....

.....

.....

.....

.....

.....
External Examiner

Date October 11 1974

ABSTRACT

The dc and small-signal characteristics of MSM Baritt diodes are investigated theoretically. The physical processes affecting the charge transport in MSM structures are studied from the diffusion theory point of view. The boundary conditions used for this study are derived from thermionic emission theory. A numerical model of MSM structures, which takes into account a realistic dependence of carrier drift velocity upon electric field and doping concentration, is applied to PtSi-nSi-PtSi Baritt diodes. The computed results are found to be in close agreement with the available experimental data.

For current densities exceeding 10 A cm^{-2}, the physical conditions of the injecting contact, and carrier diffusion in the injection and low-field regions of the structure are shown to affect significantly the electrical behavior of MSM Baritt diodes. At microwave frequencies, Baritt diodes are found to exhibit negative conductance over nearly an octave frequency range. The negative quality factor is shown to be relatively large in comparison with that of Impatt and Gunn diodes. The electronic susceptance is a small fraction of the total device susceptance and changes from inductive to capacitative over the negative conductance region.

It is shown that MSM Baritt structures with a semiconductor width between 4 and 10 μm, with doping concentration between 4×10^{14} and 4×10^{15} cm^{-3}, exhibit maximum negative conductance in the frequency range from 2 to 15 GHz and require a bias voltage from 4 to 100 Volts. The microwave behavior of Baritt diodes is affected

significantly by reducing the semiconductor width and only slightly by changing the doping concentration. Above room temperature, the microwave performance of MSM structures is greatly degraded; the maximum negative conductance reduces in magnitude and shifts to lower frequencies, and the active frequency interval becomes narrower. Based on these results, design data for Baritt oscillators is given.

ACKNOWLEDGMENT

The author wishes to express his appreciation for the assistance of many people during the course of this work:

To Dr. W.A.G. Voss and Dr. J. Nigrin under whose supervision this work has been completed, for their invaluable advice, encouragement and guidance.

To Dr. P.A. Goud, for his assistance and guidance during the period of his supervision.

To Dr. C.G. Englefield, Dr. R.P.W. Lawson, Dr. B.V. Paranjape, Dr. A.M. Robinson, Dr. D. Routledge and Dr. P.R. Smy for serving on the doctoral committee.

To Mr. C.M.B. Walker and Dr. H.K. Chaurasia for their help and patience in reading the manuscript.

To Mrs. M.K. Mounteer, for her excellent work in typing this thesis.

To members of the Microwave Group for their helpful discussions, understanding, and encouragement.

The author also thanks his wife, Nagwa for her patience, encouragement and help.

Appreciation is also extended to the following organizations: to the Faculty of Engineering, the University of Al-Azhar, Cairo, Egypt, for enabling the author to study at the University of Alberta; the Department of Electrical Engineering; the National Research Council of Canada for a postgraduate scholarship and the University of Alberta for an additional award.

TABLE OF CONTENTS

		Page
I	INTRODUCTION	1
	1.1 Historical Background	1
	1.2 Objective of the Present Study	6
	1.3 Organization of this Thesis	8
II	METAL-SEMICONDUCTOR (SCHOTTKY BARRIER) CONTACTS	9
	2.1 Energy Band Relations at an Ideal MS Contact	9
	2.2 Current Transport in Schottky Barriers made on Lightly Doped Materials	15
	2.2.1 Basic Theories	15
	2.2.2 Thermionic Emission-Diffusion Theory	19
III	CHARGE TRANSPORT IN MSM STRUCTURES	26
	3.1 Energy Band Diagram and Charge Distribution	26
	3.2 Stationary Charge Transport	29
	3.3 Basic Dynamic Equations	40
IV	BOUNDARY CONDITIONS	43
	4.1 Simplified Boundary Conditions	43
	4.2 Current-Dependent Boundary Concentrations	45
V	MATHEMATICAL MODEL AND NUMERICAL SOLUTION	57
	5.1 Mathematical Model	57
	5.2 Limitation of Analytical Solutions	60
	5.3 DC and Small-Signal Boundary-Value Problems	61
	5.4 Numerical Techniques for the Solution of Boundary-Value Problems	63
	5.5 Outline of the Numerical Method	66

5.6 Approximate Small-Signal Numerical Solution 72

5.7 Summary 76

VI STATIC CHARACTERISTICS 78

6.1 DC Properties and J-V Characteristics of a Typical MSM Structure 78

6.2 Effects of Physical Parameters 90

6.3 Temperature Effects on the DC Properties of the MSM Structure 96

VII SMALL-SIGNAL PROPERTIES OF MSM STRUCTURES 103

7.1 Small-Signal Impedance 103

7.2 Small-Signal Charge Transport Properties 105

7.3 Power Dissipation Inside the MSM Structure 118

VIII SMALL-SIGNAL ADMITTANCE OF MSM STRUCTURES 126

8.1 Small-Signal Admittance of an MSM Structure 126

8.2 Temperature-Dependence of the Small-Signal Admittance 133

8.3 Effects of the Physical Parameters on the Small-Signal Behavior 137

IX COMPARISON OF VARIOUS MODELS AND MEASURED DATA 155

X SUMMARY AND CONCLUSIONS 163

REFERENCES 167

APPENDIX A ACCURACY AND STABILITY OF THE NUMERICAL SOLUTION (USING INITIAL-VALUE METHODS) 174

LIST OF TABLES

		Page
TABLE 6.1	Summary of Structure Parameters Used for the DC Study	79
TABLE 8.1	Summary of Structure Parameters Used for the Small-Signal Analysis	127

LIST OF FIGURES

		Page
Fig. 2.1a	Energy Band Diagram of an MS Contact at Thermal Equilibrium	11
Fig. 2.1b	Corresponding Charge Distribution	11
Fig. 2.2	Energy Band Diagram of an MS Contact Under Different Biasing Conditions	14
Fig. 2.3	Electron Potential Energy (ψ) Versus Distance for an MS Barrier	20
Fig. 3.1a	Schematic Diagram of an MSM Structure	27
Fig. 3.1b	Corresponding Energy Band Diagram at Thermal Equilibrium	27
Fig. 3.1c	Corresponding Mobile Charge Distribution	27
Fig. 3.2a	Energy Band Diagram of an MSM Structure Biased Below Punch-Through Voltage	30
Fig. 3.2b	Corresponding Concentration Profile of Mobile Holes and Electrons	30
Fig. 3.3	Energy Band Diagram of an MSM Structure Under Flat Band Condition	31
Fig. 4.1	Flux Interchange at the Interfacial Boundary Layer	46
Fig. 5.1	One Dimensional MSM Structure	58
Fig. 5.2	Overall Iterative Scheme for DC Calculations	67
Fig. 5.3	Overall Iterative Procedure for Small-Signal AC Calculations	69

Fig. 6.1a	Concentration Profile of the Injected Mobile Holes in the Semiconductor Region for Two Different Doping Concentrations	81
Fig. 6.1b	Corresponding Electric Field Distribution	82
Fig. 6.2a	Drift and Diffusion Current Components (Normalized to the Total Current J_T) in the Barrier Region of the Injecting Contact, at Two Different Temperatures	84
Fig. 6.2b	Corresponding Potential Energy Distribution	85
Fig. 6.3a	Current-Voltage Characterisitics for Two Different Doping Concentrations and at Two Different Crystal Temperatures (L = 4 μm). Effect of Ignoring Space Charge of Injected Holes is also shown.	88
Fig. 6.3b	Current-Voltage Characteristics for Two Different Doping Concentrations and at Two Different Crystal Temperatures (L = 10 μm).	89
Fig. 6.4	Current-Voltage Characteristics for Structures A, B, C and D	92
Fig. 6.5	Punch-Through Voltage V_p Versus Doping Concentration N_D, With Semiconductor Width L as a Parameter	95
Fig. 6.6a	Concentration Profile of the Injected Mobile Holes in the Semiconductor Region at Two Different Crystal Temperatures	98
Fig. 6.6b	Corresponding Electric Field Distribution	99

Fig. 7.1	Equivalent Small-Signal Circuit of Punch-Through MSM Structure for Relatively Low (Left) and High (Right) Frequency Ranges	106
Fig. 7.2	Phasor Diagram of Various Components of the AC Conduction Current Density $\tilde{J}_c$ (Normalized to the Total AC Current $\tilde{J}_T$). $\tilde{J}_T$ Lies on the Positive Real Axis	108
Fig. 7.3	Space Charge Distribution of Injected Holes at Various Time Instants During One Cycle of Operation	110
Fig. 7.4	Propagation of Conduction Current Wave at Various Time Instants During One Cycle of Operation	111
Fig. 7.5	Distribution of Space Charge Amplitude of AC Hole Concentration in the Vicinity of the Injecting Contact	115
Fig. 7.6	Phasor Diagram of AC Electric Field $\tilde{E}$ and AC Conduction Current $\tilde{J}_c$ (Normalized to the Total AC Current Density $\tilde{J}_T$). $\tilde{J}_T$ Lies on the Positive Real Axis	117
Fig. 7.7	Spatial Variation of DC Power Dissipation	121
Fig. 7.8	Spatial Variation of AC Power Dissipation Corresponding to Various Components of the AC Conduction Current	124
Fig. 8.1	Admittance Chart of Structure C, for Different Current Densities	128

Fig. 8.2 Frequency-Dependence of the Small-Signal Conductance, G and Normalized Susceptance of Structure C, for Different Current Densities 130

Fig. 8.3 Frequency-Dependence of the Small-Signal Device Conductance and Normalized Susceptance of Structure B, for Two Different Temperatures 135

Fig. 8.4 Frequency-Dependence of the Small-Signal Device Conductance of Structure A, for Two Different Temperatures 138

Fig. 8.5 Constant Frequency, Small-Signal Conductance, G Versus Current Density for Structures A, B, C and D 140

Fig. 8.6 Minimum Negative Quality Factor Versus Current Density, for Structures A, B, C and D 142

Fig. 8.7 Frequency Dependence of the Small-Signal Conductance of Real (Dashed Curves) and Ideal (Solid Curves) Structures A, B, C and D 144

Fig. 8.8 Frequency Dependence of the Small-Signal Resistance and the Negative Quality Factor for Structures A, B, C and D 145

Fig. 8.9 Frequency Dependence of the Normalized Structure Susceptance for Structures A, B, C and D 147

Fig. 8.10 Frequency Dependence of Negative Conductance for Four Structures Having the Same Doping Concentration and Differing in Semiconductor Width 148

Fig. 8.11 Frequency Dependence of the Negative Conductance for Three Structures (L = 4.8 μm) Which Differ in Doping Concentration 149

Fig. 8.12 Small-Signal Conductance Versus the Structure Width L, with Fixed Doping Concentration $N_D = 1.2 \times 10^{15} cm^{-3}$ 151

Fig. 8.13 Small-Signal Conductance Versus Doping Concentration N_D, with Fixed Width L = 4.8 μm 152

Fig. 9.1a Small-Signal Device Conductance as a Function of Frequency 157

Fig. 9.1b Small-Signal Device Resistance as a Function of Frequency 158

Fig. 9.2 The Normalized Difference $\frac{\Delta G_p}{G_p}$ as a Function of Current Density. ΔG_p is the Difference Between the Negative Conductance Computed From the Exact Model, G_p, and that Obtained From Various Simplified Models 161

CHAPTER I

INTRODUCTION

1.1 Historical Background

In recent years, the use of semiconductor devices in microwave communications has increased significantly. Two important devices used for the generation and amplification of microwave signals are Gunn (Transferred Electrons) and Avalanche Transit Time (IMPATT) diodes. These devices have demonstrated economic and/or performance advantages over microwave tubes and as a result are being incorporated into microwave systems [1,2]. IMPATT diodes, at the present time, are the most powerful, but inherently noisy, solid-state sources of microwave energy for continuous wave (cw) applications.

The use of barrier-injection to generate carriers at the edge of a drift region in a punched-through transistor (e.g. pnp) structure has been proposed in one form or another for many years as a possible transit-time negative resistance microwave device [3-7]. The impetus for proposing such a device has been the need for a low-noise solid-state oscillator or amplifier. In 1971, low-noise cw oscillations were obtained from a punched-through metal-semiconductor-metal (MSM) Si structure [8]. Soon after, microwave energy was generated with PtSi-n-p^+ [9], p^+np^+ [10-12] and $p^+n\nu p^+$ [11,12] Si structures. These devices have been termed BARITT (BARrier Injection and Transit Time) diodes [8].

The small-signal properties of a punched-through semiconductor

structure operating under high-field conditions have been considered by Wright [5]. He has shown that the diode can exhibit negative resistance in the range of microwave frequencies due to the combined effects of charge injection and transit-time delay of charge transport. Wright has also concluded that, under high-field conditions, properly designed and operated structures can be used for generation of microwave energy. He pointed out that the charge injection in such structures takes place smoothly (the space-charge at the injecting contact acts as a buffer that partially smoothes out the fluctuations) and that operation should, therefore, occur at low-noise levels. Various alternatives of the high-field punched-through semiconductor structures have also been investigated by Rüegg [6] and Sheorey et al. [7]. These authors concluded that the small-signal negative resistance would not occur, but that useful power generation can be anticipated under large ac signal conditions. The fact that punched-through structures are self-starting implies that the small-signal negative resistance must exist, consequently the possibility of small-signal activity of BARITT devices as discussed by Wright is of fundamental importance.

The power capability and conversion efficiency (dc to rf) are relatively small because of the necessity of a nearly $\frac{3\pi}{2}$ transit angle to create negative resistance [8]; thus these devices are not expected to compete with other solid-state sources (e.g. Gunn and IMPATT diodes) in power applications. However, BARITT diodes have the following advantages over existing solid-state devices:

(1) Their noise-measure is about 20 db lower than that of a Si IMPATT diode and comparable with or lower than a GaAs Gunn diode [13].

(2) BARITT diodes are cheap and easy to construct using available microelectronic techniques [13]; "a typical BARITT Si wafer costs about $3.00 compared with a GaAs wafer which runs up to $90.00 per slice" [13].

(3) They are found to be mechanically and electrically rugged in use and have proved to be reliable and consistent in operation [10,12].

(4) They are found to be totally immune to the parametric effects of harmonic distortion commonly observed with Gunn and IMPATT diodes [12]. Present indications are that BARITT devices will find wide practical applications in microwave systems where moderate powers and low-noise levels are required at low cost.

Following the establishment of the small-signal activity of BARITT diodes, a number of both analytical and numerical ac studies have since been reported [14-22]. A small-signal analytical model which considers the injection of minority carriers over the potential barrier of a forward biased junction and a subsequent $\frac{3\pi}{2}$ transit angle due to the carrier drift across a high-field region appears to qualitatively describe the basic small-signal operation [14-17]. Such models provide relatively simple analytical expressions of the small-signal admittance (or impedance) of the device.

In order to obtain these simple analytical expressions the following assumptions needed to be made in the analytical models:

(1) The carrier drift velocity is saturated in the entire structure.

(2) The diffusion current is neglected.

(3) Simplified boundary conditions are introduced in the interior of the structure instead of properly formulated boundary conditions at the contacts.

A more accurate, but still not exact, model for punched-through semiconductor structures has since been described by Wright and Sultan [10]. In this model, a realistic velocity-field relation has been considered. An analytical model essentially similar to that described in ref. 10, but directly relevant to MSM structures has been described by Weller [14] and by Haus et al. [15]. Weller restricts his analysis to bias voltages greater than the Schottky barrier flat band voltage [23] to ensure that the carrier velocity is saturated at the injecting contact as well as everywhere in the entire n-region of the structure.

Further improvement in the analytical model has been obtained by Sjölund [22] for p^+np^+ structures and by Coleman [16] for MSM structures. In these studies, the injection region of the structures has been included.

Although these simple analytical models are of fundamental importance in providing an understanding of the negative resistance mechanism in punched-through structures, they cannot accurately predict the experimental small-signal response of real devices. This failure results mainly from the neglect of the actual dependence of the carrier velocity upon the electric field and/or

carrier diffusion in the injection and low-field regions of the structure.

Small-signal numerical calculations have been carried out for MSM structures [20,21] and p^+np^+ structures [19,22]. All of these studies consider carrier diffusion and incorporate a velocity-field dependence relation. The small-signal study described in ref. 19, is basically the same as that adopted for the ac studies of IMPATT diodes [25]. The unipolar charge-transport in p^+np^+ structures has been numerically studied by Sjölund [22]. The boundary conditions adopted by this author are vaguely defined. In addition, his numerical solution is not clearly presented and, therefore, cannot be used as a general method to describe the behavior of the structure. Relevant to the small-signal study on MSM structures is the study described in ref. 20 which considers a fictitious velocity-field dependence relation and thermal-equilibrium boundary concentrations for a non-realizable MS contact. An improvement in the small-signal analysis of MSM structures is given in ref. 21. In this study a numerical small-signal model, which considers a realistic velocity-electric field relation has been used to study the temperature dependence of the small-signal admittance of the structure.

The numerical approaches cited above do not have the quantitative character required to describe the general behavior of punch-through devices. For example, the numerical study adopted for MSM structures [20], which uses thermal-equilibrium boundary conditions, cannot accurately describe the actual behavior of the

structure operating under high current conditions. At current levels approaching the saturation current of the MS contact, the boundary concentration reduces significantly from its thermal equilibrium value and the response of the MSM structure can be greatly affected. The numerical model of ref. 19 considers an unrealistic velocity-electric field relation and includes additional yet unimportant physical processes which need not be considered, even for an accurate description of punch-through diodes.

1.2 Objective of the Present Study

The purpose of the present work was to accurately describe the dc and small-signal ac behavior of punch-through MSM structures. The dc properties are of interest since they are an important pre-requisite to the small-signal ac investigation. DC current transport in an MSM structure [23] and in a p^+np^+ structure [24] have been reported, the emphasis in these studies being on the investigation of the charge transport at low-current densities. In the present work, the high current region, which is very important from the structure application point of view, has been considered in detail.

A critical assessment of the available small-signal ac studies shows the need for an "exact" study that would have the general characteristics required for describing the actual behavior of punch-through devices. In the present work it has

been attempted to develop a small-signal ac analysis which consistently takes into account all important physical processes affecting the device performance. A more specjfic aim is to derive a theoretical model of the MSM structure which considers carrier diffusion, a realistic dependence of the carrier velocity upon the electric field, and properly formulated boundary conditions. This model permits a clear and precise formulation of the mathematical problem, and provides a tool for an accurate calculation of structure performance. Moreover, the exact solution allows quantitative comparison with available theories and hence the validity of each simplifying assumption can be investigated.

The theoretical model is applied to PtSi-nSi-PtSi punch-through structures and the computed results are compared with the available experimental data of Snapp and Weissglas [12].

At the present time, the power capability and conversion efficiency of BARITT diodes arequite low. However, the microwave activity of these devices can be improved significantly by proper choice of the physical parameters of the structure. So far little is known about optimum design procedures of BARITT diodes. To bridge this gap, the effects of various physical parameters on the dc and small-signal ac behavior of MSM structures are numerically investigated. Finally, the electrical properties of BARITT diodes with Schottky barrier injecting contacts are found,experimentally, to exhibit an appreciable temperature dependence. To bring more insight into this phenomenon, the temperature dependence of the electrical properties of the structure are also investigated in the

present work.

1.3 Organization of this Thesis

The main part of the original material is contained in Chapters III to X and some auxiliary work is presented in Appendix A. Chapter II discusses the current transport in Schottky barriers made on lightly doped semiconductors. Chapter III is devoted to the investigation of stationary charge transport in MSM structures. In Chapter IV, the flux interchange between the metal and adjacent semiconductor is described, and expressions for the current-dependent boundary concentrations of injected holes are derived. The mathematical models proposed in this study, together with the numerical methods of solution used to solve the mathematical problem are presented in Chapter V. The computed static characteristics and the dc properties of various MSM structures are graphically presented and discussed in Chapter VI. Chapters VII and VIII present the small-signal charge transport properties and the terminal behaviour of the MSM structures. Chapter IX provides a comparison between various theoretical models and available measured data. A summary and conclusion are given in Chapter X.

CHAPTER II

METAL-SEMICONDUCTOR (SCHOTTKY BARRIER) CONTACTS

Two different modes of current transport in metal-semiconductor (MS) contacts are possible, depending on the width of the barrier. In the case of thick barriers (MS contacts with lightly doped semiconductors), thermionic-emission of electrons (holes) over the top of the barrier is expected to be the dominant current transport mechanism. In the case of highly doped semiconductors, the thinner barrier presents a finite transparency to electrons (holes), with energies lower than the barrier height; consequently electron tunneling is expected to dominate current transport.

The MSM structures investigated in this thesis are made of lightly doped semiconductors ($N < 10^{16}$ cm^{-3}); thus, only the current-transport in lightly doped MS contacts will be considered. In this chapter the existing theories are briefly reviewed and the resulting features of their J-V characteristics are discussed.

2.1 Energy Band Relations at an Ideal MS Contact

When a metal is brought into an intimate contact with an n-type semiconductor material (e.g. by a deposition of a metal film on a semiconductor slice), equilibrium between the two materials is established and the Fermi-levels in both sides line up. Relative to the Fermi level in the metal, the Fermi level in the semiconductor has been lowered by an amount equal to the difference

between the two work functions. Figure 2.1 shows the energy band diagram and the charge distribution for an MS contact at thermal equilibrium. The difference, $\Psi_m - (\chi + \phi_n)$, is the contact potential. Ψ_m is the thermionic work function of the metal, χ and ϕ_n are the electron affinity and the internal potential of the semiconductor, respectively. The concentration of mobile electrons, n(x), and holes, p(x), in the conduction and valence bands are

$$n(x) = N_c \exp - \left(\frac{E_c(x)-E_F}{kT}\right) = N_c \exp - \frac{\phi_n(x)}{kT} \tag{2.1a}$$

$$p(x) = N_v \exp - \left(\frac{E_F-E_v(x)}{kT}\right) = N_v \exp - \frac{\phi_p(x)}{kT} \tag{2.1b}$$

where $N_c(N_v)$ is the effective density of states in the conduction (valence) band, E_c and E_v are the lower and upper edges in the conduction and valence bands respectively; k is Boltzmann's constant and T is the absolute temperature [26]. The thermal equilibrium boundary concentrations at the MS interfaces are

$$n_{BO} = N_c \exp - \frac{\phi_{nB}}{kT}$$
$$p_{BO} = N_v \exp - \frac{\phi_{pB}}{kT} \tag{2.2}$$

where ϕ_{nB} and ϕ_{pB} are the barrier heights for electrons and holes measured from the position of Fermi level [27].

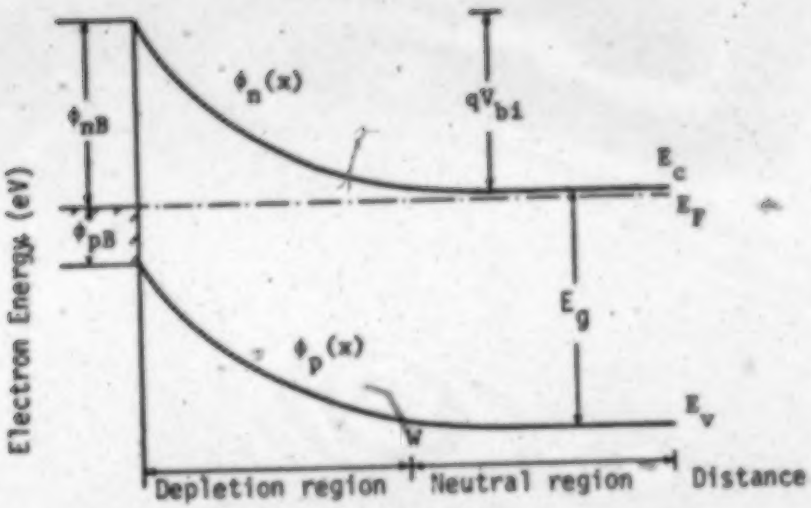

Fig. 2.1a: Energy Band Diagram of an MS Contact at Thermal Equilibrium,

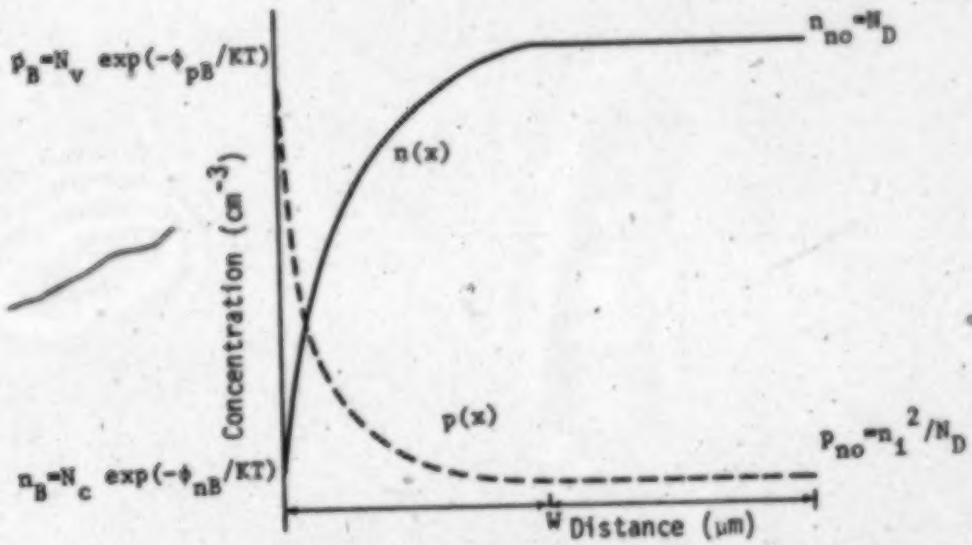

Fig. 2.1b: Corresponding Charge Distribution

The energy band relation in the barrier region can be obtained from the solution of Poisson's equation. For a one dimensional model, where the charge density varies only along the x direction, Poisson's equation is

$$\frac{\partial^2 V}{\partial x^2} = -\frac{q}{\varepsilon}\left(p(x) - n(x) + N_D^+\right) \qquad (2.3)$$

where V is the electrostatic potential, (-q) is the electronic charge, ε is the permittivity of the semiconductor and N_D^+ is the density of ionized donors. Equation (2.3) needs to be solved in combination with appropriate boundary conditions. At thermal equilibrium, the boundary concentrations of electrons and holes are given by Eq. (2.2) and the energy band diagram is then obtained from the solution of Eq. (2.3).

If an external voltage, V_A, is applied to the MS contact, a net current flows through the structure and the charge distribution is altered from its thermal equilibrium profile. The electron and hole concentrations are no longer given by Eq. (2.1) and hence a numerical solution for Eq. (2.3) is necessary. To simplify the analysis, the abrupt junction approximation is usually used to describe the barrier region of MS contacts [27]. Using this approximation, i.e. $\rho = qN_D^+$ for $x < w$ and $\rho = 0$, $\frac{dV}{dx} = 0$ for $x > w$, where w is the depletion width, the solution of Poisson's equation is given by

$$V(x) = \frac{qN_D^+}{\varepsilon}\left(Wx - \frac{x^2}{2}\right) - \frac{\phi_{nB}}{q} \qquad (2.4)$$

$$W = \sqrt{\frac{2\epsilon}{qN_D^+}(V_{bi}-V_A)} \qquad (2.5)$$

where V_A, the applied voltage, is positive (negative) for forward (reverse) bias and $V_{Bi} = \frac{(\phi_{nB}-\phi_n)}{q}$ is the built-in potential [27]. The maximum field strength which occurs at the MS interface (x = 0) is

$$E_m = \frac{qN_D^+}{\epsilon} W = \sqrt{\frac{2qN_D^+(V_{bi}-V_A)}{\epsilon_s}} = \frac{2(V_{bi}-V_A)}{W} \qquad (2.6)$$

The thermal equilibrium values can be obtained by setting $V_A = 0$ in Eqs. 2.4 - 2.6. The distortion of the barrier profile under the applied forward (reverse) bias is shown in Fig. 2.2.

The above analysis ignores the mobile carriers in the barrier region. Goodman [28] and others have shown that a correction of magnitude $\frac{kT}{q}$ is necessary to take into account the contribution of mobile carriers to the electric field. To include the image force and the electric field effects on the potential energy, a correction of magnitude $\Delta\phi$ should be subtracted from the barrier potential ϕ_{nB}. The lowering in the metal work function by an amount $\Delta\phi$ (referred to as image force lowering) is given by

$$\Delta\phi = q\sqrt{\frac{2qE_m}{4\pi\epsilon}} \qquad (2.7)$$

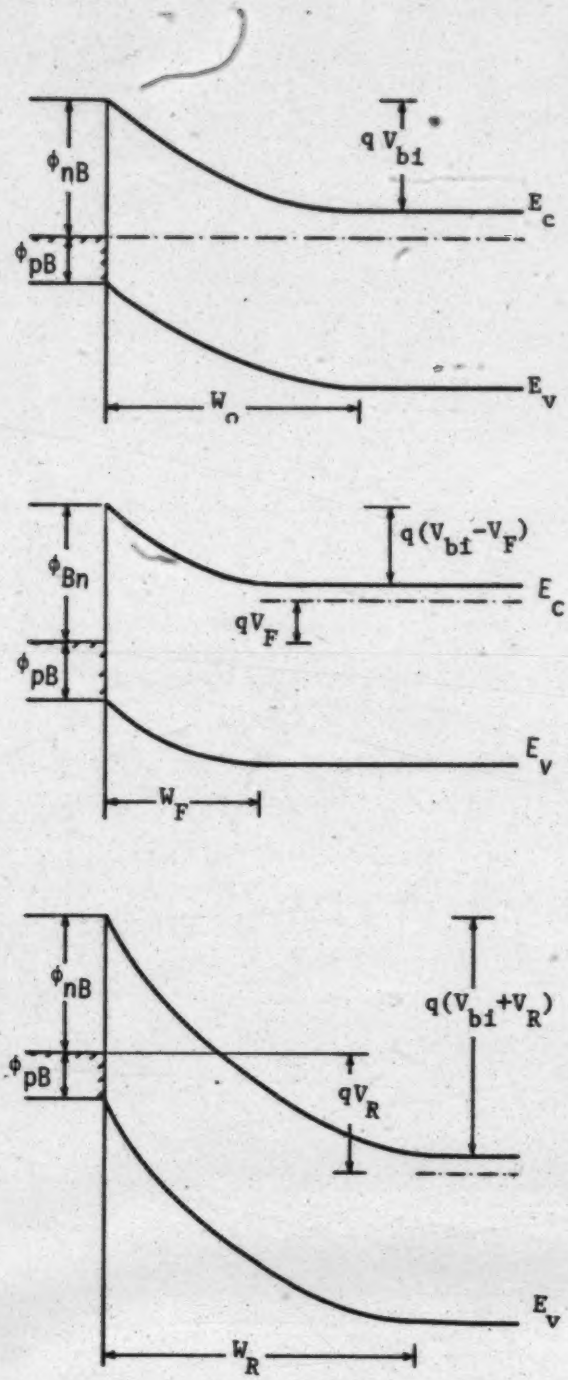

Fig. 2.2: Energy Band Diagram of an MS Contact Under Different Biasing Conditions.

where E_m is the maximum field strength at the MS interface [26].

2.2 Current Transport in Schottky Barriers made on Lightly Doped Materials

2.2.1 Basic theories

Thermionic emission of electrons over a potential barrier of an MS contact is similar in many aspects to the thermionic emission of electrons in a metal-vacuum system. The major difference, however, is the location of the potential maximum. In the case of metal-vacuum system it is located in the vacuum while for a MS contact it is located in the semiconductor. The activation of electrons (holes) in the MS contact can proceed in two different ways depending on the width of the depletion region with respect to the electron (hole) mean free path. If the barrier thickness is small compared to the mean free path, electron collision can be neglected for all practical purposes. This situation was first considered by Bethe [29], and is usually referred to as the "diode" theory. If the barrier thickness is large compared to the electron mean free path, an electron experiences many collisions in the barrier before reaching the top of the barrier. This latter case was studied by Wagner [30] and Schottky and Spenke [31] and is usually referred to as the "diffusion" theory. A detailed presentation of both of these theories can be found in Henish [26]. A more detailed treatment of the diffusion theory can be found in Spenke's book [27].

The J-V characteristic of an MS contact, as given by the diode theory is described by

$$J = J_s[\exp(\frac{qV_A}{kT}) - 1] \tag{2.8}$$

with $$J_s = A^*T^2 \exp - (\frac{\phi_{nB}}{kT}) \tag{2.9}$$

$$A^* \equiv \frac{4m^* qk^2}{h^3} \tag{2.10}$$

The constant A^*, the Richardson constant, contains the effective mass of electrons, m^*, which is assumed to be a scalar quantity in Bethe's theory. Since the effective mass in semiconductors is generally a tensor quantity, A^* may therefore depend on the orientation of the emitting surface.

For a semiconductor having an energy band with ellipsoidal constant energy surfaces in momentum space, Crowell [32] has shown that A^* is given by

$$A^* = \frac{4\pi q^2 k^2}{h^3} \sum(\ell^2 m_y^* m_z^* + m^2 m_z^* m_x^* + n^2 m_x^* m_y^*) \tag{2.11}$$

In Eq. (2.11), ℓ, m, n are the direction cosines of the normal to the emitting plane relative to the principal axis of the ellipsoid; m_x^*, m_y^* and m_z^* are the components of the effective mass tensor, and the summation has to include all energy surfaces participating in the emission process. For semiconductors with isotropic effective mass in the lowest minimum of the conduction band (such as n-type

GaAs), Eq. (2.11) reduces to

$$A^* = \frac{4\pi q k^2}{h^3} m^* \qquad (2.12)$$

where m^* is the effective mass associated with the energy surface considered.

The J-V characteristic described by Eq. (2.8) shows that at forward bias voltages greater than a few $\frac{kT}{q}$, a plot of log J versus voltage should yield a straight line with a slope $\frac{q}{kT}$. The reverse characteristic as described by Eq. (2.8) appears to present an ideal saturation. This is only true if the barrier height is independent of the external bias, which is never the case. Effects such as image force, quantum mechanical tunneling and reflection and optical phonon scattering will lead to a dependence of the barrier height on applied voltage and no real saturation under reverse bias will take place. The change in the barrier height will in turn result in changes in the shape of the forward characteristic, and the semilog slope instead of being equal to $\frac{q}{kT}$, will be equal to $\frac{q}{nkT}$, where n is a dimensionless parameter greater than unity and is given by [33]

$$n = 1 + \frac{\partial \phi_{Bn}}{\partial V} \qquad (2.13)$$

For well fabricated MS contacts (e.g. free from interfacial layers), the values of n obtained by the diode theory are usually less than 1.03 [33].

The charge transport properties of MS contacts as described by the isothermal diffusion theory are based on the Boltzman current density equation

$$J_n = q[n(x)\mu_n E + D_n \frac{\partial n}{\partial x}] \qquad (2.14)$$

where μ_n and D_n are the electron mobility and diffusion constant respectively [27]. The first term on the righthand side of Eq. (2.14) is the drift current density component as given by Ohm's law, while the second term is the diffusion current component which is due to the concentration gradient.

To obtain the J-V characteristic, Eq. (2.14) and Poisson's equation should be integrated subject to appropriate boundary conditions. Assuming thermal equilibrium boundary concentrations at the depletion layer edges, using the junction abrupt approximation and adopting the Einstein relation, Wagner has arrived at the following J-V characteristic.

$$J = J_{SD}[\exp(\frac{qV_A}{kT}) - 1] \qquad (2.15)$$

$$J_{SD} = q\mu_n N_c[\frac{2q(V_{bi}-V)}{\epsilon}]^{1/2} \exp - \frac{\phi_{Bn}}{kT} \qquad (2.16)$$

where J_{SD} is the reverse saturation current density as given by the diffusion theory [34]. In the derivation of Eq. (2.15), μ_n (the electron mobility) is assumed to be constant.

The reverse characteristic as shown by Eq. (2.15) does not present perfect saturation as in the case of the diode theory.

Rather, for large applied bias, Eq. (2.15) shows that the current density should increase in the reverse direction as $\sqrt{(V_{bi}-V_A)}$. To this current density variation the contribution of the image force correction and tunnel penetration and reflection must be included. More accurate treatment of the diffusion problem using digital computers [35,36] results in a J-V characteristic which can be accurately described by the equation

$$J = J_{SD}[\exp(\frac{qV_A}{nkT}) - 1] \qquad (2.17)$$

with a value of n approximately equal to 1.06, appropriate for all practical values of barrier heights of clean MS contacts [33].

2.2.2 Thermionic emission-diffusion theory

A theory which incorporates thermionic emission (T) and diffusion (D) theories into a single T-D emission theory has been presented by Schultz [37], who assumed simplified electron effective mass and neglected all image force effects. Recently, Crowell and Sze [38] have performed a similar calculation assuming the correct value of electron effective mass and including image force effects, phonon scattering and tunnel penetration. This approach is based on the boundary condition of a thermionic recombination velocity v_R, near the MS interface.

The energy band diagram considered by Crowell and Sze is shown in Fig. 2.3. Effects of mobile charges on the electric field

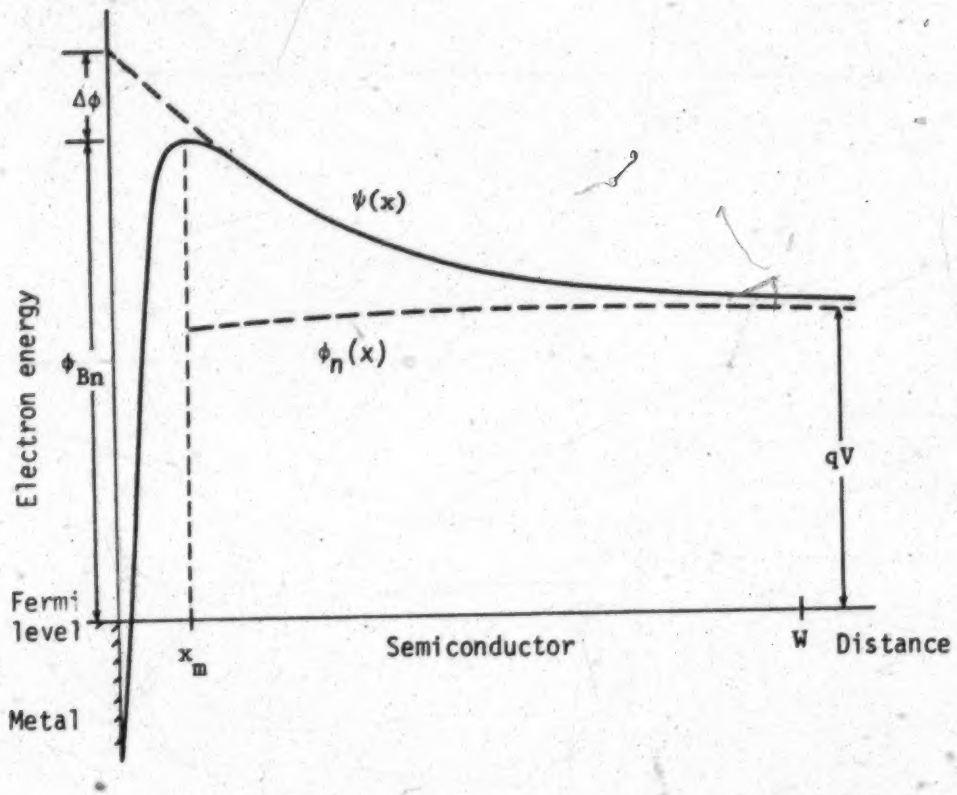

Fig. 2.3: Electron Potential Energy (ψ) Versus Distance for an MS Barrier.

are neglected. They have assumed that the region between the potential maximum ($x = x_m$) and the depletion layer edge ($x = W$) is isothermal and the electron temperature is equal to the lattice temperature. The current density in this region is specified in terms of an imref ϕ_n, by

$$J = - q\mu n \frac{d\phi_n}{dx} \tag{2.18}$$

where n is the electron density given by Eq. (2.1). In the interfacial layer $[0,x_m]$ the potential energy varies very rapidly in a distance comparable to the mean free path, and hence Eqs. (2.1) and (2.17) do not apply in this region. Instead, if this layer acts as a sink for electrons, the current density at the potential maximum could be described in terms of an effective recombination velocity v_R, as

$$J = q(n_m - n_o)v_R \tag{2.19}$$

where n_m is the electron density at x_m when the current is flowing, n_o is the quasi-equilibrium electron density at x_m (the density which would occur if it were possible to reach equilibrium without altering the magnitude and position of the potential energy maximum [27]).

The J-V characteristic as described by the T-D theory is given by

$$J = \frac{qN_c v_R}{1+\frac{v_R}{v_D}} \exp(-\frac{\phi_{Bn}}{kT})[\exp(\frac{qV_A}{kT}) - 1] \tag{2.20}$$

where $$v_D = \left[\int_{x_m}^{w} \left(\frac{q}{\mu kT} \exp - \frac{(\phi_{Bn} - \psi)}{kT}\right)\right]^{-1} \qquad (2.21)$$

is an effective velocity associated with the transport of electrons from the edge of the depletion layer w to the potential energy maximum x_m.

If no electrons other than those associated with the current density $qn_o v_R$ return, the semiconductor acts as a thermionic emitter, then

$$v_R = \frac{A^* T^2}{qN_c} \quad . \qquad (2.22)$$

If $v_D >> v_R$, the pre-exponential term in Eq. (2.20) is dominated by v_R and the thermionic emission theory most nearly applies. If, on the other hand, $v_D << v_R$, the diffusion process is dominant. If the image force effects are neglected and the electron mobility were independent of the electric field, v_D would be equal to μE, where E is the electric field in the semiconductor near the boundary. The standard Schottky result would then be obtained (Eq. (2.15)).

In the derivation of Eq. (2.20), a recombination velocity, v_R, associated with thermionic emission was introduced as a boundary condition to describe the collecting action of the metal in a Schottky barrier. In many cases there is an appreciable probability that an electron which crosses the potential energy maximum will be backscattered with a subsequent reduction in the net current over the barrier. The probability of electron emission over the potential barrier is given by

$$f_p \approx \exp - \frac{x_m}{\lambda} \tag{2.23}$$

where λ is the optical phonon mean free path [39,40]. In expression (2.23), the values of x_m and λ are given by

$$x_m = \left(\frac{q}{|6\pi\epsilon|E_m|}\right)^{1/2} \tag{2.24}$$

$$\lambda = \lambda_o \tanh \frac{E_o}{kT} \tag{2.25}$$

where E_o is the optical phonon energy and λ_o is the high energy low-temperature asymptotic value of the mean free path [39,40]. In the derivation of Eq. (2.22) it is assumed that $E_o > kT$ and hence the above treatment is not expected to be valid in the low field limit, especially when $kT \gtrsim E_o$.

In addition to the effects of phonon scattering, the energy distribution of electrons is further distorted from the Maxwellian distribution because of quantum mechanical tunneling and reflection. Crowell and Sze [41] have outlined an approach whereby the quantum-mechanical transmission (QMT) of carriers incident on Schottky barriers may be calculated as a function of the carrier energy and effective mass, the barrier height, the electric field at the MS interface and the shape of the potential barrier in the vicinity of the interface. The ratio, f_Q, of the total current flow considering tunneling and quantum-mechanical reflection to the thermionic current flow neglecting these effects, is

$$f_Q \equiv \int_{-\infty}^{\infty} P_Q \exp - \left(\frac{E}{kT}\right) d\left(\frac{E}{kT}\right) \tag{2.26}$$

where E is the electron energy measured from the position of the energy maximum and P_Q is the quantum-mechanical transmission coefficient [41]. The field at which f_Q starts to rise rapidly marks the transition between thermionic (T) and thermionic-field (T-F) emission, since at this point the field-enhanced tunneling process becomes the dominant mechanism. For Si, this transition occurs at field strength of about 4×10^5 Vcm^{-1} [41].

The complete expression for the J-V characteristic as given by T-D model and taking into account f_p and f_Q is

$$J = J_s[\exp(\frac{qV_A}{kT}) - 1] \tag{2.27}$$

$$J_s = A^{**}T^2 \exp - \frac{\phi_{Bn}}{kT} \tag{2.28}$$

where $$A^{**} = \frac{f_p f_Q A^*}{1+f_p f_Q \frac{v_R}{v_D}} \tag{2.29}$$

is the effective Richardson constant. Eq. (2.28) is similar to Eq. (2.9) with A^{**} somewhat smaller than A^*.

Andrews and Lepselter [42], have shown that the experimental results, made on metal silicide Schottky barriers, are in good agreement with those obtained from Eq. (2.27). However, the reverse J-V characteristic does not show actual saturation. They have shown that the soft behavior in the reverse characteristic is due to the slight variation of the effective Richardson constant with the

maximum value of the electric field at the MS interface. They have also pointed out, that the effective barrier height, ϕ_{Bn}, can vary more rapidly with the electric field than the usual image force model would predict. The additional barrier lowering due to the dipolar effect at the MS interface is

$$\Delta\phi_{Bn} = \alpha E_m \tag{2.30}$$

where $\alpha = \frac{\partial\phi_{Bn}}{\partial E_m}$ is an adjustable numerical constant [42]. Consequently the J-V characteristic of the real MS contact can be well described by

$$J = A^{**}T^2 \exp - \frac{(\phi_{Bn}-\Delta\phi-\alpha E_m)}{kT} [\exp(\frac{qV_A}{kT}) - 1] \tag{2.31}$$

CHAPTER III

CHARGE TRANSPORT IN MSM STRUCTURES

Stationary charge transport in a MSM structure has been studied by Sze et al. [23] and a similar study on a p^+np^+ structure has been reported by Chu et al. [24]. In their studies, which are based on thermionic emission theory, charge transport at low current densities was mainly investigated, while the high-current region was discussed only briefly. The predicted exponential current-voltage dependence in the low-current region was then verified experimentally [23]. The high-current region, which is very important from an application point of view, has not yet been adequately described in the literature for purposes of an accurate investigation of the ac properties of these structures.

In this chapter, all important physical processes which can affect charge transport in MSM structures at technically important current densities are investigated from the point of view of diffusion theory.

3.1 Energy Band Diagram and Charge Distribution

An MSM structure is a two terminal device, having a semiconductor slice sandwiched between two metallic contacts as shown in Fig. 3.1a. The thermal equilibrium energy band diagram of a PtSi-nSi-PtSi structure is shown in Fig. 3.1b. At thermal

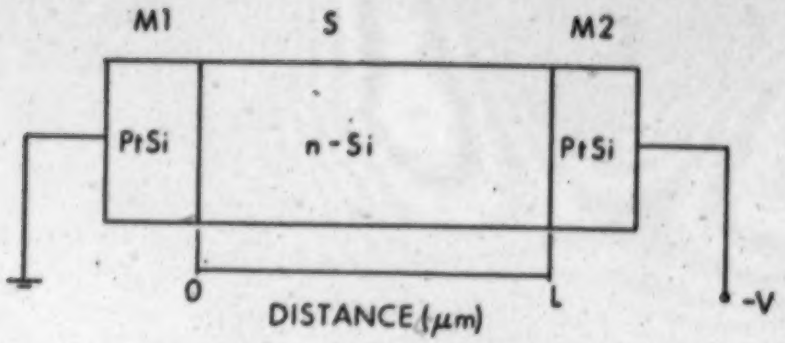

Fig. 3.1a: Schematic Diagram of an MSM Structure.

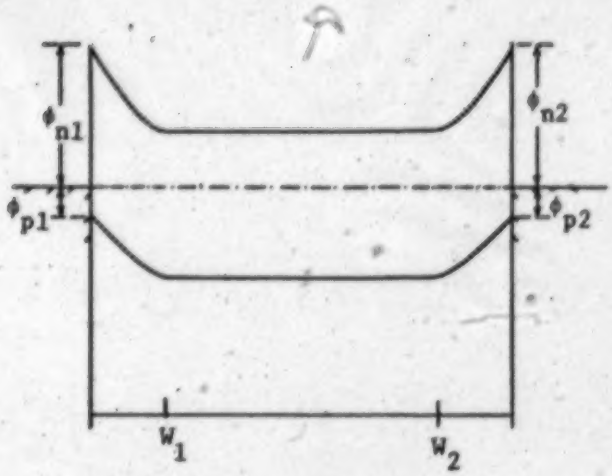

Fig. 3.1b: Corresponding Energy Band Diagram at Thermal Equilibrium.

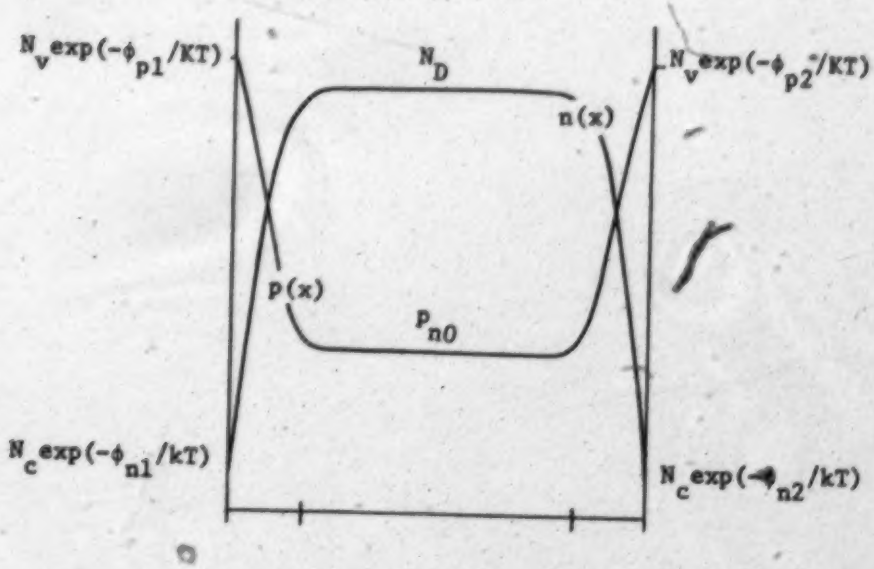

Fig. 3.1c: Corresponding Mobile Charge Distribution.

equilibrium, the sum of the two depletion regions at the contacts is a small fraction of the total semiconductor width L. The charge distribution of the mobile carriers is shown in Fig. 3.1c.

According to Spenke [27], the thermal equilibrium boundary concentration at an ideal MS interface is

$$C_o = N_{eff} \exp - \frac{\phi}{kT} \qquad (3.1)$$

where N_{eff} is the effective density of states in the conduction (valence) band and ϕ is the barrier height for the electrons (holes). Since the electron barrier height of the PtSi-n-Si contact is in the range 0.85 - 0.87 eV, the interface concentration of electrons and holes is approximately 7×10^4 and 7×10^{14} respectively [43]. Consequently there is a high concentration of injected holes close to the MS interface and thus the semiconductor region in the immediate vicinity of the interface cannot be treated as an ideal insulator when calculating the image force effect on the barrier shape [26]. If the charge transport in close proximity to the interface is described from the thermionic emission theory point of view, the actual shape of the potential barrier in this region, which can be significantly affected by any modified version of the image force, is unimportant. Farther from the interfacial layers formed at the contact, where the diffusion theory is applicable, the image force becomes less important and the energy band profile is primarily determined by ionized donor density.

If an external voltage is applied to the MSM structure of

Fig. 3.1a, the M1 and M2 contacts become forward and reverse biased respectively. As the applied voltage increases the sum of the two depletion region widths, w_1 and w_2, also increases. Eventually at the "reach-through" voltage (also called the "punch-through" voltage) V_p, the two depletion regions touch each other, and their width is exactly equal to L. At the punch-through condition, the semiconductor material is completely depleted of majority carriers (electrons). The energy band diagram and the mobile charge distribution of MSM structures biased below V_p are shown in Figs. 3.2a and 3.2b respectively. As the voltage increases, a point is reached at which the potential energy becomes flat; the corresponding voltage is called flat band voltage V_{FB}. The flat band energy band profile is shown in Fig. 3.3. For applied voltages in excess of V_{FB}, the energy band profile is bent even further, and the maximum voltage that can be applied to the structure is limited by the avalanche breakdown [23].

3.2 Stationary Charge Transport

(a) Small voltage range ($V \leq V_p$)

The charge transport in an MSM structure, biased below or at V_p, has been described by Sze *et al*. [23]. In their study, the J-V characteristic of the structure has been obtained from thermionic emission theory. It was shown that the thermionic injection of electrons (holes) over the reverse (forward) bias contact contributesto the total conduction current density. The

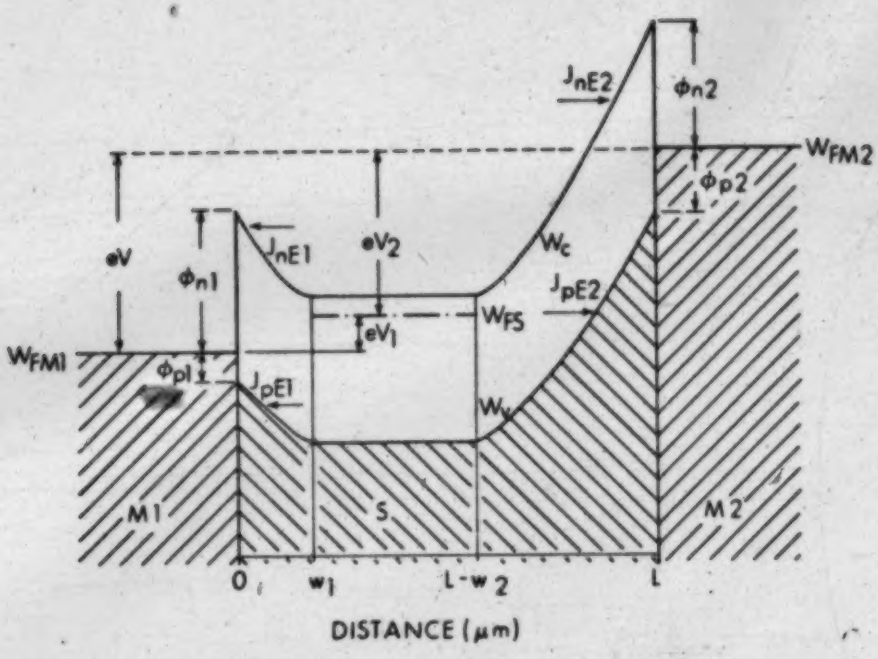

Fig. 3.2a: Energy Band Diagram of an MSM Structure Biased Below Punch-Through Voltage.

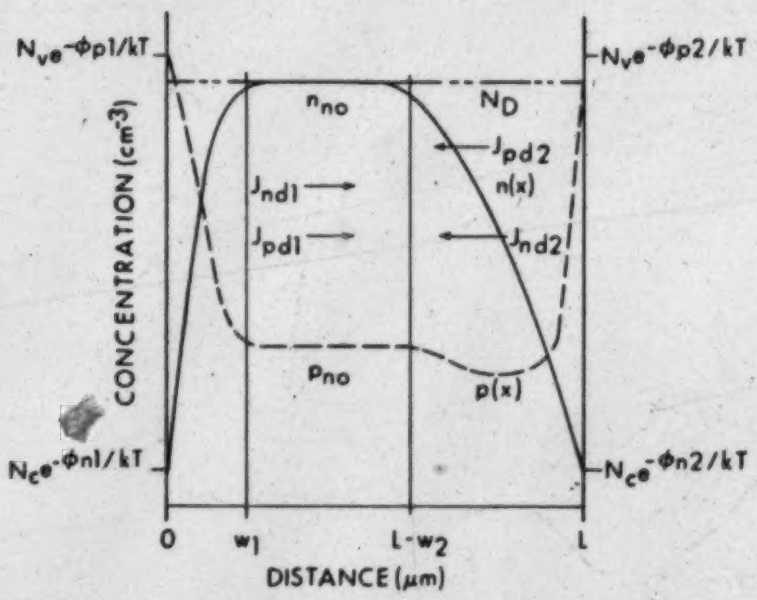

Fig. 3.2b: Corresponding Concentration Profile of Mobile Holes and Electrons.

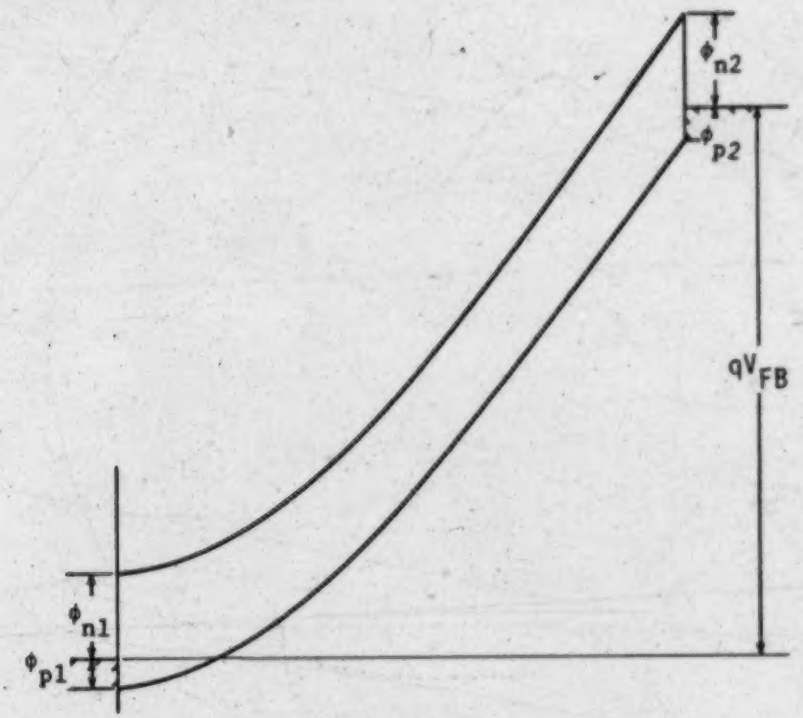

Fig. 3.3: Energy Band Diagram of an MSM Structure Under Flat Band Condition.

electron and hole current density components for MSM structures are given by [23]

$$J_n = A_n^{**} T^2 \exp - \frac{\phi_{nB2}}{kT} \exp\left(\frac{\Delta\phi_{nB2} + \alpha_2 E_m}{kT}\right)\left[1 - \exp - \frac{qV_2}{kT}\right] \tag{3.2}$$

$$J_p = \frac{qD_p P_{no}}{L_p} \tanh\left[\frac{(L-(w_1+w_2))}{L_p}\right]\left[1 - \exp\left(- \frac{qV_2}{kT}\right)\right]$$

$$+ \frac{A_p^{**} T^2 \exp-[(\phi_{BP2}+qV_{bi2})/kT]}{\cosh\left(\frac{L-(w_1+w_2)}{L_p}\right)}\left[\exp \frac{qV_1}{kT} - 1\right] \tag{3.3}$$

where L_p is the diffusion length for holes, V_1 and V_2 are the forward and reverse bias voltages respectively; other quantities have been defined previously. Equation (3.2) has been considered in Chapter II in conjunction with the current transport in Schottky barriers. Equation (3.3) is derived from the solution of the steady state continuity equation for holes in the quasineutral region $[w_1,(L-w_2)]$, subject to the thermal equilibrium boundary conditions at the depletion layer edges w_1 and $(L-w_2)$. Since the injection ratio ν of the M1 contact, which controls the hole injection, is very small (e.g. $\nu < 0.1$ in a forward biased Au-nSi diode with $J_T \lesssim 5$ Acm^{-2}) [44], the hole current can be neglected and the total current density approaches the electron saturation current density of the M2 contact. For PtSi-nSi contacts, the room temperature value of the electron saturation current density is $\sim$ 3-10 x 10^{-8} Acm^{-2}.

Depending upon the concentration and the properties of the semiconductor trapping centers, the current due to electron-hole pairs thermally generated in the reverse biased barrier can significantly exceed the electron thermionic emission current of the barrier. Thus, thermal generation of electron-hole pairs in the barrier region of the M2 contact can affect the current transport to the same extent as in the case of a reverse biased MS contact [42].

(b) Applied voltages above V_p

At voltages above V_p, the concentration of majority carriers in the whole semiconductor bulk is effectively reduced to the very low boundary concentration ($\sim 10^4$ cm^{-3}). However, the I-V characteristic shows a sharp increase of the current with slight increase in voltage [23]. Since the flux of electrons thermionically emitted from the M2 contact remains essentially unchanged, the steep rise of the current can only be accounted for by a sharp increase of the hole current component thermionically injected at the M1 contact. It can be shown that, at current density of about 10^{-6} Acm^{-2}, the room temperature concentration of electrons is at least ten times less than the concentration of injected holes anywhere in the semiconductor bulk [43]. At current densities exceeding 10^{-4} Acm^{-2}, the electron current component is only about 0.1% of the total current. As a consequence, the charge transport through the semiconductor becomes practically a unipolar flow of injected holes through the bulk of the semiconductor.

For an MSM structure biased above V_p, only the continuity equation for injected holes given by [34] needs to be considered:

$$\frac{\partial p(x,t)}{\partial t} = G_p(x,t) - U_p(x,t) - \frac{1}{q}\frac{\partial}{\partial x} J_p(x,t) \tag{3.4}$$

In Eq. 3.4, G_p is the hole generation rate, U_p is the hole recombination rate, p is the density of injected holes and J_p is the hole conduction current density. At the steady state dc conditions, $\frac{\partial p}{\partial t} = 0$ and Eq. 3.4 can be integrated to give

$$J_p(x) = J_T - J_n(x) + \int_x^L [G_p(x') - U_p(x')]dx' \tag{3.5}$$

where J_T is the total current density and J_n is the electron thermionic-emission current density of the M2 contact. In properly designed and operated MSM structures, the electric field is below the critical value for avalanche breakdown, and the semiconductor temperature is such that insignificant thermal generation of mobile carriers takes place; hence:

$$J_n + \int_x^L [G_p(x') - U_p(x')]dx' \ll 0.1 \text{ Acm}^{-2} \tag{3.6}$$

Eq. 3.5 now simplifies to

$$J_p(x) = J_T \tag{3.7}$$

for current densities exceeding $0.1\,A\,cm^{-2}$.

The unipolar charge transport in a semiconductor with nonuniform electric field and mobile electron distribution has been considered by Stratton [36]. Under non-equilibrium conditions, he has shown that the total conduction current density is given by:

$$J_T = qu(T_e)\, n(x)E(x) + qD(T_e)\,\frac{dn(x)}{dx}$$

$$+ qn(x)\,\frac{dD}{dT_e}\,\frac{dT_e(x)}{dx} \qquad (3.8)$$

Eq. 3.8 is the Boltzman current equation and it contains terms arising from drift, diffusion and thermal diffusion. The electron temperature, T_e, is not a unique function of the local field; it depends on J_T (it must tend to T_c when J_T tends to zero and the barrier region approaches thermal equilibrium) and can be determined from the simultaneous solution of the equations for the current flow and the conservation of energy. Stratton [36] has also shown that μ and D are related by the Einstein relation:

$$D(T_e) = \frac{\mu(T_e)kT_e}{q} \qquad (3.9)$$

if the spherically symmetrical part of the electron distribution function in momentum space retains its Maxwellian shape under the applied field conditions.

Assuming a Maxwellian electron-energy distribution function, electron scattering by acoustic phonons, adopting thermal equilibrium boundary conditions and neglecting both the mobile space charge and image force corrections, Stratton has evaluated

the electron temperature in the barrier region of a forward and reverse biased MS structures. For a small forward and reverse current, the electron temperature is very close to the crystal lattice temperature, T_c, everywhere in the barrier region. For a large reverse bias, T_e peaks close to the MS interface and its maximum value significantly exceeds T_c, while for large forward bias T_e becomes up to 30% less than T_c. Interpreting Stratton's results for the case of MSM structures, it can be expected that, in the injecting contact region, the injected hole temperature, T_p, is close to T_c, independent of the value of the local field, and, in the collecting contact barrier, T_p is expected to be significantly above T_c.

The hole temperature directly affects the thermal diffusion current, but it only indirectly affects the diffusion and drift currents. Since the maximum gradients of T_p are most likely to occur close to the MS interfaces [36], thermal diffusion is expected to be negligibly small in comparison with drift and/or diffusion through the whole semiconductor bulk. Consequently, if suitable approximations for $\mu(T_p)$ and $D(T_p)$ can be found the complex calculations of hole-temperature distribution becomes unnecessary, even for accurate charge transport studies. On the other hand, since "hot" holes have been shown to be a major source of noise in MSM structures [46], and since the temperature very strongly affects noise properties of "hot" holes, Stratton's approach, involving scattering of injected holes by acoustical and optical phonons, appears to be necessary for carrying out

detailed noise studies.

In the barrier region of the injecting contact, the low-field mobility, μ_o, and diffusion constant, D_o, are the best approximations for $\mu(T_p)$ and $D(T_p)$, respectively. In the low and medium field regions of the collecting contact barrier, the following approximation for the diffusion constant is given by

$$D(T_p) = \mu_o\left(\frac{kT_c}{q}\right)\left[1 + \frac{1}{2}\left(\frac{\mu_o E}{c}\right)^2 \frac{3\pi}{32}\right] \qquad (3.10)$$

where c is the velocity of longitudinal acoustic waves [47]. Eq. (3.10) is derived by substituting the following expressions for the field-dependent hole temperature and mobility [47] into the Einstein relation:

$$T_p = T_c\left[1 + \left(\frac{\mu_o E}{c}\right)^2 \frac{3\pi}{32}\right] \qquad (3.11)$$

$$\mu = \mu_o\left[1 - \frac{1}{2}\left(\frac{\mu_o E}{c}\right)^2 \frac{3\pi}{32}\right] \qquad (3.12)$$

In the high field region near the collecting contact, the hole scattering by optical phonons slows down the growth of T_p and the diffusion constant decreases with increasing electric field. At field strengths of 40 - 60 kV/cm, Sigman and Gibbons [48] have shown experimentally that the diffusion constant of holes in silicon is reduced by about 30% from its low-field value. In view of small deviations from the low-field value, it is felt that

$$D(T_p) = D_o \qquad (3.13)$$

is a satisfactory approximation for $D(T_p)$, which in the low field region reduces the error associated with neglecting thermal diffusion (note that the diffusion and thermal diffusion current components have opposite signs through most of the semiconductor). In the high field region, where carrier drift is the dominant charge transport mechanism, Eq. (3.13) results in a negligible error.

In most of the collecting contact barrier region the hole temperature is an unambiguous function of the electric field and, in analogy with the high field region of IMPATT diodes [25], the temperature dependent drift velocity of holes, $v(T_p)$, can be approximated by the measured field-dependent drift velocity

$$v(T_p) = \mu(T_p)E = v(E,T_c) . \qquad (3.14)$$

In the close vicinity of the M2 contact, the hole temperature decreases rapidly to the metal temperature, while the electric field still increases. Accordingly Eq. 3.14 becomes a poor approximation for $v(T_p)$ in this region. However, the resulting error will be negligible since the region occupies, at most, a few percent of the total semiconductor width.

In view of the previous discussions, the total conduction current in the semiconductor of the MSM structure biased above V_p can be described by:

$$J_T = q\mu_o p(x)E(x) - \mu_o kT_c \frac{dp(x)}{dx} \; ; \; 0 \leq x \leq x_m$$

$$J_T = qp(x)v(E,T_c) - \mu_o kT_c \frac{dp(x)}{dx} \; ; \; x_m \leq x \leq L \tag{3.15}$$

where x_m is the position of the potential energy maximum separating the barrier regions of the injecting and collecting contacts.

In real semiconductors, some of the injected holes are effectively immobilized in trapping centers; thus, they only affect the electric field strength. For a single set of traps,

$$\frac{dE(x)}{dx} = \frac{q}{\epsilon}[N_D^+ + p(x) + p_t(x)] \tag{3.16}$$

where N_D^+ is the density of ionized effective impurities, and $p_t(x)$ is the concentration of trapped holes [49] given by:

$$p_t(x) = \frac{p(x)N_t}{k+p(x)} \tag{3.17}$$

In Eq. (3.17), N_t is the concentration of traps and

$$k = gN_V \exp(w_v - w_t)/kT_c \tag{3.18}$$

where w_t is the trap energy level, g is its degeneracy factor, and w_v is the upper-most energy level in the valence band. If the concentration of trapping centers (Au,Cu,Fe and Zn atoms are effective trapping centers in Si) is comparable to or larger than the concentration of injected holes, then not only will higher

voltages (fields) be needed to reach the same stationary currents, but also the dynamical behavior of the MSM structures will be affected [50]. If the trap concentration is less than the concentration of injected holes, which is usually true for the MSM structures at current density levels exceeding 0.1 Acm^{-2}, the structure can be regarded as trap free, and then Poisson's equation simplifies to

$$\frac{dE(x)}{dx} = \frac{q}{\varepsilon}(N_D^+ + p(x)) \ . \qquad (3.19)$$

3.3 Basic Dynamic Equations

The dynamic behavior of MSM structures biased above V_p is described by Poisson's equation and the continuity equation for holes. When an ac voltage is impressed on a steady-state dc bias voltage, the physical quantities described in the previous section (e.g. p, E, J_p, etc.) become position and time dependent. Neglecting thermal and avalanche generation, recombination and trapping processes, the above mentioned equations take the form

$$\frac{\partial E(x,t)}{\partial x} = \frac{q}{\varepsilon}(N_D + p(x,t)) \qquad (3.20)$$

$$\frac{\partial p(x,t)}{\partial t} = -\frac{1}{q}\frac{\partial J_p(x,t)}{\partial x} \qquad (3.21)$$

To describe the small-signal operation, Eqs. 3.20 and 3.21 can be simplified by using the method of small perturbation of the

dc components [51]. According to this method, the physical quantities in Eqs. 3.20 and 3.21 can be expressed as the sum of a time independent term (dc component) and a small oscillating (ac) component, of the form

$$C(x,t) = C_0(x) + \tilde{C}(x)e^{j\omega t} \tag{3.22}$$

where C is the physical quantity (e.g. p, E, J_p), the zero subscripts indicate the dc components and tilde denotes the small-signal perturbation of the steady-state value. The quantities with the tilde are, in general, complex functions of positions. By substituting from Eq. (3.22), into Eqs. (3.20) and (3.21), we obtain two sets of equations for the dc quantities and the small-signal ac quantities.

The resulting small-signal equations are

$$\frac{\partial \tilde{E}(x)}{\partial x} = \frac{q}{\varepsilon}\tilde{p}(x) \tag{3.23}$$

$$j\omega p(x) = -\frac{1}{q}\frac{\partial \tilde{J}_p(x)}{\partial x} . \tag{3.24}$$

From Eqs. (3.23) and (3.24), it follows that,

$$\tilde{J}_p(x) + j\omega\varepsilon\,\tilde{E}(x) = \tilde{J}_T . \tag{3.25}$$

Equation (3.25) states the sum of the conduction and the displacement

currents, $\tilde{J}_T$ (the total current) is constant, independent of position. Applying the small-signal perturbation method to the Boltzman current equation (Eq. (3.15), under time varying conditions) yields the following expression for $\tilde{J}_p$:

$$\tilde{J}_p(x) = qv_o(x)\tilde{p}(x) + qp_o(x)\mu_d(x)\tilde{E}(x) - qD_p \frac{d\tilde{p}(x)}{dx} \tag{3.26}$$

where $$v_o(x) = \mu_\ell E_o(x) \quad ; \quad 0 \leq x \leq x_m$$

$$v_o(x) = \mu_o(x)E_o(x) \quad ; \quad x_m \leq x \leq L \tag{3.27}$$

is the dc drift velocity for holes, and μ_d is the differential mobility, given by:

$$\mu_d(x) = \frac{dv_o(x)}{dE_o(x)} \, . \tag{3.28}$$

Substituting from Eq. (3.27) into Eq. (3.25), yields

$$\tilde{J}_T = qv_o(x)\tilde{p}(x) - qD_p \frac{d\tilde{p}(x)}{dx} + (qp_o(x)\mu_d(x) + j\omega\varepsilon)\tilde{E}(x) \tag{3.29}$$

In summary, the charge transport properties of MSM structures biased beyond punch-through voltages, are described by Poisson's equation and the total current equation of the form (Eqs. (3.17) and (3.19)) for the dc case and (Eqs. (3.23) and (3.29)) for the small signal ac case.

CHAPTER IV

BOUNDARY CONDITIONS

4.1 Simplified Boundary Conditions

The charge transport in MSM structures has been investigated in the preceding chapter and it has been shown that the total current equation together with Poisson's equation describe the physical properties of the structure. Regarding the total current density as a parameter, Eqs. (3.17) and (3.19) form a system of two non-linear differential equations for the electric field E and the hole concentration p. Two boundary conditions are, therefore, needed to determine uniquely the solution of the above mentioned equations.

In the metal, the concentration of mobile carriers is extremely large ($\sim 10^{22}$ cm^{-3}) and hence the physical conditions of the mobile carrier system (e.g. the carrier concentration, energy distribution , carrier fluxes and emission processes) are not affected by any current flow. Therefore, any physical condition of the metal which can be analytically related to the physical conditions of the neighbouring semiconductor can serve as a boundary condition.

The mobile carriers in the metal form a highly degenerate system which cannot be analytically described. However, only a

small fraction of mobile carriers from the metal can overcome the interface potential barrier (formed at the metallurgical junction of the MS contact). As a consequence, the mobile carriers in the semiconductor side form a non-degenerate system which obeys Maxwell-Boltzmann statistics. Under thermal-equilibrium conditions, when the carrier flux emitted from the metal into the semiconductor is equal to the carrier flux emitted from the semiconductor, both the flux and the concentration of mobile carriers, at the semiconductor boundary layer, are simply related to the physical conditions of mobile carriers in the semiconductor bulk.

The equilibrium conditions of the ideal gas at the MS interface have been considered by Spenke [27] who adopted the thermal equilibrium interface concentration as a boundary condition for the MS structure. In a study on ohmic contacts, Stöckmann [49] has pointed out that the thermal-equilibrium boundary concentration is a satisfactory approximation for the boundary condition only if the net current crossing the MS interface is sufficiently small compared to the thermal emission current of the contact. Fan [52], discussed the conditions of the MS contact under large current densities. He arrived at the following boundary concentration

$$p_{BJ} = p_{Bo} \pm \frac{|J_c|}{q\bar{v}_{th}} \qquad (4.1)$$

where p_{Bo} is the thermal equilibrium boundary concentration, J_c is the net conduction current crossing the interface, and $\bar{v}_{th} = (\frac{kT}{2\pi m^*})^{1/2}$

is the thermal velocity of injected holes; the minus (plus) sign holds if the net current flows into (out of) the semiconductor bulk. Equation (4.1) is obtained from the assumption that the emission current from the metal surface is not affected by the physical conditions of the adjacent semiconductor. The boundary concentration as given by Eq. (4.1) reduces to zero at contact saturation current which does not seem to be physically justifiable.

At the present time, the boundary conditions have not been adequately described for purposes of an accurate investigation of the electrical behavior of MSM structures. In an attempt to arrive at a proper formulation of the boundary conditions at both MS contacts, the flux interchange between the metal and neighboring semiconductor has been theoretically investigated and is presented in the next section.

4.2 Current Dependent Boundary Concentration

The effect of surface recombination and carrier scattering on the charge distribution in the interior of the semiconductor may be investigated by considering the flux interchange between the metal and the semiconductor bulk via an intervening interface transition layer. The transition of the physical parameters between those of the semiconductor bulk and those of the metal is assumed to occur within a thin interfacial layer formed around the metallurgical junction of the MS contact as illustrated in Fig. 4.1. The width of the interfacial layer is assumed to be of

the order of one mean free path of injected holes ($\sim$ 50 Å). In Fig. 4.1, MM' and SS' are the metal and semiconductor interface boundaries, respectively. The reflection coefficient r, at the metal surface, is defined as the probability that a single hole in a single collision with the metal atoms will be sent back to the semiconductor rather than entering the metal. Likewise, the reflection coefficient b, is defined as the probability that a single hole upon entering the semiconductor bulk from the metal side is back scattered and reappears at the metal surface. A and G are the net fluxes entering the interfacial layer from the semiconductor and the metal sides. The total flux F_1 flowing from the metal boundary MM' towards the semiconductor boundary SS',

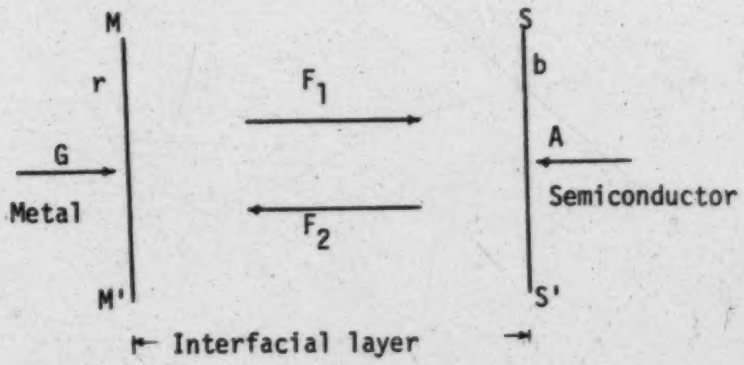

Fig. 4.1 Flux interchange at the interfacial boundary layer

and the total flux F_2 flowing in the opposite direction can be obtained by noting that F_1 is made up of a transmitted part of the incident flux G, plus that part of F_2 which is reflected by the metal suface, whereby

$$F_1 = (1 - r)G + rF_2 \tag{4.2}$$

Similarly

$$F_2 = (1 - b)A + bF_1 \tag{4.3}$$

Solving Eqs. (4.2) and (4.3) for F_1 and F_2, gives

$$F_1 = \frac{(1-r)}{(1-rb)} G + \frac{(1-b)r}{(1-rb)} A \tag{4.4}$$

$$F_2 = \frac{(1-r)b}{(1-rb)} G + \frac{(1-b)}{(1-rb)} A \tag{4.5}$$

The total flux, A_{sem}, flowing from the semiconductor boundary SS' into the interior of the semiconductor is made up of the transmitted part of F_1 plus the reflected part of A, i.e.

$$A_{sem} = (1-b)F_1 + bA \tag{4.6}$$

Similarly, the total flux, G_m, leaving the metal surface to the interior of the metal is given by

$$G_m = (1-r)F_2 + rG \tag{4.7}$$

The total conduction current, J_c, in the interfacial layer is made up of the difference between the total fluxes flowing in both directions, i.e.,

$$J_c = q(F_1 - F_2) \tag{4.8}$$

According to the current continuity requirement, the total conduction current at any particular boundary is constant, i.e.,

$$(G - G_m) = (A_{sem} - A) = (F_1 - F_2) = \frac{J_c}{q} \tag{4.9}$$

In terms of the total incident fluxes A and G, and from Eqs. (4.4), (4.5) and (4.8), the total conduction current can be expressed as

$$J_c = \frac{q(1-b)(1-r)}{(1-rb)}(G-A) \tag{4.10}$$

In thermal-equilibrium, when no net current flows, the total flux crossing the interfacial layer in one direction must be equal to the flux in the opposite direction, i.e.

$$F_{10} = F_{20}, \quad G_m = G_o, \quad A_{sem} = A_o \tag{4.11a}$$

and from Eq. (4.10),

$$A_o = G_o \tag{4.11b}$$

For an MS contact with a barrier height of a few kT, the thermal equilibrium boundary concentration at the SS' boundary is given by Eq. (2.1) as

$$p_{Bo} = N_v \exp - (\phi_p/kT) \qquad (4.12)$$

Since $p_{Bo} << N_v$, the Maxwell-Boltzmann distribution function describes well the properties of the ideal gas of injected holes [53]. According to the equilibrium theory of an ideal gas, one half of the injected holes moves in the positive x direction, while the other half moves in the opposite direction (one dimensional model only is considered), and the average velocity of injected holes which is the same in both directions is given by

$$\bar{v}_{th} = \frac{\bar{C}}{2} \qquad (4.13)$$

where $\bar{C} \equiv (\frac{8kT}{\pi m^*})^{1/2}$ is the mean thermal velocity [53]. Consequently the thermal-equilibrium fluxes A_o and G_o are given by

$$A_o = G_o = \frac{p_{Bo}}{2} \frac{\bar{C}}{2} = \frac{p_{Bo}\bar{C}}{4} \qquad (4.14)$$

If a net current flows across the MS contacts of the MSM structure (as a result of an applied voltage), the thermal equilibrium is disturbed and the two fluxes crossing the boundary layer are no longer equal. Since there is a huge reservoir of free carriers in the metal side, the physical conditions (e.g. carrier concentration, electric field and potential energy distribution) are unaffected by any current flow and, therefore, the total flux G remains practically unchanged from its thermal-equilibrium value, i.e.

$$G = G_o = \frac{p_{Bo}\bar{C}}{4} \tag{4.15}$$

In general, the distribution function of injected holes, in the semiconductor side, deviates from the Maxwellian form due to the current flow. On average, there will be p_J holes at the semiconductor surface SS' moving with average velocity $\bar{v}_J$ in the positive x direction and p_J' holes moving with average velocity $\bar{v}_J'$ in the opposite direction. Thus,

$$A_{sem} = \bar{v}_J p_J \quad ; \quad A = \bar{v}_J' p_J' \tag{4.16a}$$

and

$$p_J + p_J' = p_{BJ} \quad ; \quad (A_{sem} - A) = \frac{J_c}{q} \tag{4.16b}$$

where p_{BJ}, is the interface boundary concentration of injected holes at a given current level. According to Eqs. (4.16a) and (4.16b), the interface concentration p_{BJ}, is

$$p_{BJ} = \frac{A_{sem}}{\bar{v}_J} + \frac{A}{\bar{v}_J'} \tag{4.17}$$

Solving Eqs. (4.4), (4.5), (4.6), (4.8) and (4.15) for A and A_{sem}, one obtains

$$A = \frac{(1-rb)}{(1-r)(1-b)} \left(\mp \frac{|J_c|}{q}\right) + \frac{p_{Bo}\bar{C}}{4} \tag{4.18}$$

$$A_{sem} = \frac{p_{Bo}\bar{C}}{4} - \frac{r+b-2rb}{(1-r)(1-b)} \left(\mp \frac{|J_c|}{q}\right) \tag{4.19}$$

Substituting Eqs.(4.17) and (4.18) into Eq. (4.16) yields

$$p_{BJ} = \frac{1}{\bar{v}_J}\left\{\frac{p_{Bo}\bar{C}}{4}\left(1+\frac{1}{\alpha}\right) \mp \frac{(1/\alpha)(1-rb)+(r+b-2rb)}{(1-r)(1-b)}\frac{|J_c|}{q}\right\} \tag{4.20}$$

where $\alpha \equiv \frac{\bar{v}_J'}{\bar{v}_J}$ is a numerical factor of the order of unity, and minus (plus) sign holds if the net carrier flux flows into (out of) the semiconductor bulk.

Expression (4.20), is a general current dependent boundary concentration at both forward and reverse biased contacts. However, if the net current density is small compared to the contact emission current $\frac{qp_{Bo}\bar{C}}{4}$, the hole concentration at the semiconductor surface SS' is scarcely changed by the current flow and the distribution function of injected holes deviates only slightly from Maxwellian form. Therefore,

$$\bar{v}_J = \bar{v}_J' = \frac{\bar{C}}{2} \; ; \; \alpha = 1 \tag{4.21}$$

while p_J' will be less than p_J to satisfy the equation

$$(p_J - p_J') = \frac{J_c}{q(\frac{\bar{C}}{2})} \tag{4.22}$$

At current densities of the order of the contact emission current $\frac{qp_{Bo}\bar{C}}{4}$, the distribution function of injected holes is highly disturbed from Maxwellian and the system is far from the thermal-equilibrium one. The distribution function describing

such a system is dependent on the particular Schottky barrier. For Schottky barriers with thin interfacial layers, Stratton [36], has shown that the distribution function of electrons deviates only slightly from Maxwellian if elastic phonon interactions dominate the electron scattering mechanism. In a study on the diffusion of hot and cold electrons in Schottky barriers, with thin interfacial layer, Stratton has shown that for small forward bias, the electron temperature, T_e, is close to the crystal lattice temperature, T_c, everywhere in the barrier region. For large reverse bias, the electron temperature peaks close to the MS interface and its maximum value significantly exceeds the crystal temperature. For large forward bias, on the other hand, T_e becomes slightly less than T_c (not more than 30%). Interpreting Stratton's results for the MSM structures, one might expect that in the injecting contact region the temperature of injected holes, T_p, is close to T_c independent of the amplitude of the conduction current, and, in the collecting contact barrier region, T_p is expected to be significantly above T_c. Assuming that a single, elastic, electron-phonon scattering mechanism takes place at the MS interface layer, the distribution function of injected holes can be assumed to remain Maxwellian even at high currents and hence

$$\bar{v}_J = \bar{v}'_J = \frac{\bar{C}_p}{2} \; ; \; \alpha = 1 \qquad (4.23)$$

where $\bar{C}_p = \sqrt{\frac{8kT_p}{\pi m^*}}$ is the mean thermal velocity of injected holes

and T_p is the hole temperature which can be different at the two MS interfaces. Applying the preceding argument to Eq. (4.20), the interface boundary concentration becomes

$$p_{BJ} = p_{Bo} \frac{\bar{C}}{\bar{C}_p} \mp \frac{2J_c}{q\bar{C}_p} \frac{1+r+b-3rb}{(1-r)(1-b)} \tag{4.24}$$

Equation (4.18) shows that the flux A entering the interfacial layer from the semiconductor bulk decreases as the net conduction current J_c increases. If the physical conditions in the semiconductor are such that no flux from the semiconductor bulk enters the interfacial layer, i.e., A = 0, the saturation current

$$J_{sat} = \frac{qp_{Bo}\bar{C}}{4} \frac{(1-b)(1-r)}{(1-br)} \tag{4.25}$$

will be reached. Combining Eqs. (4.24) and (4.25), the boundary concentration may be written as

$$p_{BJ} = p_{Bo} \frac{\bar{C}}{\bar{C}_p} \left(1 \mp \frac{J_c}{J_{sat}}\right) \pm \frac{2J_c}{q\bar{C}_p} \tag{4.26}$$

where the upper (lower) signs hold for the injecting (collecting) contact.

Substituting from Eqs. (4.12) and (4.13) for p_{Bo} and $\bar{C}$ into Eq. (4.25), the saturation current density takes the form

$$J_{sat} = A^* \frac{(1-r)(1-b)}{(1-rb)} T^2 \exp - \frac{\phi_{pB}}{kT} \tag{4.27}$$

where $A^* \equiv \frac{4\pi qk^2 m_p^*}{h^2}$, is the Richardson constant given by Crowell [32].

The expression $\frac{(1-r)(1-b)}{(1-rb)} A^*$ closely resembles the effective Richardson constant, A^{**} discussed in Chapter II.

According to Eq. (4.26), the boundary concentration p_{BJ}, depends on the physical properties of the ideal MS contact (which determine the equilibrium contact concentration p_{Bo}), the temperature of injected carriers (which determines the carrier thermal velocity $\bar{C}_p$), the properties of the interfacial layer (which determines the saturation current), and the conduction current. As will be shown in the numerical study (to be described in the next chapter), the physical properties of the MSM structure are dominated by the physical conditions of the forward biased injecting contact. At this contact, the temperature of injected holes deviates only slightly from the crystal temperature, hence $\bar{C}_p$ can be well approximated by $\bar{C}$. Thus, Eq. 4.26 reduces to

$$p_{BJ} = p_{Bo}\left(1 \mp \frac{J_c}{J_{sat}}\right) \pm \frac{2J_c}{q\bar{C}} \qquad (4.28)$$

To obtain the boundary concentration at various current densities, the saturation current density must be determined first.

The saturation current can be theoretically evaluated by investigating the charge transport in the interfacial layer. For accurate transport studies, the scattering processes of injected holes by optical and acoustical phonons (caused by the vibration of the crystal lattice) and the quantum mechanical reflection process must be taken into consideration. On the other hand, the saturation current density may be obtained from the measured J-V

characteristic of a particular structure. It is not the aim of this thesis to describe the transport properties in the interface layer, hence the measured saturation current density will be used here to determine the boundary concentration. For PtSi-nSi contacts, the measured saturation current density of injected holes, J_{st} = 200 A cm^{-2}, has been reported by Andrews and Lepselter [42]. The boundary concentrations for PtSi-nSi-PtSi (with J_{st} = 200 A cm^{-2}), as given by Eq. 4-27 are thus reduced to

$$p_{BJ} = p_{Bo} \mp \lambda J_c \tag{4.29}$$

where $\lambda = (\frac{p_{Bo}}{J_{sat}} - \frac{1}{qC}) = 0.2334 \times 10^{12} A^{-1} cm^{-1}$.

The above relations have been derived for the case of steady state dc charge transport, under the assumption that, for currents up to saturation level, the mean thermal velocity of holes crossing the MS interface layer and the reflection probability for holes incident on the semiconductor boundary, b, and the metal boundary, r, remain unchanged.

If an ac voltage is superimposed upon the dc bias, an alternating current will flow through the structure, and the boundary concentration becomes time dependent. The time dependent boundary concentrations at the two MS interfaces of the PtSi-nSi-PtSi structure, may be obtained from Eq. (4.28) as

$$p_B(J(t)) = p_{Bo} \mp \lambda J_c(x_B, t) \tag{4.30}$$

Under small signal conditions, the ac boundary concentration reduces to

$$\tilde{p}_B(J) = \mp \lambda \tilde{J}_c(x_B) \qquad (4.31)$$

In Eqs. (4.29) and (4.30), x_B is the position coordinate of the MS interface and tilde denotes small signal quantities.

In most of the small signal studies of punch-through transit time structures, it is assumed that the boundary concentration is not affected by the ac conduction current [10,11,16,17,20,21]. To investigate this assumption, a numerical factor k has been introduced in Eq. (4.30), which takes the values between zero and unity. k = 1, implies that the carrier concentration is fully affected by the conduction current as in dc case. k = 0, assumes that the boundary concentration is not changed by the ac conduction current. The microwave activity of the MSM structure is found to be affected by the variation of the ac boundary concentration at the injecting contact. The detailed results of such an effect will be presented in Chapter IX.

CHAPTER V

MATHEMATICAL MODEL AND NUMERICAL SOLUTION

5.1 Mathematical Model

(a) Charge transport equations

The one dimensional MSM structure is shown in Fig. 5.1, in which the coordinates 0 and L represent the injecting and collecting contacts, respectively. The distribution of mobile holes and the electric field profile within the MSM structures can be obtained by solving two basic equations, namely the continuity equation for holes and the Poisson equation. For punched-through MSM structures, these equations (Eqs. 3.21 and 3.20) take the form

$$\frac{\partial p(x,t)}{\partial t} = -\frac{1}{q}\frac{\partial J_p(x,t)}{\partial x} \tag{5.1}$$

$$\frac{\partial E(x,t)}{\partial x} = \frac{q}{\epsilon}(N_D + p(x,t)) \tag{5.2}$$

where,

$$J_c(x,t) = q\mu(E)p(x,t)E(x,t) - qD_p\frac{\partial p(x,t)}{\partial x} \tag{5.3}$$

Boundary conditions are imposed at the contacts and are given in terms of the current-dependent boundary concentrations, as

$$p_B(J_c) = p_{Bo}\left(1 \mp \frac{J_c}{J_{sat}}\right) \pm \frac{2J_c}{q\bar{c}} \qquad (5.4)$$

where the upper (lower) signs hold for the injecting (collecting) contact.

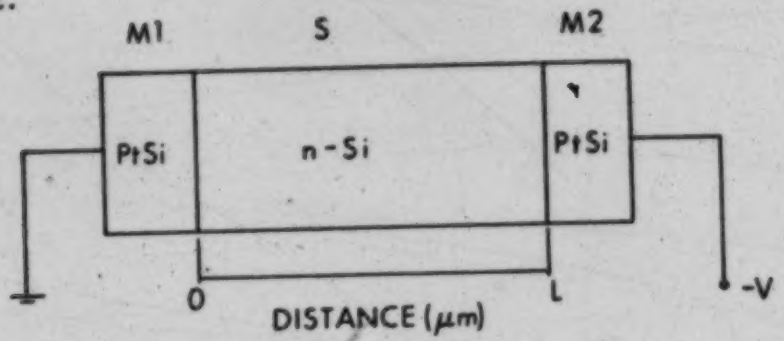

Fig. 5.1 One dimensional MSM Structure

(b) Mobility expression

The carrier mobility is one of the fundamental parameters that can directly affect the electrical behavior of the MSM structure. It is necessary, therefore, to include in the analysis, the variation of the hole mobility with the electric field E and the doping concentration N_D. According to the physical model described in Chapter III, the carrier mobility is assumed to be constant in the injection region, while in the rest of the semiconductor region the carrier mobility is approximated by the following expression [25]

$$\left(\frac{\mu_L}{\mu}\right)^2 = 1 + \left(\frac{N_D}{N_D/S+N}\right) + \frac{(E/A)^2}{F+(E/A)} + (E/B)^2 \qquad (5.5)$$

The room temperature values of the above quantities are:

μ_ℓ (low field mobility) = 480 $cm^2V^{-1}sec^{-1}$, N = 4 x 10^{16} cm^{-3}, S = 81. A = 6.1 x 10^3 Vcm^{-1}, F = 1.6 and B = 2.5 x 10^4 Vcm^{-1}. As the temperature increases, μ_ℓ decreases, the region of constant mobility extends to higher electric fields, the drift velocity saturates at higher electric fields (saturation drift velocity is also referred to as scattering limited velocity)and the scattering limited velocity seems to be slightly reduced [66]. Assuming that holes reach a scattering limited velocity of 7 x 10^6 cm sec^{-1} at an electric field strength of 2 x 10^5 Vcm^{-1} and taking into account the previously mentioned features (by extrapolating the available measured data),another set of values in expression (5.5) is obtained for T = 423 °K as μ_ℓ = 200 $cm^2V^{-1}sec^{-1}$, N = 4 x 10^{16}, S = 81, A = 9 x 10^3 Vcm^{-1}, F = 1.1 and B = 6.2 x 10^4 Vcm^{-1}. Equation 5.5 with the set of values obtained at T = 423 °K is used in the analysis to investigate the temperature effects on the electrical behavior of the MSM structures.

To obtain the J-V characteristic and the structure ac impedance (admittance), the relation between the electrostatic potential and the electric field strength

$$\frac{\partial V(x,t)}{\partial x} = - E(x,t) \qquad (5.6)$$

is used in the analysis.

The analytical formulation and the numerical method of solution of the mathematical model will be described in the remainder of this chapter. The analysis to be discussed here is restricted

to the steady state dc and small-signal ac conditions.

5.2 Limitation of Analytical Solutions

The fundamental equations mentioned in the preceding section are generally non-linear differential equations and analytical solutions in closed form cannot be found. In order to obtain analytical solutions the following simplifying assumptions were adopted in various studies:

(1) The dependence of the carrier mobility upon the electric field and doping concentration is simplified by assuming constant drift velocity throughout the whole semiconductor region [14,16].

(2) The diffusion component of the conduction current is neglected [5,10,16,17].

(3) Simplified boundary conditions are introduced in the interior of the structure instead of properly formulated boundary conditions at the contacts [5,10].

The above assumptions are usually unsatisfactory and can lead to serious errors in describing the actual behavior of the device. Perhaps the most unsatisfactory assumption of all is the first, since the MSM structures are usually made on lightly doped semiconductors, and hence a low-field region (where the drift velocity is field-dependent) always exists. Other assumptions become unsatisfactory when describing high current operation (which is usually the case for high frequency structures).

Computer aided numerical solutions represent an alternative approach to the problem; the final aim is to achieve an "exact" solution of the most general character without any of the conventional assumptions being introduced. The "exact" solution allows the quantitative comparison with the analytical first order theories and hence the validity of each simplifying assumption can be investigated.

Serious difficulties are also encountered in numerical investigations and have rendered the available numerical techniques unsuitable for obtaining the desired "exact" solution. These difficulties, which are encountered even in the simple MS junction case treated by Macdonald [35], are responsible for the acceptance of some of the conventional assumptions in the PN junction theory [54-56]. Although more general and complete formulation of the problem may be devised, solution of the simplified set of equations that takes into account carrier diffusion, the dependence of carrier mobility upon electric field and doping concentration together with properly defined boundary conditions at the contact will here be referred to as the "exact" solution.

5.3 DC and Small-Signal Boundary-Value Problems

Under dc conditions the fundamental equations (Eqs. (5.1 - (5.3)) simplify to the following forms

$$\frac{dp_o(x)}{dx} = \frac{\mu_o(E)E_o(X)}{D_p} p_o(x) - \frac{J_c(x)}{qD_p} \qquad (5.7)$$

$$\frac{dE_o(x)}{dx} = \frac{q}{\varepsilon}(N_D + p_o(x)) \tag{5.8}$$

and

$$J_c(x) = J_c \tag{5.9}$$

Equation (5.7) has been rearranged in a form more convenient for numerical computations. The dc boundary condition is

$$p_B(J_c) = p_{Bo}(1 \mp \frac{J_c}{J_{st}}) \pm \frac{2J_c}{qC} \tag{5.10}$$

where upper (lower) signs hold for the injecting (collecting) contact. Regarding the conduction current J_c as a parameter Eqs. (5.7) - (5.10) form a two-point boundary value problem; its solution yields the dc behavior of the structure. The dc solution is required in this work for two reasons:

(1) To study the dc properties and to describe the static characteristic of the MS structures.

(2) To furnish the initial values necessary for performing the small-signal solution.

In small-signal operation, the fundamental equations together with the boundary conditions, may be written in the following form (more convenient for numerical studies):

$$\frac{d\tilde{p}(x)}{dx} = \frac{v_o(x)\tilde{p}(x)}{D_p} + (\frac{p_o(x)\mu_d(x)}{D_p} + j\omega\varepsilon)\tilde{E} - \frac{\tilde{J}_T}{qD_p} \tag{5.11}$$

$$\frac{d\tilde{E}(x)}{dx} = \frac{q}{\varepsilon}\tilde{p}(x) \tag{5.12}$$

and $$\tilde{\rho}_B = \mp \left(\frac{\rho_{Bo}}{J_{st}} - \frac{2}{qC}\right)\tilde{J}_c \qquad (5.13)$$

Regarding the total current as a parameter Eqs. (5.11) and (5.13) form a two-point boundary value problem, which is similar in many respects to the dc problem. Consequently the same numerical technique can be used for both the dc and small-signal cases. The numerical method of solution used to solve the boundary value problems cited above will be described in the next section.

5.4 Numerical Techniques for the Solution of Boundary-Value Problems

The usual algorithms for the solution of boundary -value problems fall into two general classes: the finite-difference methods and the shooting method.

The finite-difference methods involve approximation of the differential equations at a finite number of base points in the total interval; each derivative is replaced by a difference operator. The system of differential equations is transformed to a system of simultaneous algebraic equations. If the system of differential equations is linear, then the set of equations generated is also linear. The solution of the linear system of algebraic equations is simple and can easily be obtained. Unfortunately, when the differential equations are non-linear, the system of finite difference equations is also non-linear. The

generation of any solution of non-linear equations may be very difficult, especially when many base points are used. In some cases [57], one can linearize the equations, solve the equations iteratively, then relinearize about the new solution, find a new solution iteratively, etc. In effect, a complex problem has been replaced by another problem which is somewhat less complex.

The shooting methods reduce the solution of a boundary value problem to the iterative solution of an initial-value problem [58]. The usual approach involves a trial-and-error procedure. That boundary point having the most known conditions is selected as the initial point. Any other missing initial conditions are assumed and the initial-value problem is solved using one of the step-by-step procedures (e.g. Runge Kutta algorithm, Euler method, Hamming Predict or corrector method, etc.,). Unless the computed solution agrees with the known boundary condition (unlikely on the first try), the initial conditions are adjusted and the problem is solved again. The process is repeated until the assumed initial conditions yield, within the specified tolerances, a solution that agrees with the known boundary conditions.

To use the shooting methods for solving boundary value problems, the solution of the initial value problems must be obtained with sufficient accuracy such that the subsequent decisions based on them can be justified. Such a requirement is not always warranted. It can happen that a small variation in the initial conditions results in large variations in the values obtained by

the solution. Therefore, even a small error (e.g. round off) at one point can make the subsequently computed values at another point meaningless. The initial value problems for a particular set of differential equations can be "unstable" even though boundary value problems for the same set of equations may be perfectly stable. It is not advisable, in these cases, to attempt the solution of the boundary problem via a sequence of initial value problems, but it would be preferable to use a method that approximates the boundary value problem (e.g. finite-difference methods).

The solution of two-point boundary value problems (discussed in the previous section) by means of the initial value method (if stable and accurate solutions can be found) may be carried out in either direction (i.e. from 0 to L or from L to 0) since the conditions at both contacts are symmetrical. For unipolar charge transport devices (e.g. punched-through MSM structures and their semiconductor alternatives), a stable solution for the two-boundary value problem can always be found by initial-value methods. In the case of bipolar transport devices (general PN junctions) where electrons and holes contribute to the charge transport, the forward solution (from 0 to L) or the backward solution (from L to 0), using the initial-value approach is usually unstable. In these devices, the holes are responsible for the instability of the forward solution, while the electrons are responsible for the instability of the backward solution.

In this study, a one-step method using a Runge-Kutta fourth

order algorithmhas been used to solve the dc and small-signal two-point boundary value problems. An accurate and stable solution has been obtained by performing backward integration (i.e. from the reverse-biased contact towards the forward-biased contact). A detailed analysis of the accuracy and stability of the obtained solution is described in Appendix A. In the next section, the outline of the numerical method being used will be described.

5.5 Outline of the Numerical Method

The complete iteration scheme of the numerical solution for the dc two-point boundary value problem is shown in Fig. 5.2. The structure's physical parameters (e.g. N_D and L) together with the total conduction current density, J_c, are first specified and the applied terminal voltage is determined at the completion of the integration procedure. To begin the computation, an initial guess for the electric field, E_o, at the reverse biased contact is assigned. The hole mobility, $\mu(E)$, and the drift velocity v_o are computed as a function of position by using Eq. (5.5). Knowing these values Eqs. (5.7) and (5.8) are solved simultaneously by using RKGfourth order method. The integration of Eqs. (5.7) and (5.8) is continued until the desired semiconductor width has been reached, where it is checked whether or not the specified boundary condition (Eq. 5.4) is met. If the boundary condition requirement has not been closely met (within a specified tolerance) another guess value for E_o at the contact is

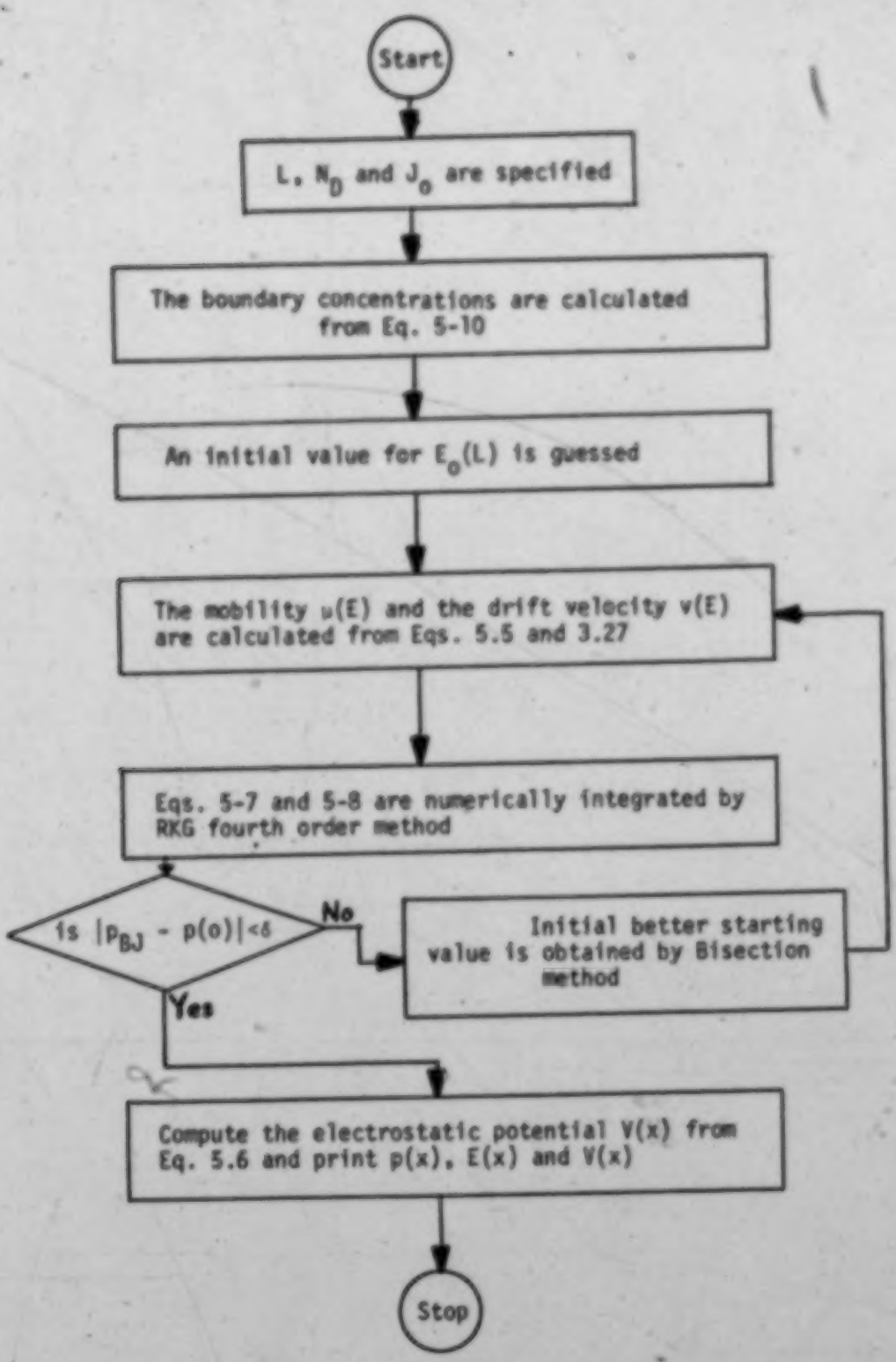
Start
L, N_D and J_o are specified
The boundary concentrations are calculated from Eq. 5-10
An initial value for $E_o(L)$ is guessed
The mobility μ(E) and the drift velocity v(E) are calculated from Eqs. 5.5 and 3.27
Eqs. 5-7 and 5-8 are numerically integrated by RKG fourth order method
is $|p_{BJ} - p(o)| < \delta$
No
Initial better starting value is obtained by Bisection method
Yes
Compute the electrostatic potential V(x) from Eq. 5.6 and print p(x), E(x) and V(x)
Stop

Fig. 5.2: Overall Iterative Scheme for DC Calculations.

assigned and the numerical integration is repeated until the solution p(x), satisfies the proper boundary condition.

Although the initial value $E_o(L)$ which satisfies the desired boundary condition p_{BJ} at $x = L$ for a given choice of J and L can often be estimated quite closely, obtaining accurate results usually requires several iterations. In order to hasten the iteration procedure, the bisection iteration method is used here [61].

The complete iteration scheme of the numerical method of solution for the small-signal boundary value problem is shown in Fig. 5.3. The numerical method described for the dc case can be applied to the small-signal case with slight modification. First, the dc solution for a specific structure parameter and dc conduction current density is obtained, then the dc quantities, $p_o(x)$ and $E_o(x)$, needed in the small-signal computation, are approximated by natural cubic spline polynomials [59]. To obtain such polynomials, the total semiconductor width is divided into (N-1) subintervals by N points (abscissai). The set of N functional values $F_1, F_2, \ldots\ldots, F_N$ (for p(x) and E(x)) and the corresponding coordinates $x_1, x_2, \ldots\ldots, x_N$ are then fed to a natural-cubic spline subroutine and an output array C of dimension (3,(N-1)) corresponding to p_o and E_o is obtained. In the i^{th} interval $[x_i, x_{i+1}]$, the spline interpolate, F(x) is given by:

$$F(x) = C_{3,i}(x-x_i)^3 + C_{2,i}(x-x_i)^2 + C_{1,i}(x-x_i) + F(x_i) \qquad (5.14)$$

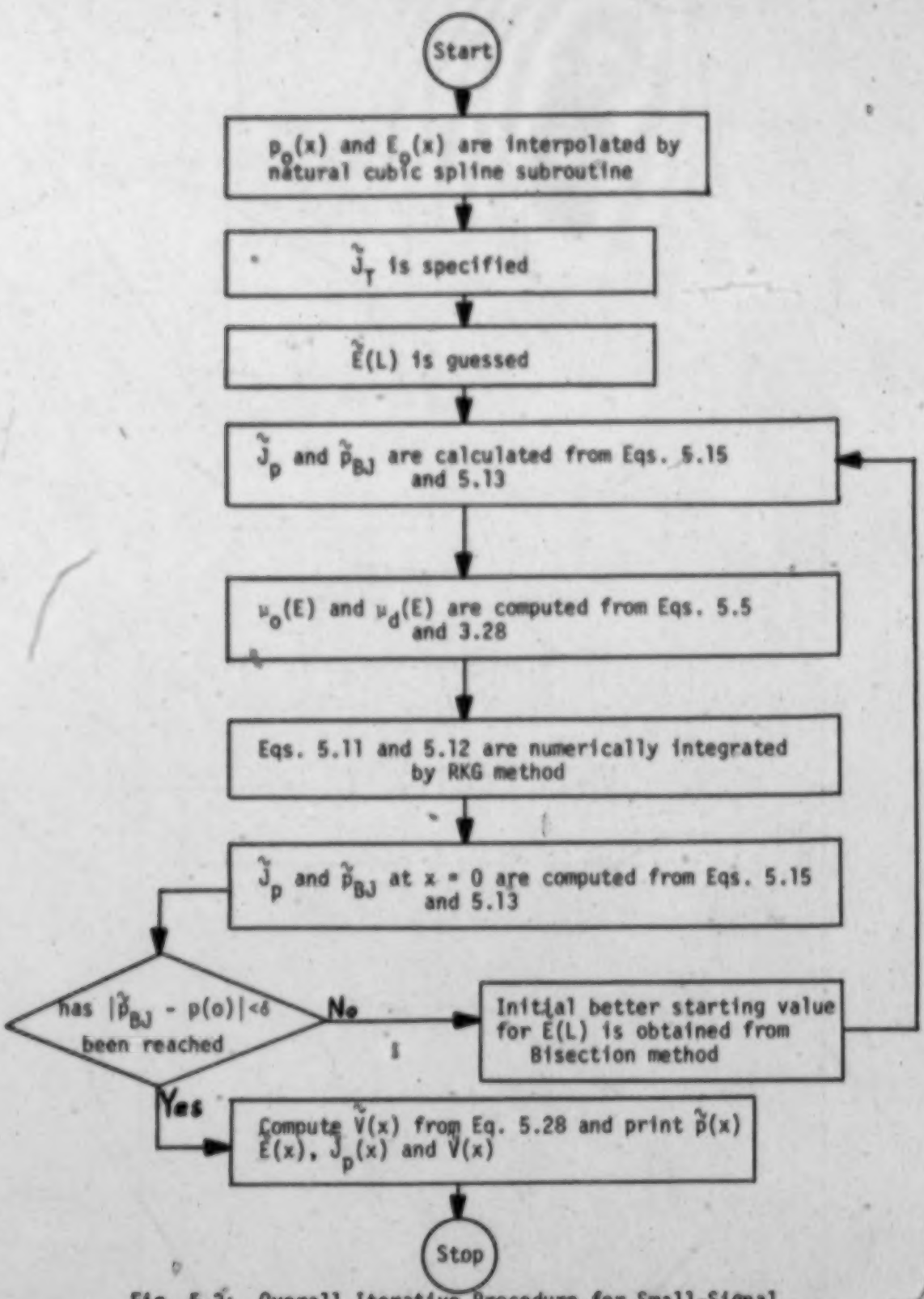
Start
$p_o(x)$ and $E_o(x)$ are interpolated by natural cubic spline subroutine
$\tilde{J}_T$ is specified
$\tilde{E}(L)$ is guessed
$\tilde{J}_p$ and $\tilde{p}_{BJ}$ are calculated from Eqs. 5.15 and 5.13
$\mu_o(E)$ and $\mu_d(E)$ are computed from Eqs. 5.5 and 3.28
Eqs. 5.11 and 5.12 are numerically integrated by RKG method
$\tilde{J}_p$ and $\tilde{p}_{BJ}$ at x = 0 are computed from Eqs. 5.15 and 5.13
has $|\tilde{p}_{BJ} - p(o)| < \delta$ been reached
No
Initial better starting value for $\tilde{E}(L)$ is obtained from Bisection method
Yes
Compute $\tilde{V}(x)$ from Eq. 5.28 and print $\tilde{p}(x)$ $\tilde{E}(x)$, $\tilde{J}_p(x)$ and $\tilde{V}(x)$
Stop

Fig. 5.3: Overall Iterative Procedure for Small-Signal AC Calculations.

This routine was tested using data from natural cubic splines over the interval [0,1] and from these tests, near machine accuracy was obtained for all problems [60]. For our data, the interpolated values have been compared with the exactly calculated results for a number of points within each subinterval, and an agreement up to the sixth digit was obtained for all tested functional values. Having obtained the dc coefficients for $p_o(x)$ and $E_o(x)$ throughout the total specified interval, the small-signal solution can be obtained by specifying the total ac current density $\tilde{J}_T$ and the terminal ac voltage is determined at the end of the integration procedure. Also the device impedance (admittance) can then be obtained. Since the ac quantities are generally complex functions of position, $\tilde{J}_T$ is taken as a reference phasor lying in the positive real axis (i.e., $\tilde{J}_T = 1$). To begin the ac computation, an initial guess for $\tilde{E}(L)$ is assumed and the ac conduction current density $\tilde{J}_C$ at the contact is computed from the equation

$$\tilde{J}_C = \tilde{J}_T - j\omega\varepsilon\tilde{E} \qquad (5.15)$$

and the ac boundary concentration is then obtained from Eq. (5.13). The carrier dc and differential mobilities μ_o and μ_d necessary for the ac calculations are obtained from Eqs. (5.5) and (3.28) respectively. Knowing the above mentioned quantities Eqs. (5.11) and (5.12) are simultaneously solved using a RK fourth order method. The integration of (5.11) and (5.12) is continued until the end of the interval is reached where the ac conduction current $\tilde{J}_C$ is computed

from Eq. (5.15). The ac boundary concentration at the forward biased contact is then obtained from Eq. (5.13). The calculated boundary concentration is checked with the pertinent value obtained from the solution of Eq. (5.11). If the two values agree within certain specified tolerances, then the boundary condition is met and Eq. (5.6) can be integrated to obtain the terminal ac voltage. If the boundary condition is not closely met, another guess for $\tilde{E}(L)$ is assigned and the procedure is repeated until the boundary condition is closely met.

Usually a large number of iterations must be tried before the proper value is reached. The iteration procedure for the ac case is more difficult than that for the dc case. In the dc case, the quantities are real and hence a guess of one value only is required. For the ac case, on the other hand, the ac field is a phasor quantity and a pair of values must be guessed simultaneously. Unless a fairly close guess is used, the iteration procedure may not converge or may require an excessively long time for convergence. To overcome this difficulty, a close initial value for $\tilde{E}(L)$ is obtained by performing an approximate small-signal solution where the ac diffusion current component is neglected. Having obtained a reasonable guess (the outcome of the approximate solution) to start the first iteration, improved values for $\tilde{E}(L)$ are then obtained by applying the bisection iteration method [61].

In the next section, a simplified small-signal approximate solution will be described.

5.6 Approximate Small-Signal Numerical Solution

An approximate small-signal solution is needed to obtain a fairly good approximation for the ac electric field $\tilde{E}(L)$ which then can serve as an initial guess of the numerical solution. The approximate solution also helps investigation of the simplifying assumption of neglecting ac diffusion.

If the ac diffusion current is neglected, Eqs. (5.11) and (5.12) become

$$\tilde{p}(x) = \frac{1}{v_o(x)}\left[\frac{\tilde{J}_T}{q} - \left(p_o(x)\mu_d(x) - \frac{j\omega\varepsilon}{q}\right)\tilde{E}(x)\right] \qquad (5.16)$$

$$\frac{d\tilde{E}}{dx} = \frac{1}{\varepsilon v_o(x)}\left[\tilde{J}_T(x) - (qp_o(x) + j\omega\varepsilon)\tilde{E}(x)\right] \qquad (5.17)$$

which is an ordinary linear differential equation with non-constant coefficients. The solution of Eq. (5.17) is given by:

$$\tilde{E}(x) = \exp - \int_o^x (a+jb)dx' \left\{C + \frac{\tilde{J}_T}{\varepsilon}\int_o^x \left[\exp\int (a+jb)dx''\right]\frac{dx'}{v_o(x')}\right\} \qquad (5.18)$$

where

$$a(x) = \frac{qp_o(x)\mu_d(x)}{\varepsilon v_o(x)} \qquad (5.19)$$

$$b(x) = \frac{\omega}{v_o(x)} \qquad (5.20)$$

and C is the constant of integration to be determined from the initial

conditions. To obtain the solution $\tilde{E}(x)$ (of Eq. 5.18), suitable initial conditions must be properly found.

An analytical small-signal study of a punch-through p^+np^+ structure has been reported by Wright and Sultan [10]. In this study the injection region is neglected and the barrier maximum is regarded as an effective source plane. These authors have further assumed that the ac electric field at the effective source plane modulates only the charge velocity and not the charge density. Consequently the conduction current injected at the barrier maximum is in phase with the local ac electric field $\tilde{E}(o)$, i.e.

$$\tilde{J}_c(o) = \sigma\tilde{E}(o) \tag{5.21}$$

where

$$\sigma = \frac{\mu_p J_o}{v_{os}} \tag{5.22}$$

is an effective small-signal conductivity of the source plane. In Eq. (5.22) v_{os} is the dc injection velocity of mobile holes at the barrier maximum position. To obtain v_{os}, Wright and Sultan [10] have numerically integrated the dc conduction current equation and Poisson's equation by considering the barrier maximum as origin (x=0) and by using $E_o = 0$ and $\frac{dp_o}{dx} = -\frac{J_o}{\mu kT}$ at the barrier maximum as initial conditions. By selecting the value of $p_o(o)$ at the barrier maximum so as to give self-consistent solutions for both equations, they have obtained v_{os} as

$$v_{os} = -\frac{D_p}{p_o}\frac{dp_o}{dx}\Big|_{x=0} \tag{5.23}$$

The ac electric field at the effective source plane is then given by

$$\tilde{E}(o) = \frac{\tilde{J}_T}{\frac{\mu_o J_o}{v_{os}} + j\omega\varepsilon} \qquad (5.24)$$

Having obtained the initial value of the alternating small-signal electric field, Wright and Sultan have numerically integrated Poisson's equation (Eq. (5.17)) by assuming that mobile holes are injected through the barrier maximum with the velocity v_{os} and, thereafter, are considered to be transported to the opposite contact by drift alone (i.e. $v_o(x) = v_{drift}$, $x > 0$).

By applying the previous analysis of Wright and Sultan, we have found that the numerical integration of Eq. (5.17) leads to great uncertainties in the neighbourhood of the barrier maximum position. The reason for the discrepancies in the calculated results is due to the neglect of the dc carrier diffusion in the low-field region of the structure. In the vicinity of the barrier maximum position, the drift velocity is small and mobile carriers are moving through this region mainly by diffusion. If the carrier diffusion is neglected, the magnitude of the ac concentration of injected holes, $\tilde{p}(x)$, as well as the ac electric field $\tilde{E}(x)$ is too large as compared to those obtained when diffusion processes are considered.

The above discussion indicates that the carrier velocity is one of the fundamental parameters which can directly affect the electrical behavior of the structure. Analytical models which

consider drift velocity and neglect the diffusion transport mechanism yield results which differ considerably from the actual behavior of the structure. An improvement in analytical small-signal models can be obtained if the effects of carrier diffusion upon the dc velocity of injected holes is considered. In the present work, the small-signal analytical study described by Wright and Sultan has been modified to include the injection region and the dc diffusion processes in the entire semiconductor bulk. The modified model is based on the exactly calculated dc solution described in Section 5.3.In this model, the total semiconductor width is divided into two regions. The first includes the injection and low-field regions and is referred to as the diffusion affected region (the region where dc diffusion current is more than 10% of the total conduction current). The second is the drift (high-field) region where carriers are being transported by drift alone (the drift current is more than 90% of the total conduction current). In the diffusion affected region, the carrier effective velocity is defined as

$$v_{eff}(x) = \frac{J_o}{qp_o(x)} \tag{5.24}$$

which depends on both drift and diffusion. Following the physical assumption of Wright and Sultan, that no carrier modulation by the ac electric field takes place in the injection region, we thus have

$$\tilde{p}(x) = 0 \quad \text{for } 0 \leq x \leq x_m \tag{5.25}$$

where 0 and x_m are the position coordinates of the forward biased MS interface and the barrier maximum respectively. From Eq. (5.16) the ac electric field, in the injection region, is given by

$$\tilde{E}(x) = \left[\frac{\tilde{J}_T}{qv_{eff}(x)p_o(x) + j\omega\varepsilon}\right] \tag{5.26}$$

The initial value required to carry out the integration of Eq. (5.17) can be obtained from Eq. (5.26) as

$$\tilde{E}(o) = \frac{\tilde{J}_T}{\sigma(o)+j\omega\varepsilon} \tag{5.27}$$

where $\sigma(o) \equiv qv_{eff}(o)p_o(o)$, is the effective small-signal conductivity of the forward MS contact. The total ac voltage is obtained from the integration of Eq. (5.17) as

$$\tilde{V}(x) = -\int_0^x \tilde{E}(x)dx' \tag{5.28}$$

A Runge Kutta fourth order method has been used to obtain $\tilde{E}(x)$ and $\tilde{V}(x)$. The value of $\tilde{E}(L)$ can then serve as the first initial guess for the exact numerical small-signal solution.

5.7 Summary

A mathematical model for punch-through MSM structures has been described. Carrier diffusion, velocity dependence on electric field and doping concentration, and properly defined boundary conditions

at the MS contacts are included in the model. Under steady-state dc and small-signal conditions, the fundamental equations reduce to a two-point boundary value problem. A numerical method of solution for the two-point boundary value problem has been outlined. The obtained solution of this problem is referred to as the "exact" solution. To carry out the exact small signal solution a fairly close initial guess obtained from an approximate model has to be used.

CHAPTER VI

STATIC CHARACTERISTICS

Based on the mathematical model described in the previous chapter, the dc properties of a few MSM structures have been evaluated and are described in this chapter. The distribution of density of mobile holes, electric field and electrostatic potential are useful in explaining the J-V characteristic of the structure. In addition the distribution of mobile holes and electric field are required for the initial values of the small-signal solution.

The computed results of the above mentioned quantities are graphically presented and discussed for various PtSi-nSi-PtSi structures. Symmetrical structures are assumed (i.e., having the same cross-sectional area at both contacts) and all results are displayed with respect to unit cross-sectional area of the contacts. Table (6.1) is a summary of the structure parameters used in this investigation.

The room temperature dc properties of structure A (N_D = 4.4 x 10^{14} cm^{-3} and L = 10 μm) are described in the following section. The effects of the physical parameters are presented in Section 2 while the temperature effects on the dc behavior of the structure are shown in Section 3.

6.1 DC Properties and J-V Characteristic of a Typical MSM Structure

The distribution of the density of injected holes inside

TABLE 6.1

SUMMARY OF STRUCTURE PARAMETERS USED FOR THE DC STUDY

Structure	Semiconductor width, L(μm)	Doping Concentration $N_D(cm^{-3})$
A	10	4.4×10^{14}
B	10	1.2×10^{15}
C	7.9	1.2×10^{15}
D	4.8	2.5×10^{15}
E	4	4.4×10^{14}
F	4	1.2×10^{15}

the bulk of the semiconductor, at different current density levels, is shown in Fig. 6.1(a). The density of holes varies by several orders of magnitude through the semiconductor. Close to the MS contacts, a steep concentration gradient occurs within a few tenths of a micron from both contacts.Farther from the contacts, the concentration is a slowly varying function of position and becomes nearly constant. According to Fig. 6.1(a), the bulk concentration significantly increases with increasing the current density, e.g., if the current density changes from 1 to 10 $A\,cm^{-2}$, the bulk concentration increases from 10^{12} to 10^{13} cm^{-3}. Since the density of trapping states in a pure uncompensated silicon is of the order of 10^{12} cm^{-3}, the computed results should accurately characterize the real MSM structures for current densities of about 1 $A\,cm^{-2}$ and greater. In close proximity of the MS interfaces, the hole concentration changes only as the current densities approach the contact saturation value (the room temperature saturation current density of PtSi-nSi-PtSi is approximately 200 $A\,cm^{-2}$ [42]). This is clearly demonstrated by the J = 100 $A\,cm^{-2}$ curve of Fig. 6.1(a). At the forward biased contact hole concentration decreases with increasing current density, while at the reversed biased contact, this concentration increases with increasing current. The decrease of the hole concentration at the injecting contact will be shown to have a significant effect on the resulting J-V characteristic.

The electric field distribution inside the semiconductor bulk of the MSM structure, for different current density levels,

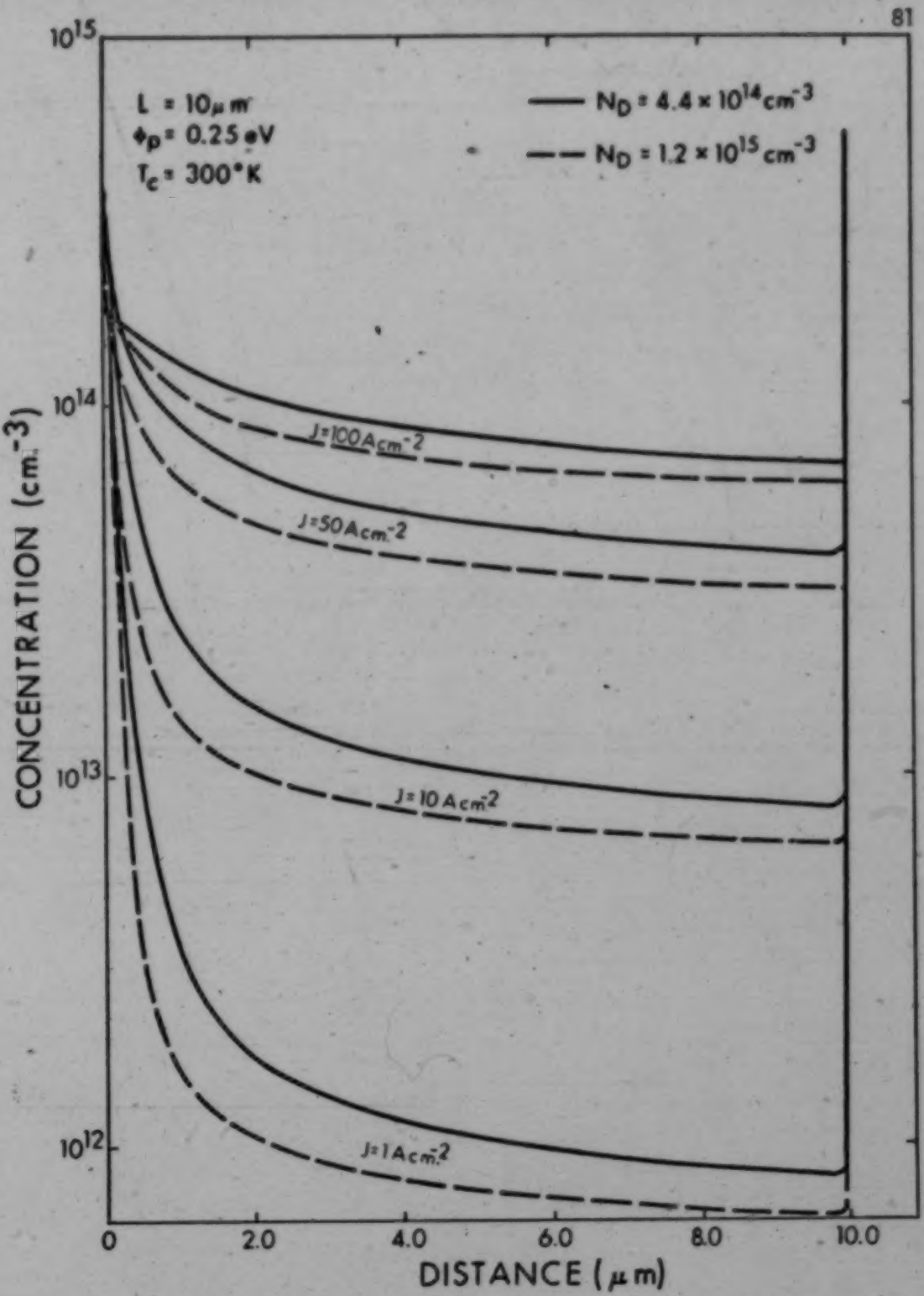

Fig. 6.1a: Concentration Profile of the Injected Mobile Holes in the Semiconductor Region for Two Different Doping Concentrations.

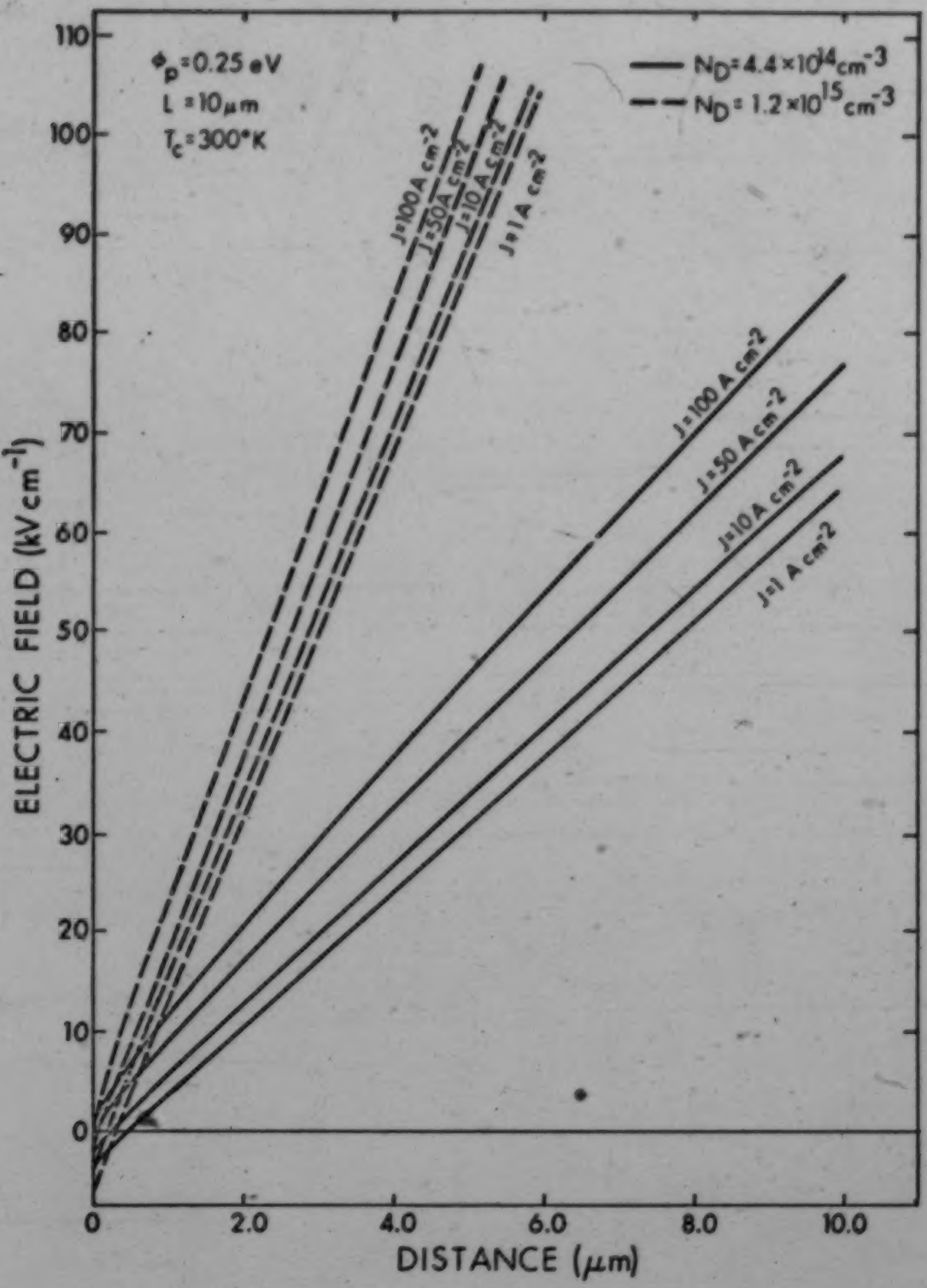

Fig. 6.1b: Corresponding Electric Field Distribution.

is illustrated in Fig. 6.1(b). At low current density levels, the electric field increases linearly in most of the semiconductor bulk, the slope being determined by the density of ionized donors. Close to both contacts, the injected holes significantly affect the electric field profile which is highly non-linear. At high currents, the non-linear region of the electric field extends farther from the contacts, and in the remainder of the semiconductor the slope of the linearly increasing fields increases with current. The slope of the electric field is determined by the background donor concentration and the density of mobile holes which is nearly constant within the region. As the current density increases, the point of zero electric field (potential maximum) shifts towards the forward biased contact (i.e. the injection region is reduced by increasing the current density). It will be shown that the reduction of the injection region by increasing the current density affects the microwave activity of the structure.

Figure 6.2 illustrates in more detail the physical conditions in the injecting contact region. The variation of the diffusion and drift current density components in the vicinity of the forward bias contact is shown in Fig. 6.2(a). Close to the contact, the diffusion current is large, and reduces very rapidly as the distance from the contact increases. At the forward contact, the drift current component is negative because carriers drift toward the contact due to the retarding field in the injection region. As the distance increases the retarding force on injected holes decreases and a point is reached where the drift current becomes exactly

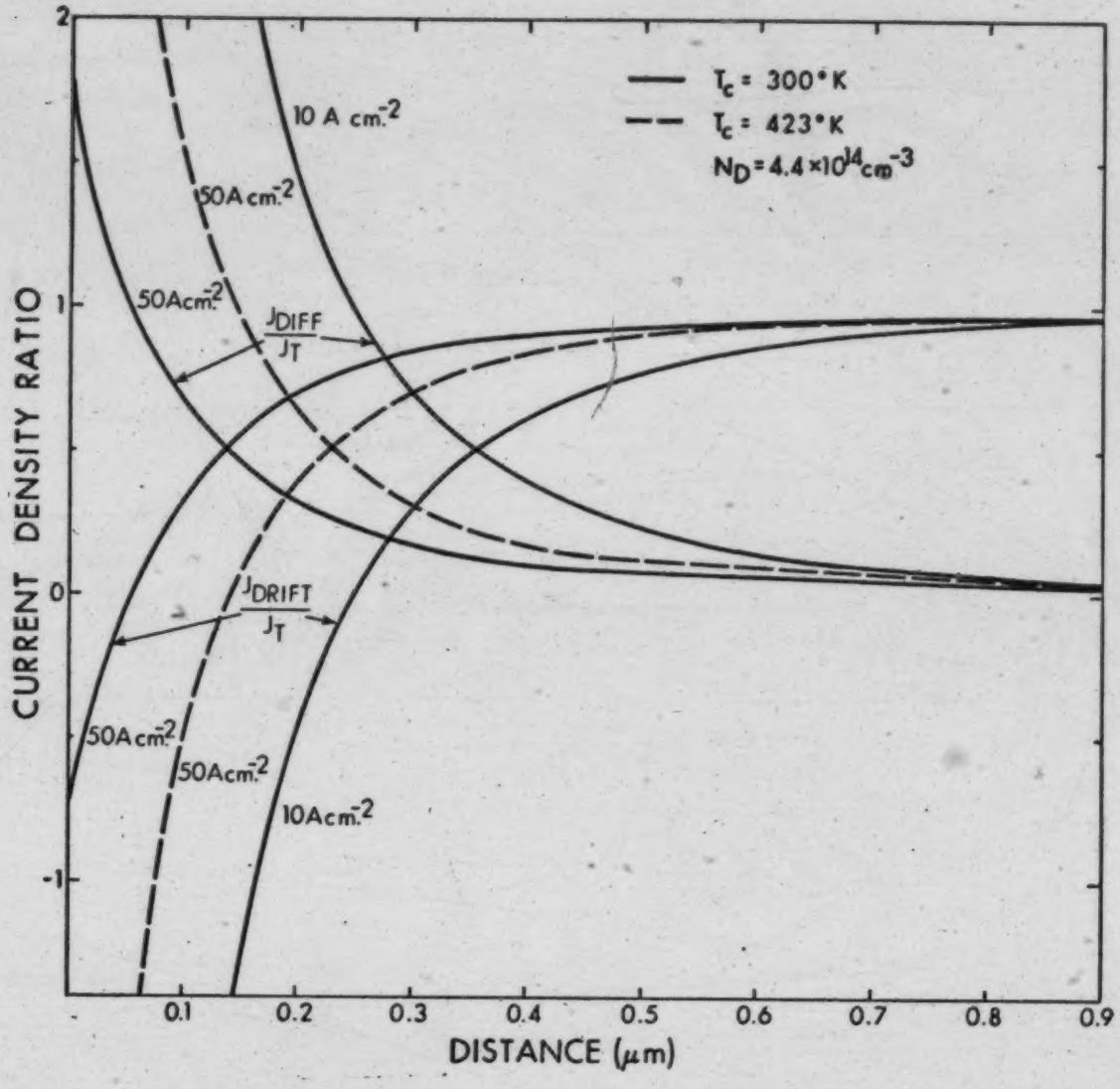

Fig. 6.2a: Drift and Diffusion Current Components (Normalized to the Total Current J_T) in the Barrier Region of the Injecting Contact, at Two Different Temperatures.

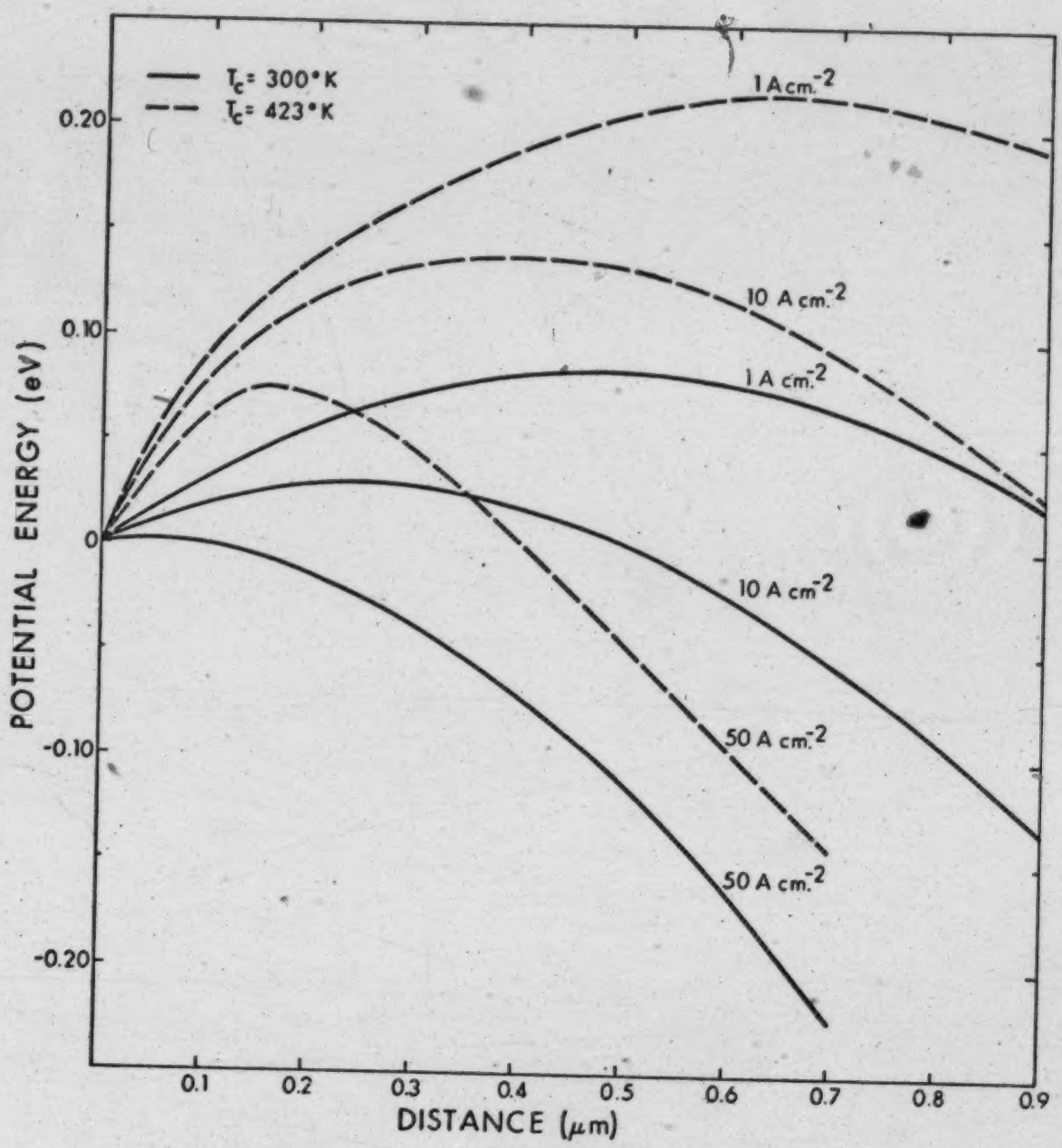

Fig. 6.2b: Corresponding Potential Energy Distribution.

equal to zero. At the point of zero drift current (due to zero electric field) the mobile holes move only by diffusion mechanism and the diffusion current is equal to the total conduction current. Beyond the zero field position ($J_{drift} = 0$), the drift current increases until a point is reached where it becomes practically equal to the total current (i.e., the diffusion current becomes negligible). The semiconductor region bounded by the forward biased contact ($x = 0$) and the point $x = x_d$, where the diffusion current component is approximately 10% of the total conduction current, is here referred to as the diffusion affected region. It is the region where carrier transport is due to both the diffusion and drift mechanisms and it includes the injection region and part of the low-field region where the carrier drift velocity is proportional to the electric field. It will be shown later that most of the power dissipation inside the MSM structure occurs within this region, and hence it significantly affects the electrical behavior of the device. As the current density increases, the width of the diffusion affected region varies from approximately 0.2 μm up to 0.8 μm depending on the physical parameters (e.g., L and N_D) of the structure. In most MSM structures, this region can become comparable to the total semiconductor width, especially for high frequency structures (with thin semiconductor width). It will also be shown later that neglecting diffusion effects in this region can lead to serious errors.

The potential energy distribution in the diffusion affected region described above is shown in Fig. 6.2(b), for three current

density levels. Above punch-through voltage, a pronounced potential energy maximum is formed close to the contact. In a manner analogous to vacuum tubes, the presence of the potential maximum controls the mobile carrier injection and will, therefore, result in the space charge reduction of the shot noise component of the conduction current. By increasing current density, the potential maximum becomes more narrow, shifts towards the injecting contact and decreases in magnitude.

The terminal voltage at different current density levels is computed numerically and the resulting features of the J-V characteristic of the MSM structure is shown in Fig. 6.3. The exponential dependence of the structure current on the applied voltage, which has been predicted and verified experimentally for low current levels [23], is clearly exhibited by the J-V characteristic of Fig. 6.3. The actual characteristic, however, begins to deviate from the exponential dependence at a certain current density level (30 Acm^{-2} for this case) due to the space charge effects of injected holes. As the current density increases further, the space charge effects become more pronounced as is clearly shown by comparison of curves (a) and (b) of Fig. 6.3. As the current density approaches the contact saturation current, the J-V characteristic levels off very rapidly due to the finite number of injected holes that can be present at the MS injecting contact. Any further increase of the terminal voltage will result in very little change of current. The maximum allowable voltage that can be applied to the MSM structure is limited by the avalanche breakdown voltage as will be explained later in this

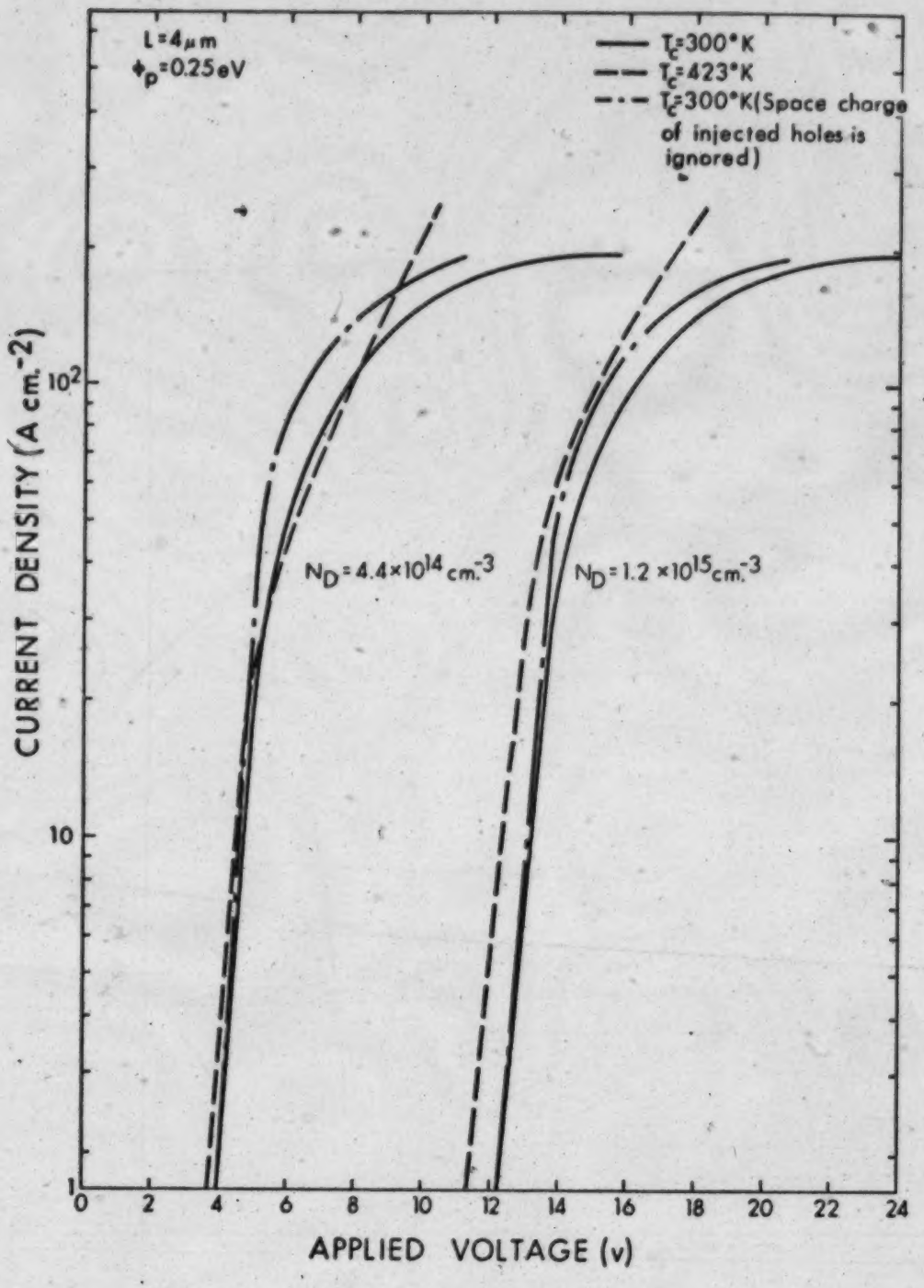

Fig. 6.3a: Current-Voltage Characteristics for Two Different Doping Concentrations and at Two Different Crystal Temperatures (L = 4 μm). Effect of Ignoring Space Charge of Injected Holes is also shown.

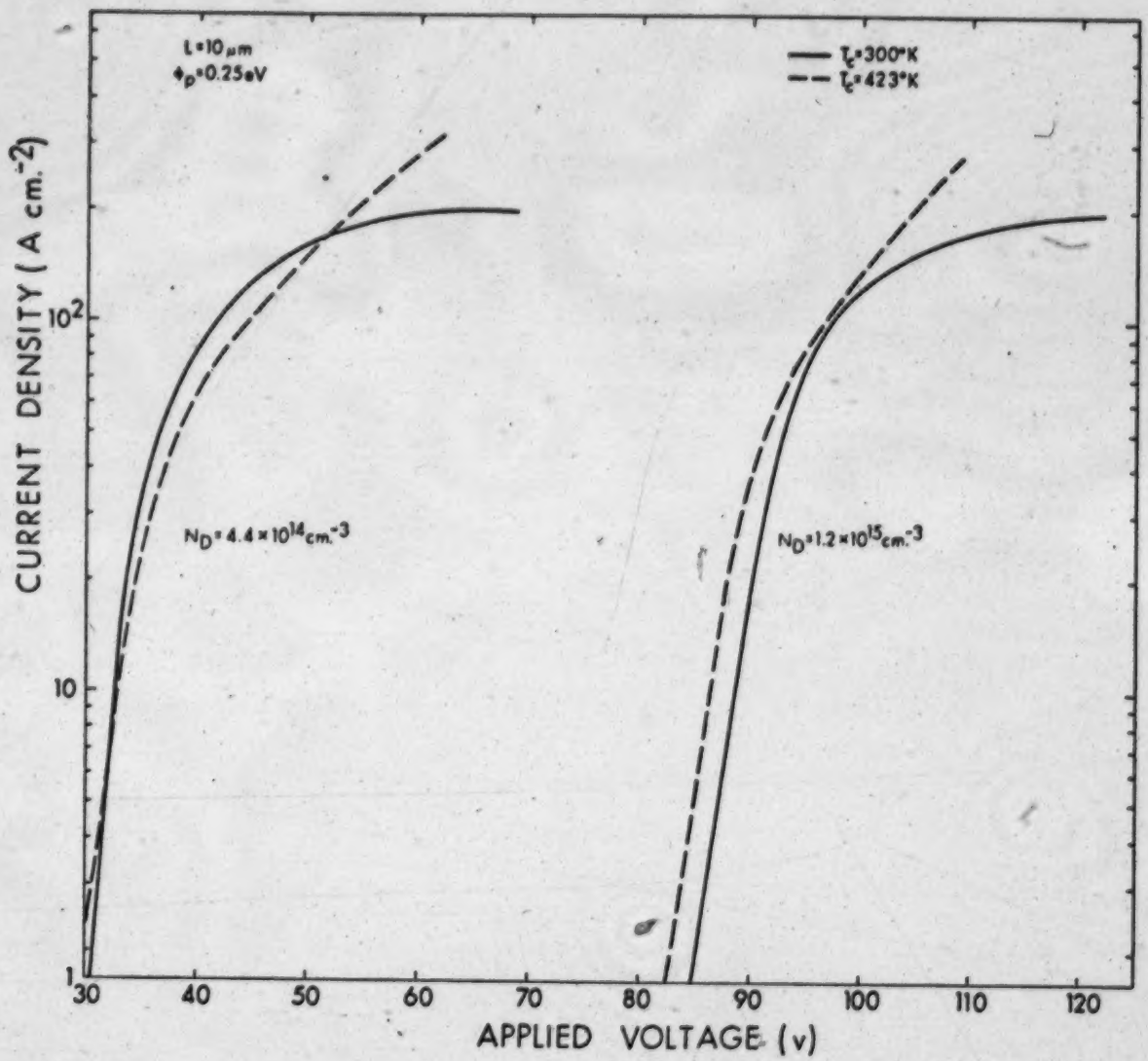

Fig. 6.3b: Current-Voltage Characteristics for Two Different Doping Concentrations and at Two Different Crystal Temperatures (L = 10 μm).

chapter.

6.2 Effects of Physical Parameters

To study the effects of the physical parameters, a variety of MSM structures differing in semiconductor width and doping concentration have been numerically investigated. The structures were chosen in such a way that operation at different microwave frequencies and under different biasing conditions could be examined.

The distribution of injected holes inside the semiconductor bulk, for two different doping concentrations, is shown in Fig. 6.1(a). For a given current, the density of holes is slightly reduced by increasing the doping concentration. This phenomenon is a direct consequence of the increase of the carrier drift velocity brought about by increasing the doping concentration.

Fig. 6.1(b) shows the electric field vs distance (measured from the injecting contact) for two doping concentrations at different current density levels. It is clearly shown that a significant increase of the slope results from increasing the doping concentration. The maximum electric field occurs at the collecting contact and can become so large that appreciable avalanche multiplication of free carriers takes place. For n-type Si with doping concentration below 10^{16} cm^{-3}, the avalanche breakdown field E_B is about 250 kV cm^{-1}. Consequently, for MSM structures made with fixed semiconductor width, the doping concentration is limited by that value at which the maximum

electric field at the collecting contact exceeds E_B. At a particular current density level, the electric field in the highly doped structure is everywhere larger than that in the lightly doped structure. Consequently, the terminal voltage necessary for obtaining the same current density increases as the doping concentration increases. The resulting J-V characteristics of the two structures are shown in Fig. 6.3b. While a bias voltage of about 35 volts is necessary to obtain 50 Acm^{-2} through the structure with low doping (4.4×10^{14} cm^{-3}), a bias voltage of about 85 volts is necessary to drive the same current density through the highly doped structure (1.2×10^{15} cm^{-3}).

Another important parameter that can significantly affect the terminal J-V characteristic of the MSM structure is the semiconductor width. For fixed doping, the applied bias increases with the increase of semiconductor width. This is a direct consequence of the electric field distribution inside the structure. Assuming a linear relation for the electric field vs distance, a quadratic relation between the electrostatic potential and the semiconductor width is obtained. Such a relation between V (electrostatic potential) and L (semiconductor width) can closely approximate that obtained for actual devices operating at normal current levels, provided that the effect of the space charge on the slope of the electric field is included. The resulting J-V characteristics for two structures, each having the same doping concentration but differing in semiconductor width, are shown by curves (B) and (C) of Fig. 6.4. A wide variation of applied voltage is also obtained by varying the width of the semiconductor slice.

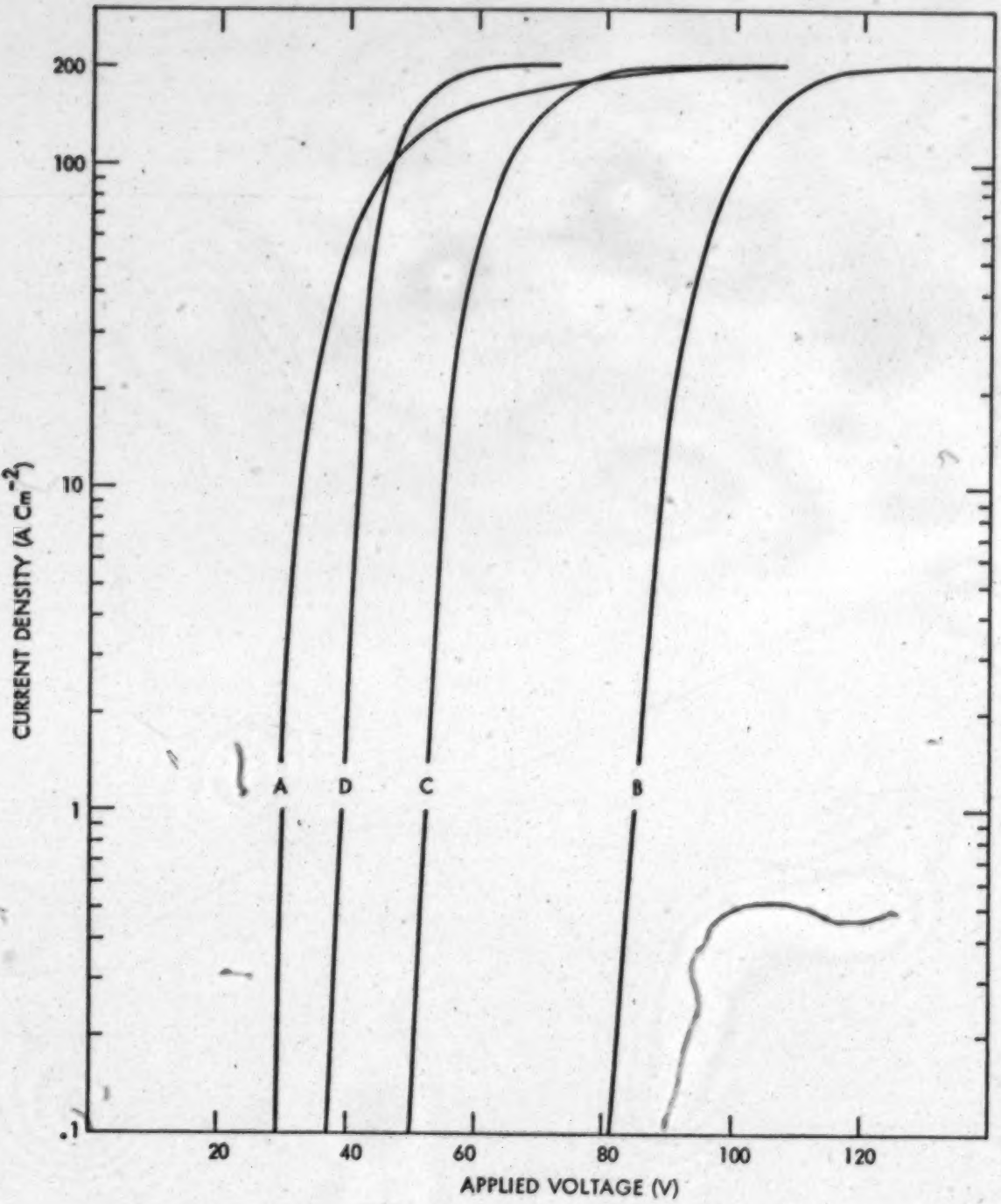

Fig. 6.4: Current-Voltage Characteristics for Structures A, B, C and D.

The combined effects of both doping concentration and semiconductor width are very important in the design considerations of the structure. The computed J-V characteristics for different structures A, B, C and D (as given in Table 6.1) are shown in Fig. 6.4. A comparison of curves A and B is informative since it illustrates the effect of changing the doping concentration while the width of the semiconductor is held constant. Likewise a comparison of curves B and C shows the effect of changing the semiconductor width while the doping concentration is kept constant. Curves B and D are the characteristics of two structures which have equal $N_D L$ products. A comparison between these two curves shows that the applied voltage is larger for the structure B which has a larger semiconductor width. According to Fig. 6.4, structures with lower doping and/or smaller semiconductor width result in lower dc bias voltages. It can also be seen from the same figure that the space charge effect is very small for structure D, having a highly doped semiconductor, while significant space charge is apparent in structure A, having a lightly doped semiconductor.

Since the slope of the J-V characteristics of Fig. 6.4 is very steep up to a current density of about 50 Acm^{-2} (which is nearly the optimum operating current density range of most devices) the dc bias voltage of the structures deviates only slightly from the punch-through voltage V_p. Consequently, V_p accurately approximates the actual operating voltage of the structure. Neglecting the space charge effect of injected holes, Poisson's equation can be integrated and the following expression for V_p

may be obtained

$$V_p = \frac{qN_D}{2\epsilon}(L - x_m)^2 - V_{bi}$$

where $x_m = \frac{2\epsilon V_{bi}}{qN_D}$, is the position of the potential energy maximum (measured from the injecting contact) and V_{bi} is the built-in potential. The calculated values of V_p as a function of N_D are shown in Fig. 6.5 for various values of L. The curves in this figure were obtained by assuming V_{bi} = 0.8 volts in the case of Si [34].

Good agreement between these curves and exactly calculated values is obtained if V_p is defined as the bias voltage corresponding to a current density of 0.1 Acm^{-2}. From Fig. 6.5, a wide range of applied voltage can be obtained by varying N_D and/or L as described above. In properly designed and operated structures, the maximum electric field must be well below the critical value, E_B, necessary for avalanche breakdown. The maximum applied voltage of the MSM structure is, therefore, limited by the breakdown voltage V_B and is represented by the constant electric field line E_B (E_B = 250 kV/cm is assumed). The curve E_B = 250 $kVcm^{-1}$ determines the upper limits of the structure's physical parameters. Dashed lines in Fig. 6.5 indicate the parameters for which the maximum electric field at punch through voltage reach 50 and 100 $kVcm^{-1}$.

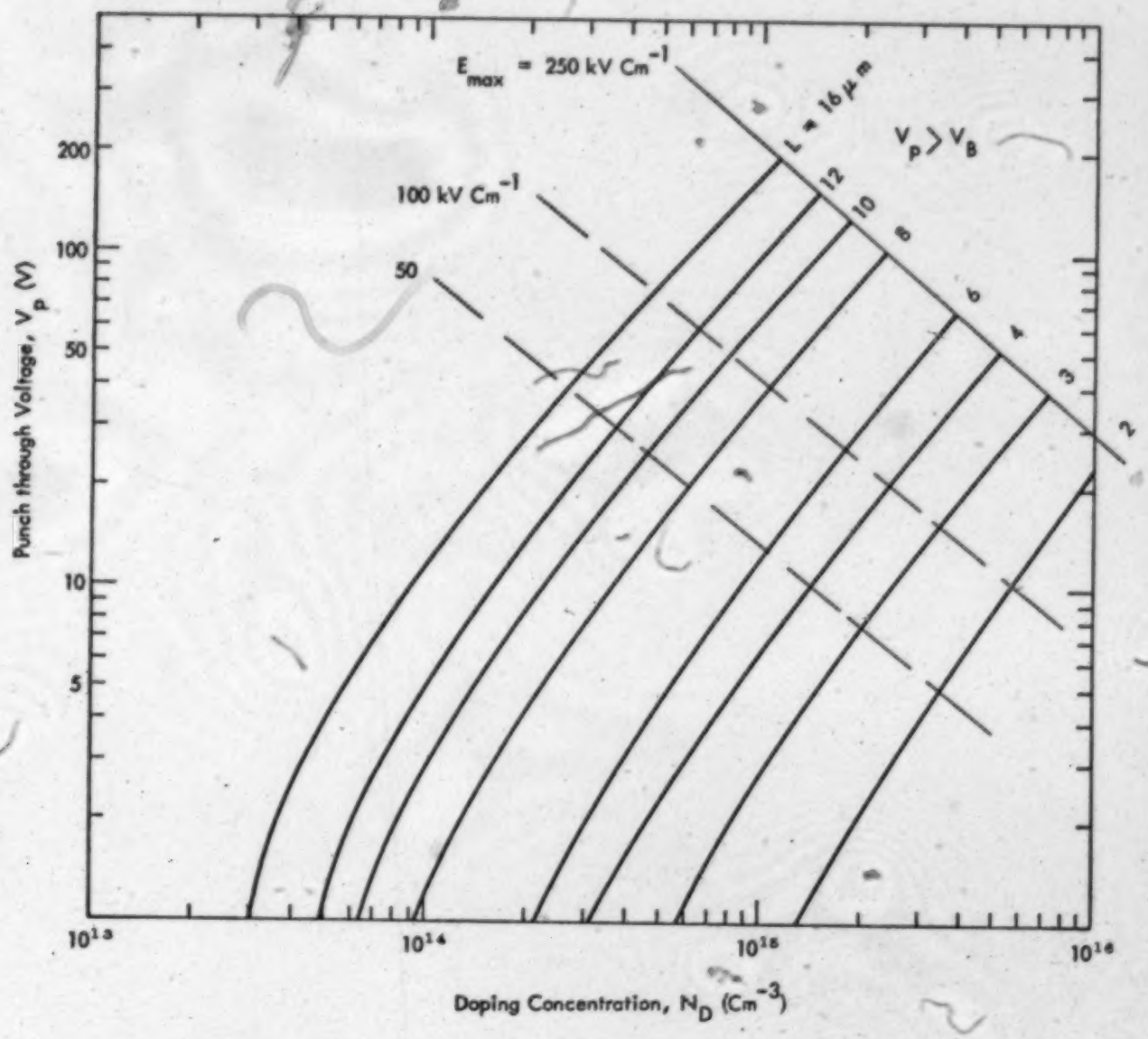

Fig. 6.5: Punch-Through Voltage V_p Versus Doping Concentration N_D, with Semiconductor Width L as a Parameter..

6.3 Temperature Effects on the DC Properties of the MSM Structures

The results described in the preceding sections were computed at room temperature by assuming isothermal conditions. It will be shown in the next chapter that, under dc conditions, all MSM structures dissipate power inside their semiconductor bulk. The dissipated power is then converted to thermal energy that heats the structure. MSM structures are usually operated at current densities of 10 - 100 A cm^{-2} and at bias voltages in the range 10 - 80 volts. Depending on the contact area of the structure, the dc power dissipation may vary in the range 0.5 - 8W. Assuming a collecting contact thermal resistance of about 20°C/W, the crystal temperature may thus be more than 100°C above room temperature at high current densities. Snapp and Weissglas [12] have shown experimentally that the crystal temperature significantly affects the microwave activity of the structure (the peak of the negative conductance shifts towards lower frequencies and reduces in magnitude with increasing T_c). Clearly, information on charge transport at T_c > 27°C is of great practical importance. To include high temperature effects on the static behavior of the structure, the mobility expression (Eq. 5.5) is used and a new set of constants in this expression is obtained from the consideration of the velocity-field dependence as previously discussed in Chapter 5. The boundary concentrations are also temperature dependent and the corresponding values at T = 150°C are considered. To simplify the numerical calculation, isothermal conditions are assumed.

The injection of minority carriers from MS contacts decreases with a decrease in temperature. At relatively low temperatures ($\sim$ 100°K) the dc bias voltage must be significantly increased (above V_B) in order to obtain the normal operating current density level. Snapp and Weissglas [12] experimentally showed that punched-through structures with MS injecting contacts operating at 100°K fail to exhibit any negative conductance. Furthermore, the dc bias voltage necessary to obtain 10 A cm^{-2} exceeds the avalanche breakdown voltage. Therefore, this study will be restricted to higher temperature ranges (i.e. above room temperature).

The concentration profile of the injected holes in the semiconductor region for two different crystal temperatures, T_c, computed at three current density levels, is shown in Fig. 6.6(a). It is shown in Chapter 4 that the boundary concentration at the MS contacts exponentially increases with increase of temperature. According to Fig. 6.6(a), at a given current the concentration of mobile holes in the bulk of the semiconductor (far from both contacts) increases only slightly with the increase of the lattice temperature. The high temperature bulk concentration is not only a direct consequence of the exponentially increased interface concentration with temperature but it also compensates for the reduced high-temperature carrier mobility. The electric field distribution inside the structure at two different operating temperatures is shown in Fig. 6.6(b). In most of the semiconductor

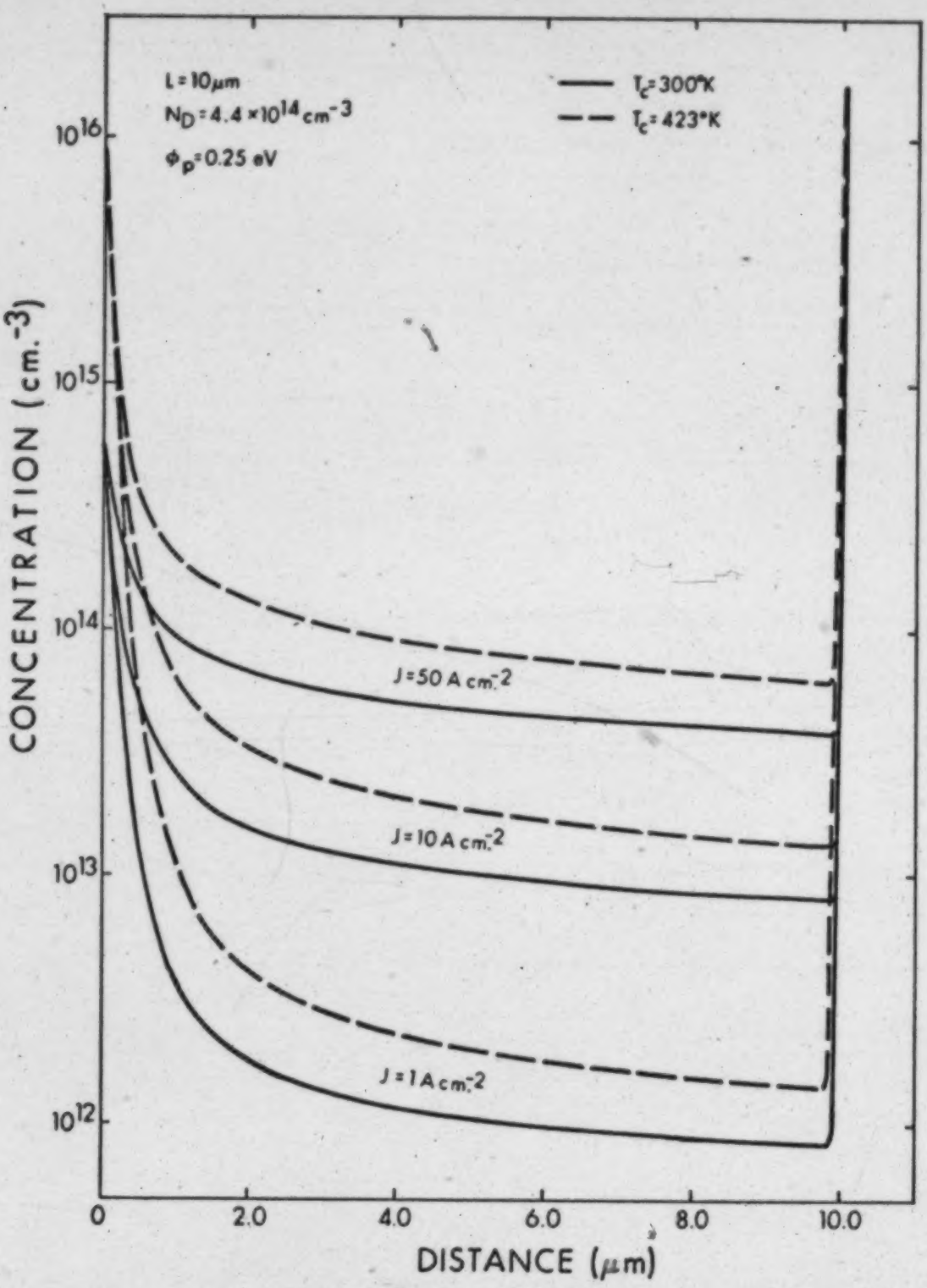

Fig. 6.6a: Concentration Profile of the Injected Mobile Holes in the Semiconductor Region at Two Different Crystal Temperatures.

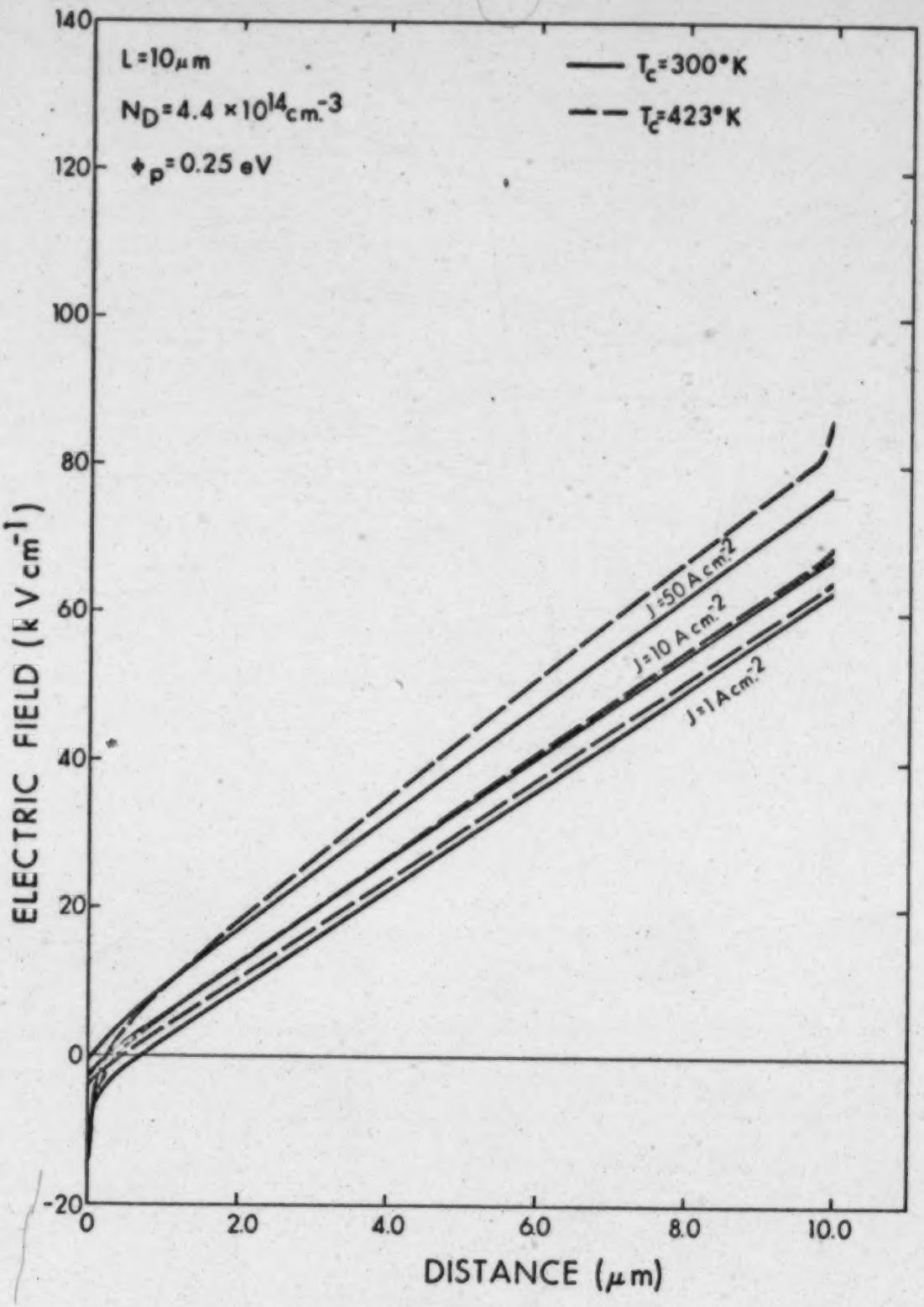

Fig. 6.6b: Corresponding Electric Field Distribution.

bulk, the electric field is linear, the slope being determined by the donor concentration for low-current levels (almost the same slope for both temperatures), while at high current levels, the slope of the electric field increases for higher temperature due to the pronounced space-charge effects of mobile holes. Near the MS contacts, a large number of mobile carriers exist and they significantly affect the slope of the electric field in the vicinity of both contacts. Fig. 6.6(b) also shows, for the particular MSM structure described in this section (device A), that at any current density level exceeding 1A cm^{-2}, the electric field is larger for higher temperatures everywhere in the semiconductor bulk. Hence the applied voltage necessary to obtain the same current density increases with increasing temperature.

The drift and diffusion current components (normalized to the total conduction current density) in the diffusion affected region, at two different temperatures (for structure A) is shown in Fig. 6.2(a). As the temperature increases, the drift component decreases due to the reduction of the low field mobility. Since the total conduction current is constant throughout the structure, the diffusion current component increases with increase of temperature to compensate for the reduction of the drift current component. Furthermore, with increasing temperature, the region of constant mobility extends to a region of higher electric field and the drift velocity saturates at increasingly higher electric field strengths. As a result, the diffusion affected region increases with

increasing the crystal temperature, as is clearly shown in Fig. 6.2(a).

The effect of increasing the semiconductor temperature on the distribution of the electrostatic potential is shown in Fig. 6.2(b). The potential energy maximum becomes wider, shifts farther from the injecting contact, and increases in magnitude with an increase of crystal temperature.

The J-V characteristics of structures A, B, E and F are shown in Fig. 6.3 for two temperatures (T_c = 300 and 423°K). The simplified J-V characteristic which is obtained by neglecting the space charge effect of injected holes on the electric field (for structures E and F, at T = 300°K) is also shown in Fig. 6.3(a). In comparison with the room temperature J-V characteristics, the high-temperature J-V characteristics at small currents are shifted towards lower voltages; the higher the doping concentration, the larger the shift. Since the space charge effect of injected holes is negligible at low current levels, the lower applied voltage for the higher temperature characteristic is due to the large negative amplitude of the electric field which occurs in the injection region (the barrier region of the forward biased contact). In the lightly doped structures (A and E), the room and higher temperature characteristics intersect twice. In these structures, the space charge effect of injected holes, at high temperatures and large current densities, is strong enough to cause the first intersection of the two characteristics. The saturation levelling of the room temperature characteristics is

responsible for the second intersection. In highly doped structures (B and F) on the other hand, the separation of the room and high temperature characteristics is relatively large, and the space charge effect of injected holes commences at relatively high current densities. This allows the room temperature characteristic to saturate before it can be intersected by the high temperature characteristics.

CHAPTER VII

SMALL-SIGNAL PROPERTIES OF MSM STRUCTURES

7.1 Small Signal Impedance

The small-signal impedance Z and admittance Y of MSM structures is defined as

$$Z = R + jX = \frac{1}{Y} = \frac{L}{G+jB} \equiv \frac{\tilde{V}_T}{A\tilde{J}_T} \qquad (7.1)$$

where $\tilde{V}_T$ and $\tilde{J}_T$ are the terminal ac voltage and the total ac current density; A is the contact area of the structure. According to the numerical calculations (based on the mathematical model described in Chapter V) the structure impedance, at microwave frequencies, can be represented by a parallel combination of a resistance and a capacitance, both dependent on frequency. Since the microwave behavior of the structure depends on a number of physical processes, the structure impedance is expected to be a complicated function of frequency. In a certain frequency range, the diode conductance can become negative while the capacitance varies around the geometrical capacitance C_o of the structure ($C_o \equiv \frac{\epsilon A}{L}$).

It is rather difficult to explain the microwave response of the MSM structure by a simple examination of the structure immittance defined by Eq. 7.1. For example, we cannot explain directly why the low frequency dynamic capacitance is less than C_o, while the

stationary capacitance $C_{st} = \frac{\partial Q}{\partial V_a}$ (Q is the total charge stored in the structure and V_a is the applied dc voltage) exceeds C_o because of the space charge.

In order to gain an understanding of the behavior of the structure, we investigate a "detailed" equivalent circuit obtained by splitting the structure admittance into two admittances corresponding to the conduction current $\tilde{J}_c$ and the displacement current $\tilde{J}_d$. At any cross-section the total current $\tilde{J}_T$ is constant and is given by

$$\tilde{J}_T = \tilde{J}_c(x) + \tilde{J}_d(x) \tag{7.2}$$

where $$\tilde{J}_d = j\omega\varepsilon\tilde{E} \tag{7.3}$$

Integrating Eq. 7.2 over the semiconductor width yields:

$$\tilde{J}_T = \frac{1}{L}\int_o^L \tilde{J}_c(x)dx + \frac{j\omega\varepsilon}{L}\tilde{V}_T \tag{7.4}$$

where $$\tilde{V}_T = \int_o^L \tilde{E}(x)dx \tag{7.5}$$

According to Eqs. (7.1) and (7.4), the small-signal admittance (per unit contact area) is

$$Y = \frac{\bar{J}_c}{\tilde{V}_T} + j\omega C_o = \bar{Y}_c + j\omega C_o \tag{7.6}$$

where $\bar{J}_c = \frac{1}{L}\int_o^L \tilde{J}_c(x)dx$ is the average ac conduction current

of the structure.

The equivalent circuit representation of the MSM structure is shown in Fig. 7.1. Such an equivalent circuit has been used by many authors to describe the small-signal behavior of various devices [51, 62-64]. The admittance is composed of a parallel combination of the geometrical capacitance of the structure and the "electronic admittance" $\tilde{Y}_c$ which depends on the charge transport properties of the structure. At relatively low frequencies, the electronic capacitance is negative ($C_c < 0$) showing the inductive effect of injected carriers, while at high frequencies (in the range of negative conductance) C_c may vary from negative to positive values.

Since the total conductance of the structure is due to the electronic processes occuring inside the device, the equivalent circuit described above cannot explain the mechanism of negative conductance. Therefore, to gain better understanding of the microwave performance of the MSM structure, the electronic processes inside the device must be investigated. A representative PtSi-nSi-PtSi structure ($L = 4.8$ μm and $N_D = 1.2 \times 10^{+15}$ cm^{-3}) has been numerically studied, and will be described in the next section.

7.2 Small-Signal Charge Transport Properties

It has been shown in Chapter III that the total ac current density may be written as

$$\tilde{J}_T = (qv_o(x)\tilde{p}(x) - qD_p \frac{d\tilde{p}(x)}{dx}) + qp_o(x)\tilde{v}(x) + j\omega\varepsilon\tilde{E}(x) \tag{7.7}$$

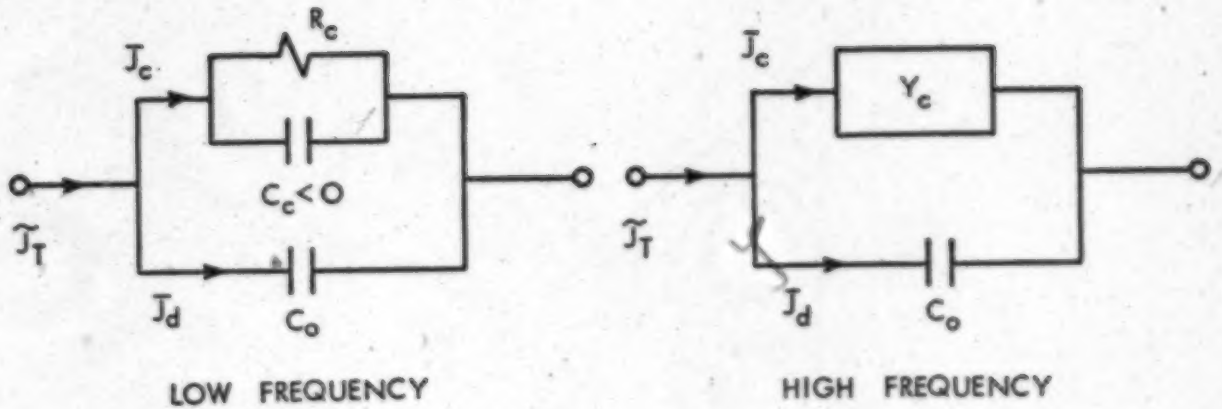

Fig. 7.1: Equivalent Small-Signal Circuit of Punch-Through MSM Structure for Relatively Low (Left) and High (Right) Frequency Ranges.

According to this equation, $\tilde{J}_T$ consists of the following components: the space-charge current $\tilde{J}_{sc}$ defined as

$$\tilde{J}_{sc}(x) = qv_o\tilde{p}(x) - qD_p\frac{d\tilde{p}}{dx} \tag{7.8}$$

the velocity modulation current

$$\tilde{J}_v = qp_o(x)\tilde{v}(x) \tag{7.9}$$

and the displacement current. The above current components are associated, respectively, with the time variation of the density of injected holes, their velocity and electric field.

We are particularly interested in the variation of the components of the conduction current $\tilde{J}_c$ defined as $\tilde{J}_c = \tilde{J}_{sc} + \tilde{J}_v$, which determines the charge transport inside the structure. The phasor representation of various components of $\tilde{J}_c$ (through the semiconductor region of the structure) is shown in Fig. 7.2. In this figure, the total ac current density lies on the positive real axis and various components are normalized with respect to $\tilde{J}_T$. Parameters were chosen as $J_o = 80\ Acm^{-2}$ and $f = 10$ GHz which corresponds to the maximum negative conductance obtained for this particular structure. The numbers in the figure represent the distance x in microns measured from the injecting contact.

The interesting feature of this diagram is the rapid decay of $\tilde{J}_v$ and the rapid increase of $\tilde{J}_{sc}$ on moving away from the injecting

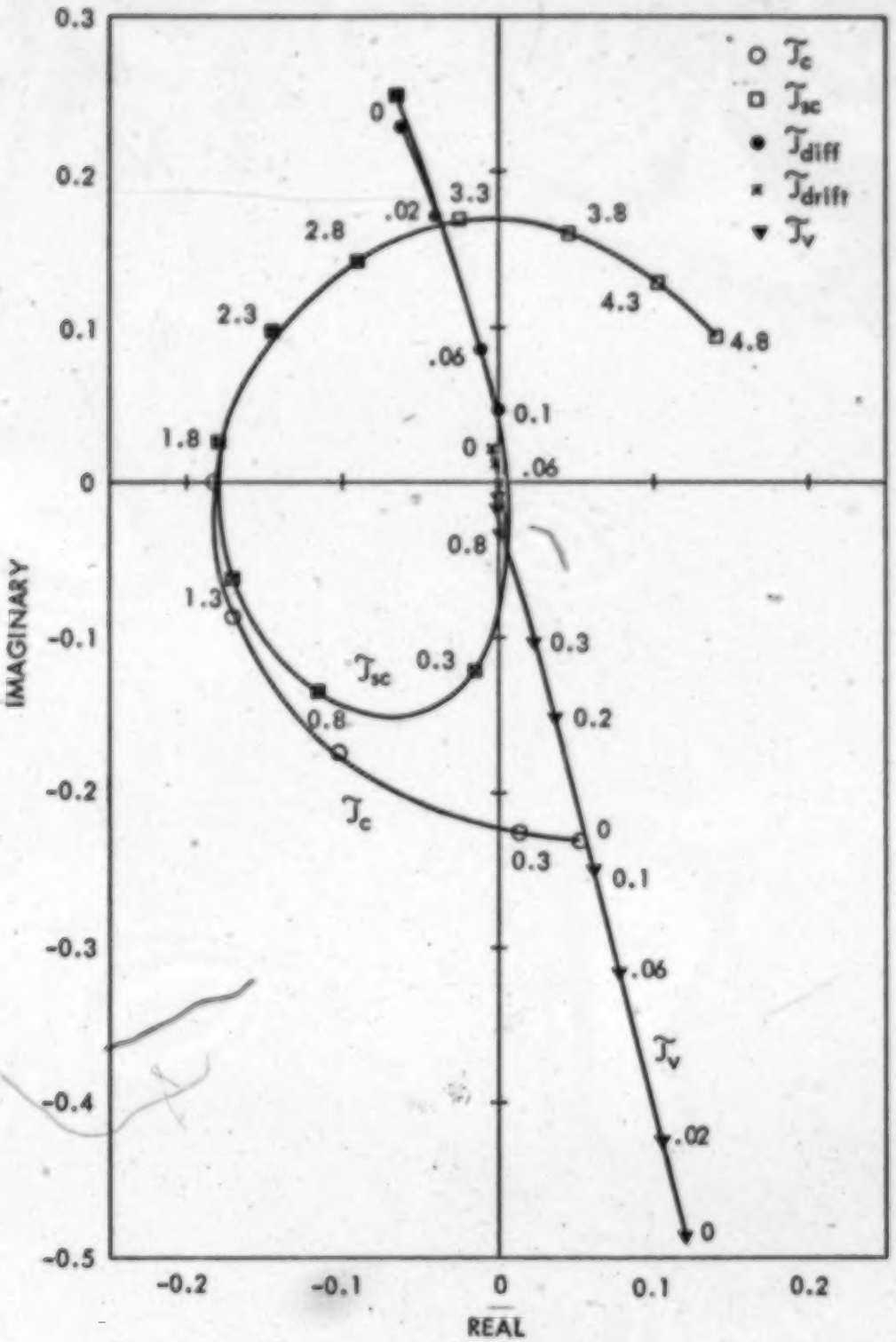

Fig. 7.2: Phasor Diagram of Various Components of the AC Conduction Current Density J_c (Normalized to the Total AC Current J_T). J_T Lies on the Positive Real Axis.

contact. At this contact, the dc concentration of injected holes, p_o, and the differential mobility, μ_d, of mobile holes ($\mu_d \equiv \frac{dv_o}{dE_o}$) are large. Both of these effects result in a large $\tilde{J}_v$. As the distance x increases, $p_o(x)$ and $\mu_d(x)$ decrease rapidly; thus $\tilde{J}_v$ falls off very quickly. The space-charge current, on the other hand, is large at the injecting contact because of ac carrier diffusion. In the vicinity of the contact, the ac concentration rises rapidly to an almost constant amplitude. Consequently, the diffusion current decreases while the drift component increases. On moving away from the injection region, the dc velocity of mobile holes increases rapidly resulting in a rapid increase of $\tilde{J}_{sc}$ which becomes nearly equal to $\tilde{J}_c$ upon entering the high field space ($x \geq 0.8$ μm). Since the amplitude of $\tilde{J}_c$ decays through the injection and low field regions, the phasors of $\tilde{J}_c$ for $x \leq 0.8$ μm take a reducing vortex format. In the high field region, the dc electric field is large and the conduction current wave travels through most of this region with nearly constant velocity. Since the conduction current amplitude scarcely decays within this region, the phasors of $\tilde{J}_c$ follow a circular path.

The propagation of space-charge and conduction current waves is shown in Figs. 7.3 and 7.4, respectively. Figure 7.3 shows the space-charge distribution at various time instants during one cycle of operation. The corresponding transport of the conduction current wave is shown in Fig. 7.4. These figures have been obtained from the real and imaginary components of $\tilde{p}$ and $\tilde{J}_c$, respectively. The phase of the total current, $\tilde{J}_T$, has been taken as reference.

According to Fig. 7.3, at t = 0 carriers injected in the

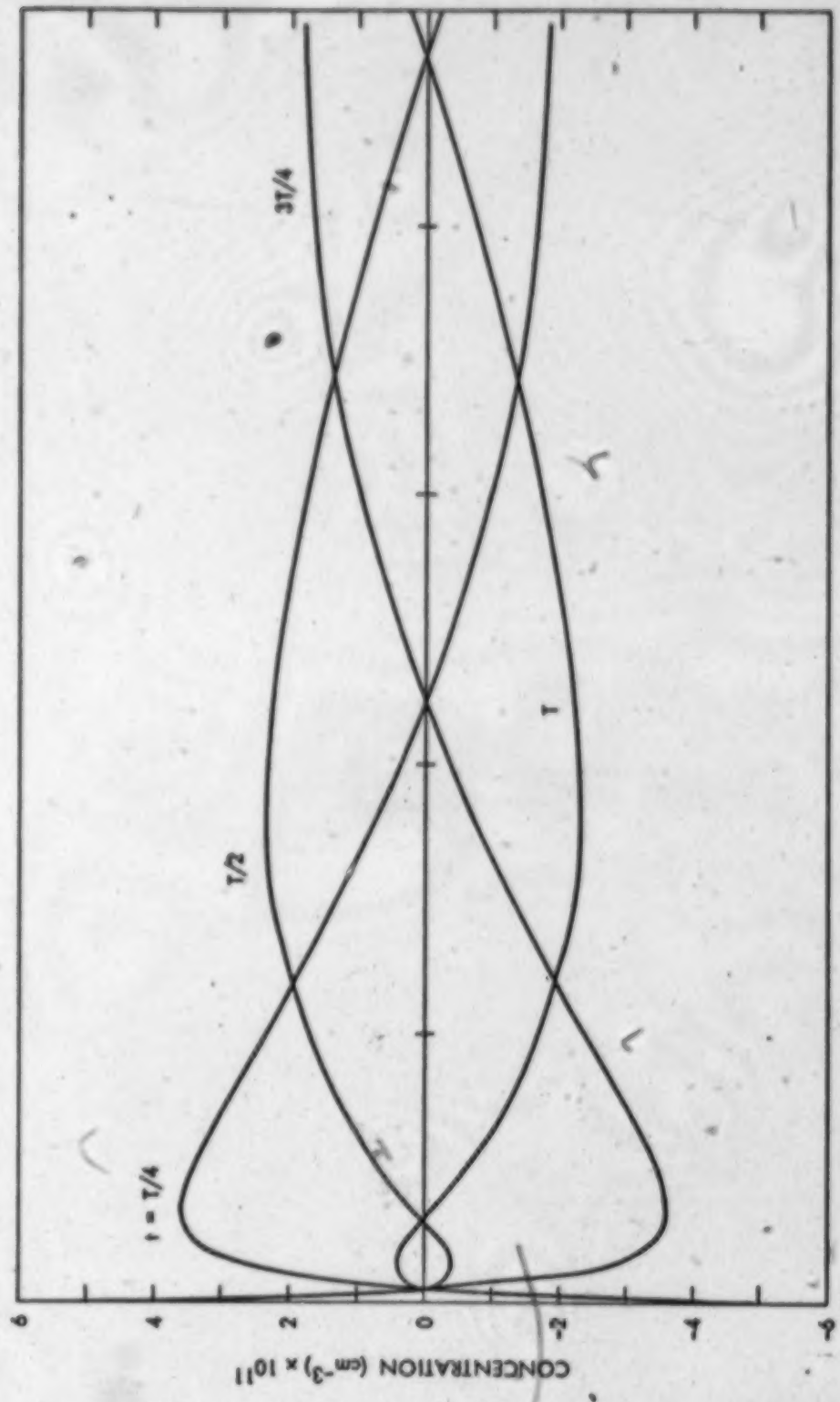

Fig. 7.3: Space Charge Distribution of Injected Holes at Various Time Instants During One Cycle of Operation

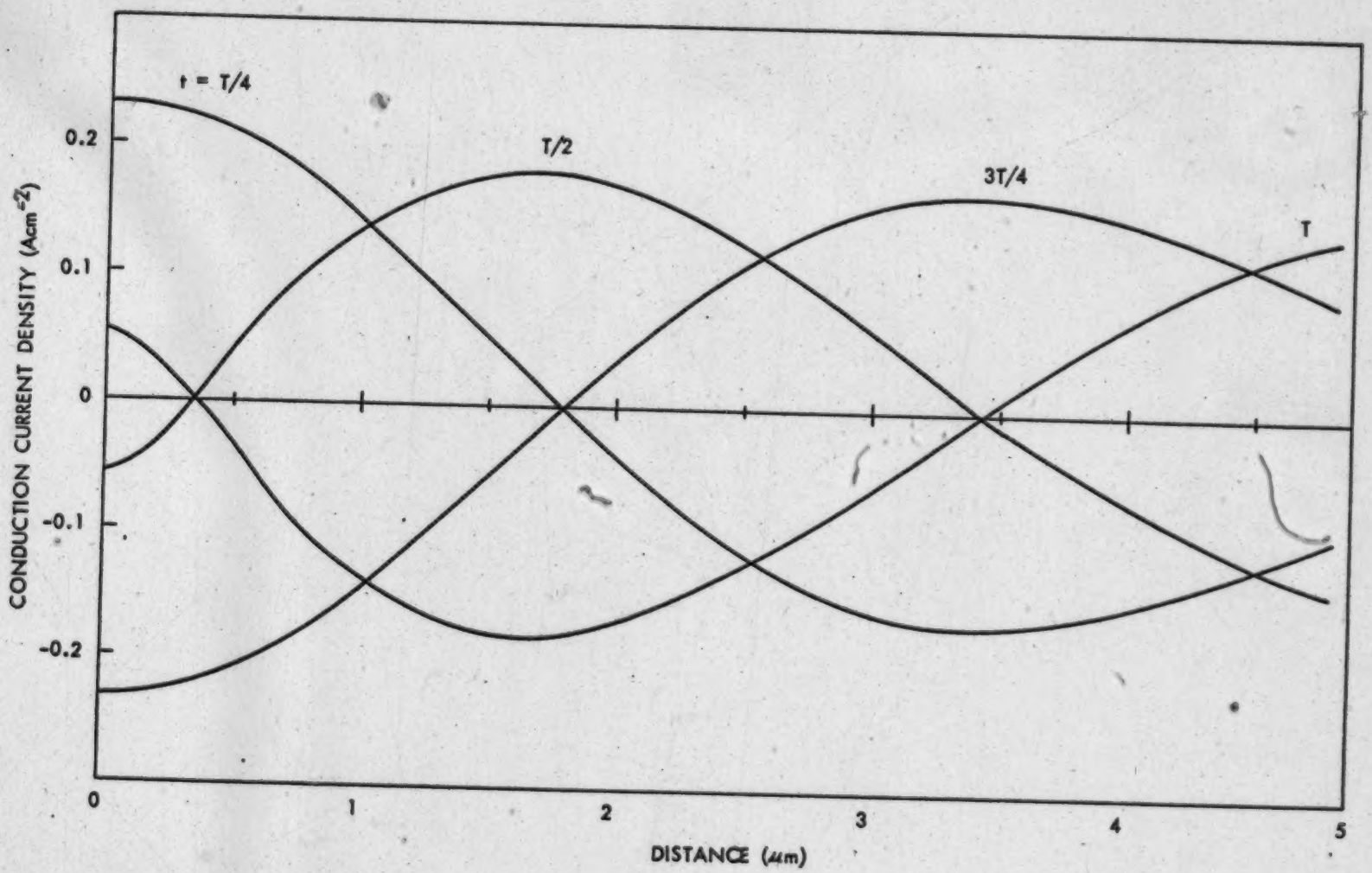

Fig. 7.4: Propagation of Conduction Current Wave at Various Time Instants During One Cycle of Operation.

previous cycle are disappearing at the collecting contact. As time progresses, the ac space charge bunch, formed close to the injecting contact, moves through the semiconductor bulk and reaches the edge of the diffusion affected region after one quarter of a cycle. In this region, the dc electric field is small, and hence the motion of injected ac holes is slow. At later time instants (e.g. at $t = T/2$) the bunch moves faster towards the collecting contact because of the rapid increase in the carrier drift velocity, (the shift of the bunch maximum is larger between T/2 and $\frac{3T}{4}$ than between T/4 and T/2). It is further apparent that as this bunch enters the high-field region, the space-charge forces combined with non-constant velocity result in bunch spread and thus reduction of the amplitude of the bunch.

According to Fig. 7.4, the maximum amplitude of the conduction current wave is delayed behind the total current maximum by about T/4. This delay is due to the fact that the structure acts in the first place as an insulator whose physical properties are slightly affected by injected mobile holes. It is further noticed that the amplitude of the $\tilde{J}_c$ wave decays in the injection and low-field regions while it is only slightly affected in the high-field region. The decay of the $\tilde{J}_c$ amplitude in the low-field region is a direct consequence of the rapid reduction of $\tilde{J}_v$ as previously discussed.

Bunch formation of injected holes close to the injecting contact can be described if an applied voltage step is considered. If such a step ΔV is superimposed on the dc bias voltage, the electric field is uniformly increased by ΔE throughout the semiconductor bulk (the injected charges cannot be rearranged

instantaneously). The immediate consequence of this variation in the electric field is to increase the velocity of injected holes by an amount

$$\Delta v = \frac{dv_o}{dE_o} \Delta E$$

where E_o and v_o are the steady-state dc values for the electric field and the carrier drift velocity. In the vicinity of the injecting contact, the additional velocity Δv of injected carriers is large and decreases as the distance from the injecting contact increases. As a result, injected carriers at the contact move faster than those inside the bulk and a bunch of charged carriers is generated in the vicinity of the contact where the density of injected holes is large. The bunch of injected holes moves towards the collecting contact with a velocity determined by the dc bias. On moving away from the injection region, the dc carrier velocity rises rapidly resulting in a spread and hence reduction of the bunch amplitude (as shown in Fig. 7.3). Dascalu [51] has shown that the spreading out of the bunch, as described above, is mainly due to the dependence of carrier velocity on position; a constant velocity throughout the semiconductor bulk would result in a constant bunch amplitude.

Referring to Fig. 7.3, it is apparent that the formation of the bunch of ac holes is associated with a steep concentration gradient which results in a diffusion current opposing the velocity modulation current. Since the net conduction current injected into the semiconductor bulk is reduced, the charge diffusion lowers the

incremental concentration in the whole semiconductor. This effect is clearly indicated in Fig. 7.5 which shows the distribution of the amplitude of the ac hole concentration inside the MSM structure. In this figure, the exactly calculated results (based on the "exact" model described in Chapter V) are represented by k = 1 curves. Curves k = 0 correspond to the boundary condition $\tilde{p} = 0$ (i.e. the injected holes are not affected by the ac current flow). The dashed curve shows the dc diffusion current (normalized with respect to the total dc current) and is drawn to identify the diffusion affected region. Negative amplitudes of the exactly calculated ac concentrations of injected holes correspond to 180° phase difference between $\tilde{p}$ and $\tilde{J}_c$ which is a direct consequence of the boundary conditions being used (as discussed in Chapter IV).

According to this figure, the ac concentration rises rapidly in the vicinity of the injecting contact, giving rise to a steep concentration gradient. Such behavior occurs in all cases (even for the case neglecting diffusion). For the exactly calculated dependences (curves k = 1), a point x_o at which no ac carrier modulation takes place is reached very close to the injecting contact ($\sim$ 0.06 μm in this particular structure). This point is almost unaffected by dc current density and signal frequency. Therefore, it can be assumed that x_o is an effective source plane at which no ac modulation of the amplitude of injected holes takes place. If a proper effective value for the dc concentration at x_o is found, the boundary concentration $\tilde{p}(o) = 0$ (closely resembles the equilibrium boundary concentration) can be used as a proper boundary condition.

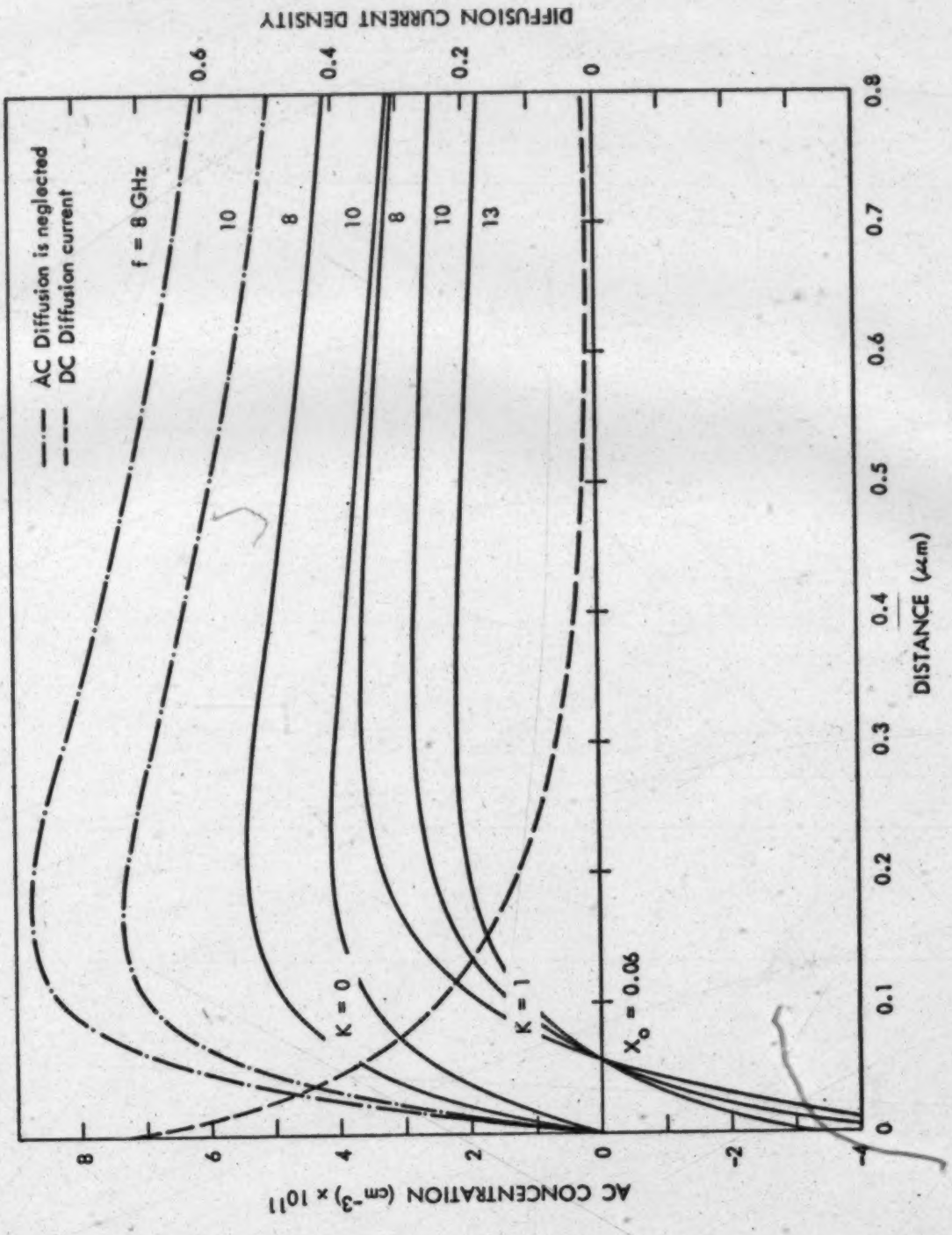

Fig. 7.5: Distribution of Space Charge Amplitude of AC Hole Concentration in the Vicinity of the Injecting Contact.

Using the current independent boundary concentration ($\tilde{p} = 0$) at the injecting contact, without adopting the effective dc concentration, significantly affects the maximum amplitude of the ac hole concentration, as clearly indicated in Fig. 7.5. It is further apparent that as the frequency increases, the amplitude of the ac bunch decreases. This is due to the reduction of the ac electric field at the injecting contact with increasing signal frequency.

The effect of neglecting ac diffusion on the amplitudes of the conduction current $\tilde{J}_c$ and the ac electric field $\tilde{E}$ can be seen in Fig. 7.6. This figure shows the phasor variation of $\tilde{J}_c$ and $\tilde{E}$ inside the semiconductor bulk. If ac carrier diffusion is neglected, the amplitude of the ac bunch of injected holes as well as that of the conduction current is too large, as compared with that obtained when ac diffusion is considered.

The transport properties described above were qualitatively discussed by Wright and Sultan [10]. It should be noted, however, that this study yields results which differ considerably from the present work in a quantitative sense. For instance, the maximum peak of the conduction current wave in Fig. 7.4 has a value approximately one half that obtained in the small-signal analysis due to Wright and Sultan [10].

The most significant difference between the study quoted above and the present analysis is the fact that the carrier diffusion in the vicinity of the injecting contact has previously been ignored. This is obviously a very important factor from a quantitative point of view.

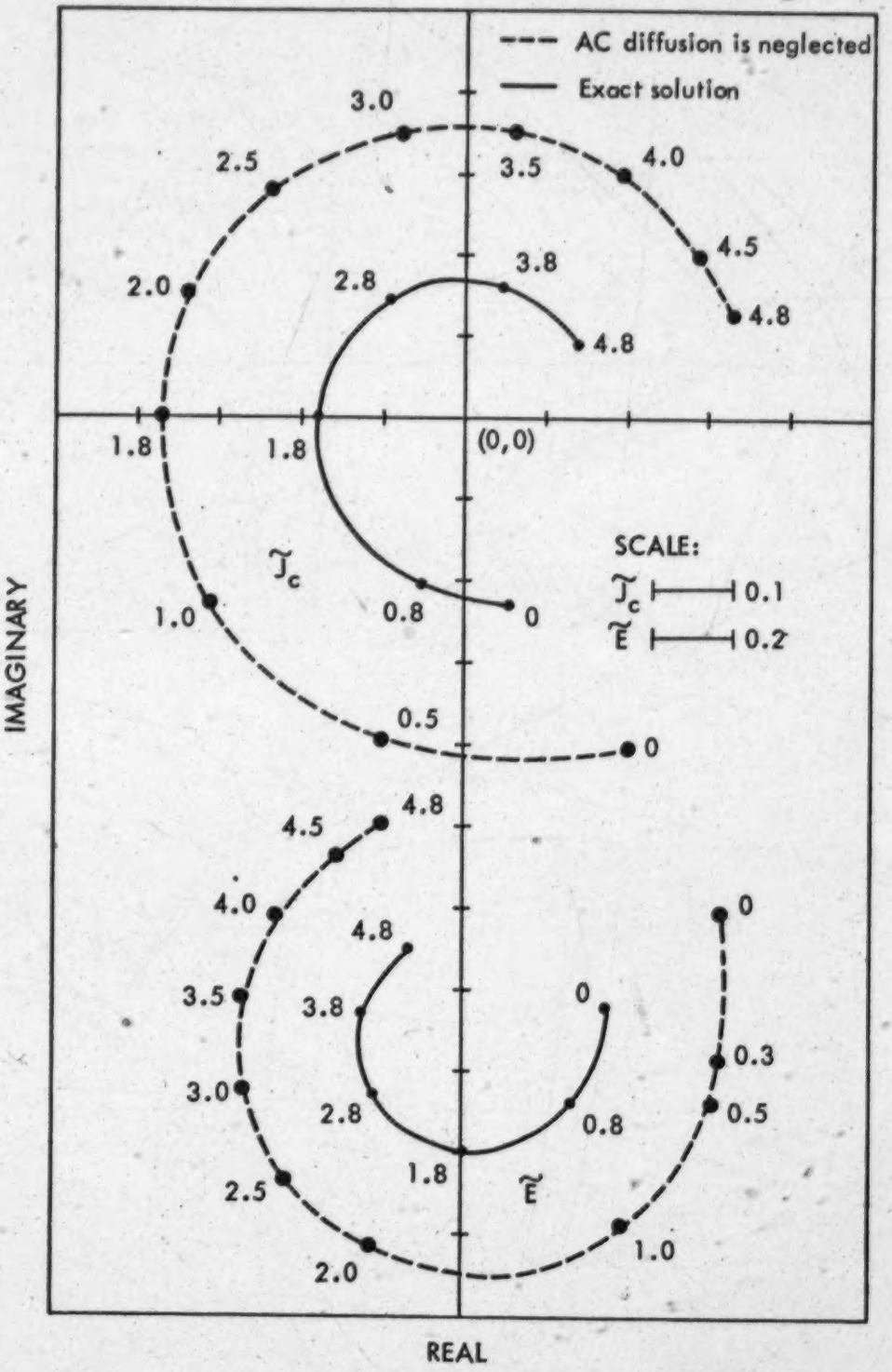

Fig. 7.6: Phasor Diagram of AC Electric Field $\tilde{E}$ and AC Conduction Current $\tilde{J}_c$ (Normalized to the Total AC Current Density $\tilde{J}_T$). $\tilde{J}_T$ Lies on the Positive Real Axis.

7.3 Power Dissipation Inside the MSM Structure

Positive resistance corresponds to power dissipation while negative resistance reflects the ability of solid matter to generate electric energy. Since the slope of the J-V characteristic of the MSM structure is always positive (Fig. 6.3), the structure dissipates dc electric energy. The thermal energy, into which the dissipated energy is converted, then heats the structure. Under ac conditions, the finite transit time of injected carriers through the semiconductor can result in a phase delay between the conduction current and the local ac electric field ranging from $\frac{\pi}{2}$ - $\frac{3\pi}{2}$. At frequencies at which such delay occurs, the structure can present negative conductance (resistance) to the external circuitry. If included in proper rf circuitry, the structure can convert part of the supplied dc energy into rf energy. In this section, the dc and small-signal ac power dissipation inside an MSM structure will be described.

(a) DC Power Dissipation

The dc power dissipation inside the semiconductor bulk of an MSM structure (per unit contact area) is given by

$$P_o = \int_o^L J_o E_o(x) dx \qquad (7.12)$$

where J_o is the dc conduction current density (consists of drift and diffusion components), E_o is the dc electric field, and o and L are the position coordinates of the injecting and collecting MS

contacts, respectively. The conduction current J_o is given by

$$J_o = q\mu E_o(x)p_o(x) - qD_p \frac{dp_o}{dx} \qquad (7.13)$$

The local power dissipation due to the drift component of the conduction current (per unit contact area) is

$$P_{drift} = q\mu(E)p_o(x)E_o^2(x)dx \qquad (7.14)$$

Since all the physical quantities in Eq. 7.14 are positive, P_{drift} is positive. The local power dissipation due to the diffusion current component is

$$P_{diff} = \int (-qD_p \frac{dp}{dx})E_o(x)dx$$

In the injection region ($x = 0$ to $x = x_m$, where x_m is the potential maximum position), the electric field takes non-positive values and the injected holes are moving against the electric field mainly by diffusion. Since $(\frac{dp}{dx})$ is negative, P_{diff} is negative in the injection region (where $E_o \leq 0$) and dc power generation instead of dissipation occurs within this region. This phenomenoncould be explained as follows: when a carrier moves in the direction that the electric field tends to push it, the field does work on the carrier and consequently the field loses energy (which is converted into thermal energy of the particle). When a carrier moves against the electric field, the opposite occurs, and the carrier pumps energy to the field

(i.e., part of the particle thermal energy is converted to field energy). The last situation occurs in the injection region and the carriers give up energy. Apart from the injection region (i.e., $x > x_m$), the electric field takes positive values and the carriers diffuse in the direction of the electric field; thus the local P_{diff} becomes positive and the diffusion current contributes to power dissipation.

Since the injection region is only a small fraction of the total semiconductor width (usually less than 10% for all devices), the net power dissipation inside the MSM structure is positive and the structure, therefore, dissipates dc power. The dissipated power inside the low and high field regions ($x > x_m$) is converted to thermal energy of particles which then heats the semiconductor bulk (via scattering mechanisms). In the injection region, on the other hand, the mobile carriers lose energy to the electric field, and their temperature reduces slightly below the crystal temperature as discussed in Chapter III.

The spatial variation of the dc power dissipation inside the MSM structure is shown in Fig. 7.7. In the injection region very little power is generated while large power dissipation occurs in the major part of the structure.

(b) <u>High Frequency Power Dissipation Inside the MSM Structure</u>

High frequency negative resistance reflects the ability of the active device to convert part of the dc power into high frequency power. The conversion mechanism can be explained by investigating power dissipation inside the structure, namely the dissipation corresponding to each component of the total ac current.

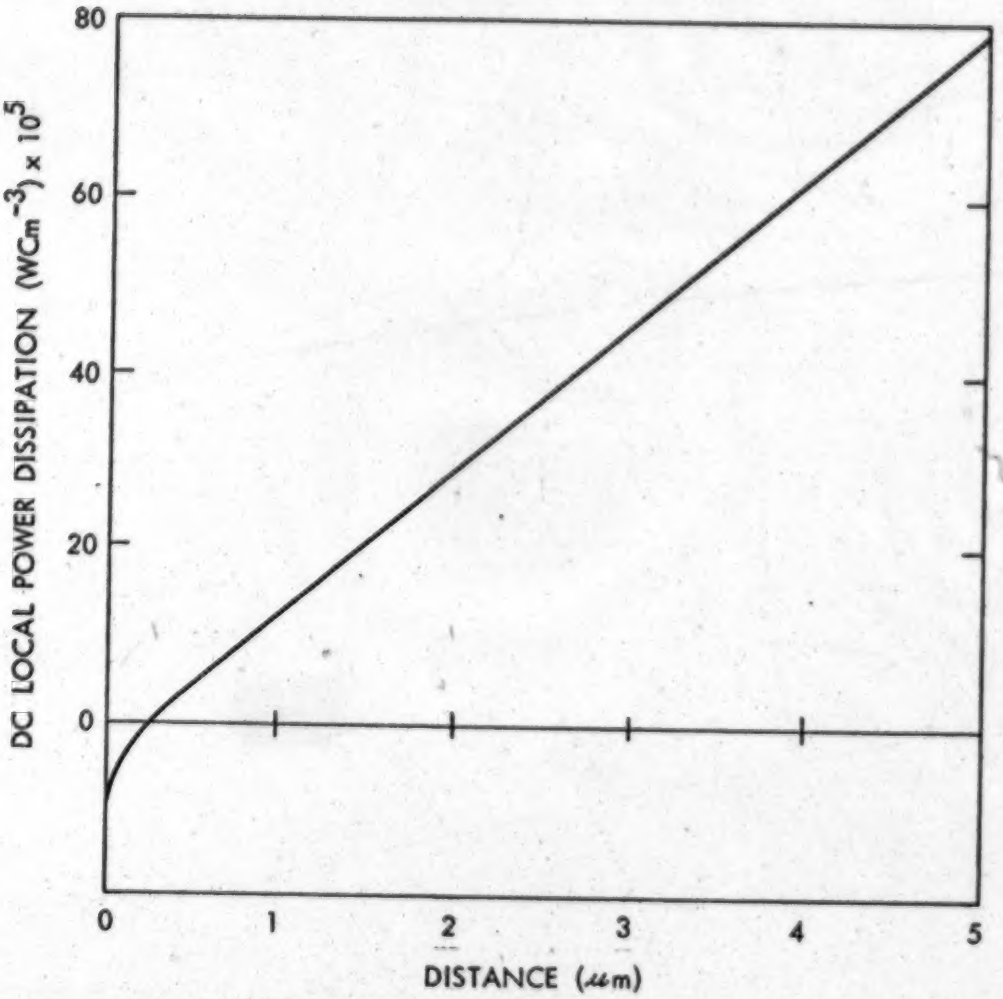

Fig. 7.7: Spatial Variation of DC Power Dissipation.

The net ac power dissipation inside the MSM structure (per unit contact area) is given by [51],

$$P_{net} = \frac{1}{2}R_e\left(\int_0^L \tilde{J}_T^*\tilde{E}(x)dx\right) = \frac{1}{2}\left(\tilde{J}_T^*\tilde{V}_T\right) \qquad (7.15)$$

where $\tilde{J}_T$ and $\tilde{V}_T$ are the external ac total current density and voltage respectively. Substituting for $\tilde{J}_T$ from Eq. 7.1, the net ac power dissipation can be written as

$$P_{net} = \frac{1}{2}R_e \int_0^L (\tilde{J}_{sc}^* + \tilde{J}_v^* + \tilde{J}_d^*)\tilde{E}(x)dx \qquad (7.16)$$

which consists of three components corresponding to $\tilde{J}_{sc}$, $\tilde{J}_v$ and $\tilde{J}_d$ respectively.

The active ac power associated with the displacement current $\tilde{J}_d$ is

$$P_d = \frac{1}{2}R_e \int_0^L \tilde{J}_d^*(x)\tilde{E}(x)dx = \frac{1}{2}R_e \int_0^L -j\omega\varepsilon|E(x)|^2\,dx \equiv 0 \qquad (7.17)$$

Therefore, the displacement current neither dissipates nor generates active power inside the structure. This is expected since $\tilde{J}_d$ always leads the local ac field by $\frac{\pi}{2}$ angle throughout the whole semiconductor bulk.

The local active power associated with $\tilde{J}_v$ is

$$P_v = \frac{1}{2}R_e\left(\tilde{J}_v^*(x)\tilde{E}(x)\right) = \frac{1}{2}R_e\left(qp_o(x)\mu_d(x)|\tilde{E}(x)|^2\right) \qquad (7.18)$$

According to Eq. (7.18), P_v can become negative (corresponds to power generation) if μ_d is negative. The differential mobility μ_d, however, is a property of the semiconductor material. For some semiconductor materials (e.g., GaAs), the differential mobility of electrons is negative in a certain range of the electric field. However, for silicon (which is investigated here), μ_d for holes or electrons is always positive at all values for the electric field. Consequently, P_v for silicon devices is positive and power dissipation always occurs due to the velocity modulation component.

Therefore, power generation which takes place in the MSM structure is due to the space charge current component. The power dissipation associated with $\tilde{J}_{sc}$ (per unit contact area) is

$$P_{sc} = \frac{1}{2}R_e(\tilde{J}^*_{sc}(x)\tilde{E}(x)) \qquad (7.19)$$

It has been shown in the previous section that $\tilde{J}_{sc}$ becomes nearly equal to $\tilde{J}_c$ in most of the semiconductor bulk (see Fig. 7.2); in addition the phase angle, θ, between the space charge current and the local ac electric field can exceed $\frac{\pi}{2}$ in some regions of the semiconductor (see Fig. 7.6). Generally, if the signal frequency ω is sufficiently high (in comparison with the reciprocal of the carrier transit time) the phase angle θ can lie in the range $\frac{\pi}{2} \leq \theta \leq \frac{3\pi}{2}$ in most of the semiconductor bulk. Consequently, the net power dissipation due to $\tilde{J}_{sc}$ can be negative (i.e. power generation.

Figure 7.8 shows the spatial variation of the local power

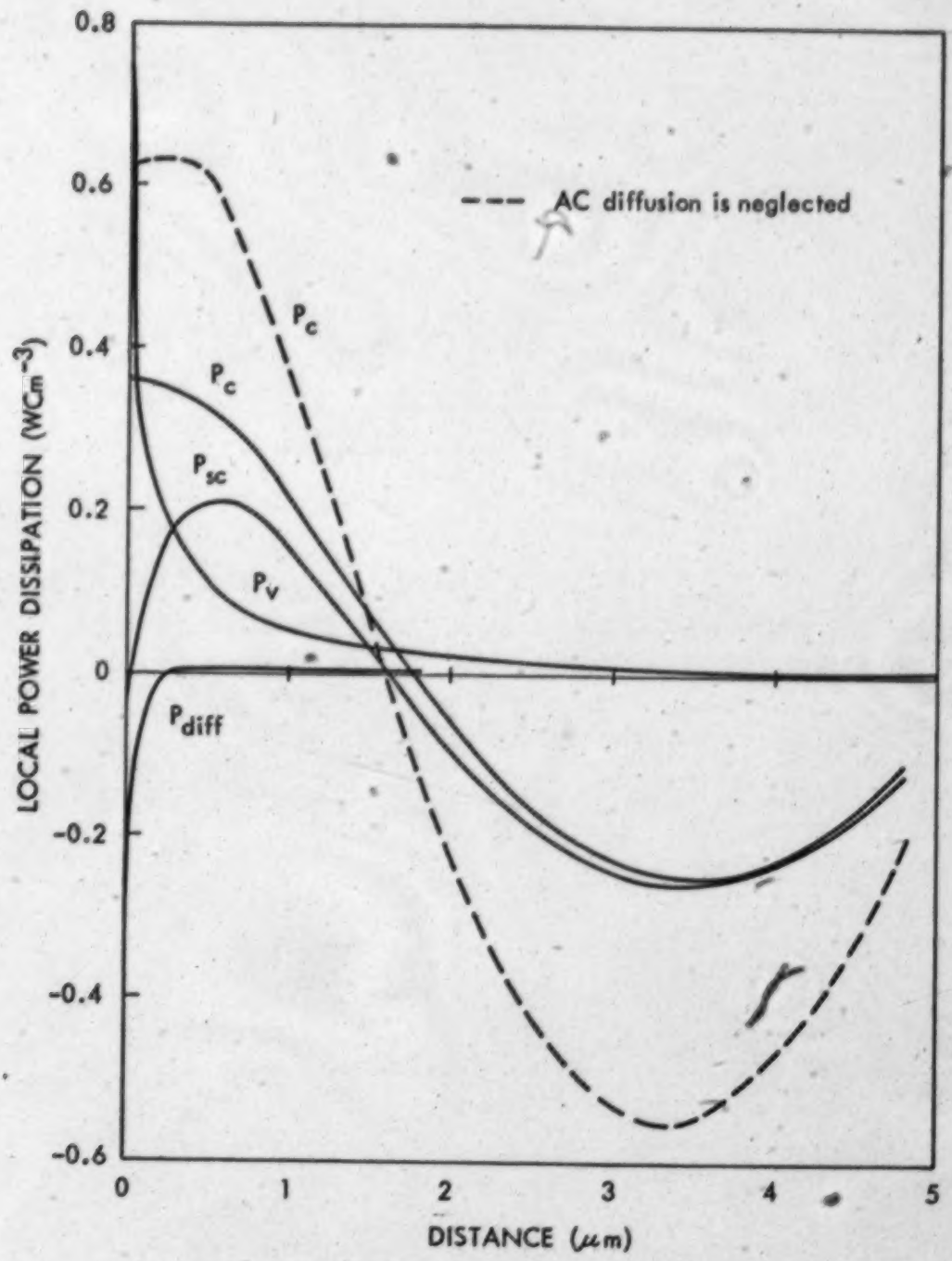

Fig. 7.8: Spatial Variation of AC Power Dissipation Corresponding to Various Components of the AC Conduction Current.

dissipation P_v and P_{sc} at the frequency which corresponds to optimum microwave activity of the structure. The power dissipation P_v is large near the contact and decays rapidly when moving towards the high field region. The reduction of P_v is a direct consequence of the rapid decay of $\tilde{J}_v$ (as shown in Fig. 7.2). Near the contact, $\tilde{J}_{sc}$ contributes to power dissipation. The contribution of the diffusion and drift current components to P_{sc} is also shown in the figure. The diffusion current contributes to power generation because of the diffusion of the ac holes against the local ac electric field; this power generation, however, is insignificant (as in the dc case). The drift current contributes to power dissipation in the region $x < 1.8$ μm, because it lags behind the ac electric field by an angle less than $\frac{\pi}{2}$. For this particular structure, the phase angle θ becomes more than $\frac{\pi}{2}$ at a distance x exceeding 1.8 μm and, therefore, local power generation instead of power dissipation takes place. The local power dissipation P_c due to the total conduction current ($P_c = P_v + P_{sc}$) is also shown in Fig. 7.8. It can be clearly seen that the net ac power loss (the total area under the P_c curve) is negative and the semiconductor presents negative conductance in the external circuitry.

CHAPTER VIII

SMALL-SIGNAL ADMITTANCE OF MSM STRUCTURES

In this chapter, the computed small-signal admittance of various PtSi-nSi-PtSi structures is graphically presented and discussed. The equivalent circuit described in Chapter VII has been used to identify the electronic admittance of the structure. Physical parameters (e.g. doping concentration and semiconductor width)of the investigated structures are given in Table 8.1 and the results are displayed per unit cross-sectional area of the contacts. In obtaining these results, the total ac current density is assumed constant independent of the signal frequency ω. The small-signal admittance of a typical structure is presented in section 8.1. In the following sections the temperature-dependence of the small-signal admittance and the effects of the physical parameters of the structure are described.

8.1 Small-Signal Admittance of an MSM Structure

A typical admittance chart of the structure C ($L = 7.9\ \mu m$ and $N_D = 1.2 \times 10^{15}\ cm^{-3}$) is shown in Fig. 8.1, for different dc current densities. Dashed curves in the figure are the constant frequency contours. According to this figure, negative conductance is displayed over a wide frequency range ($f = 4.5$ GHz - 8.5 GHz). At low current-densities, the maximum negative conductance is small and increases slightly with an increase of current density.

TABLE 8.1

SUMMARY OF STRUCTURE PARAMETERS USED FOR THE SMALL-SIGNAL STUDY

Structure	Semiconductor width, L(μm)	Doping Concentration $N_D(cm^{-3})$
A	10	4.4×10^{14}
B	10	1.2×10^{15}
C	7.9	1.2×10^{15}
D	4.8	2.5×10^{15}

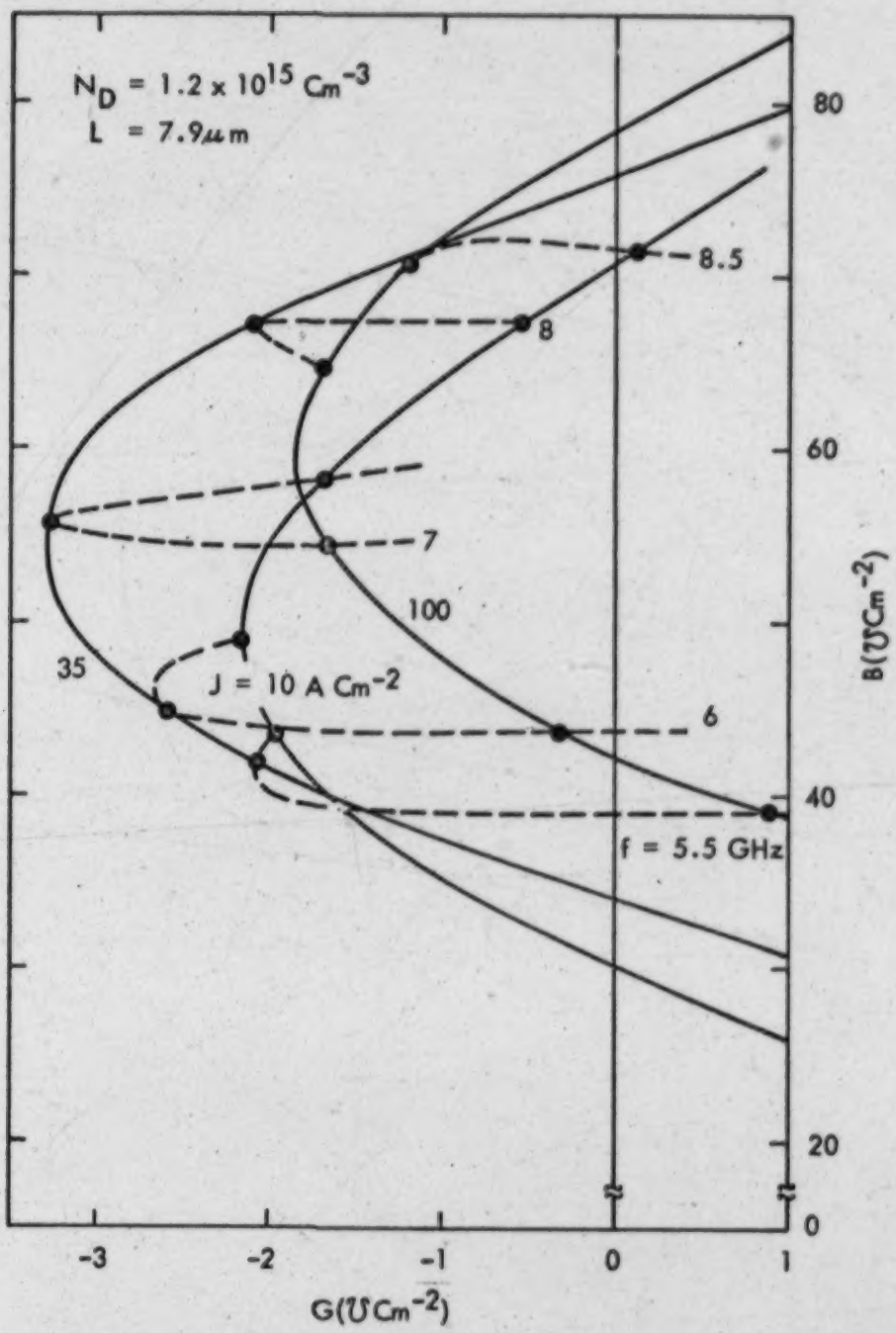

Fig. 8.1: Admittance Chart of Structure C, for Different Current Densities.

Optimum negative conductance for this particular structure occurs at a current density somewhat greater than 35 A cm^{-2}. As the current density increases further, the negative conductance decreases. It is also apparent in the figure that the structure susceptance is frequency dependent. For a given frequency the structure susceptance decreases with an increase of dc current density.

At low currents, insignificant carrier modulation takes place because of the small dc concentration of injected holes in the entire semiconductor. Conduction current is thus a small fraction of total current and the charge transport processes will have only a small effect on the overall behavior of the structure. Consequently, the negative conductance is small. As the dc current density increases, more carriers are modulated by the ac signal resulting in an increase in the ac conduction current as well as in the negative conductance. If the current density is sufficiently large, the density of dc injected holes in the semiconductor bulk becomes high enough to give rise to a large velocity modulation current. Therefore, the power loss associated with $\tilde{J}_v$ increases and hence the negative conductance reduces. In addition, a large dc density of injected holes reduces the phase-delay between the conduction current wave and the ac electric field in the entire semiconductor bulk. This effect results in an additional reduction of the negative conductance at high current levels.

The frequency dependence of the structure conductance G and susceptance B is shown in Fig. 8.2 for different current densities.

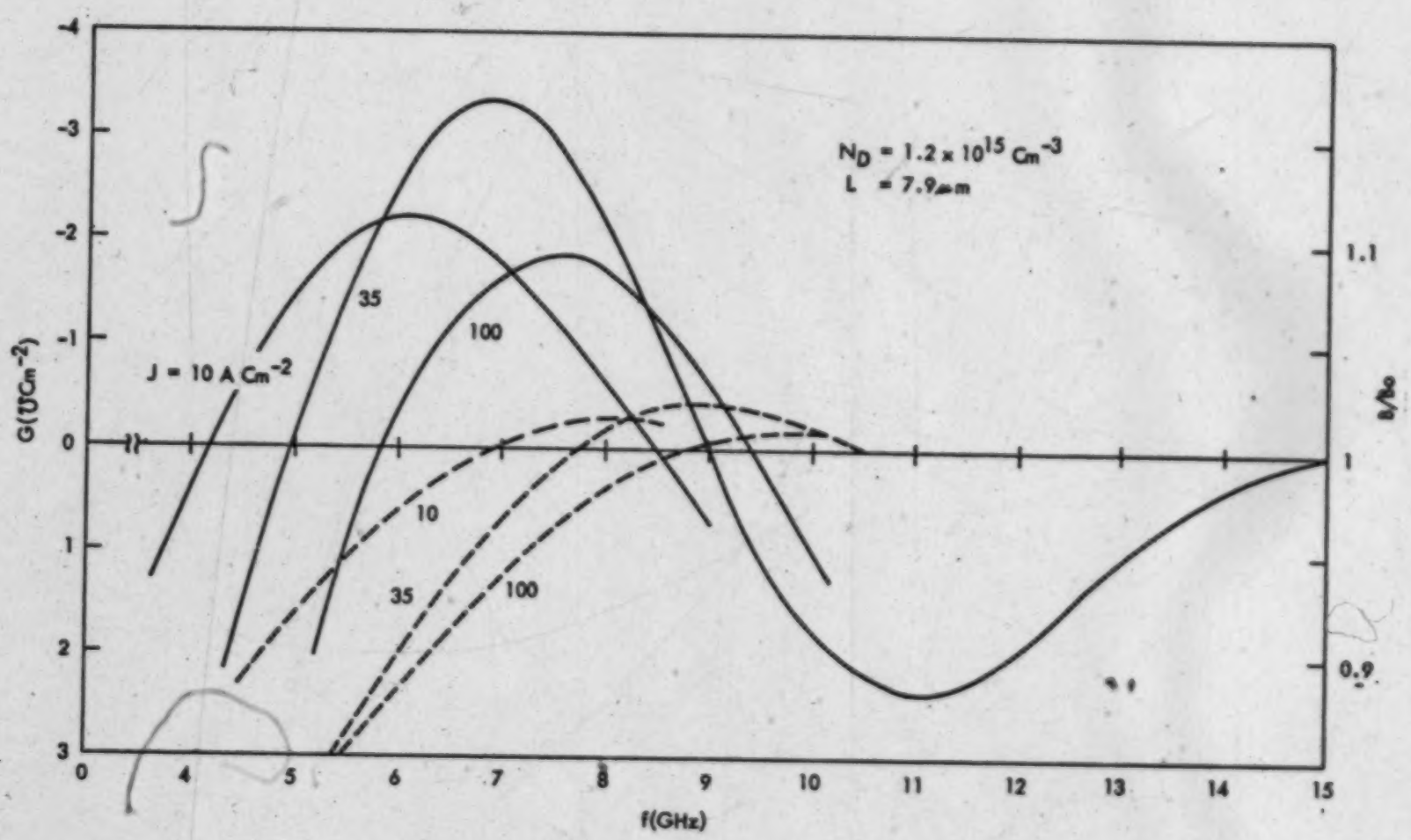

Fig. 8.2: Frequency Dependence of the Small-Signal Conductance, G and Normalized Susceptance of Structure C, for Different Current Densities.

For a given current density, the active frequency interval (defined as the interval in which the device exhibits a negative conductance) extends over about an octave; and it slightly decreases with an increase of the current density. As the current density increases, the peak of the negative conductance shifts to higher frequencies. The electronic tuning coefficient defined by

$$\alpha_e = \frac{1}{f} \frac{\Delta f}{\Delta J} \tag{8.1}$$

is of the order of 10^{-3}/A cm^{-2}. In addition to the optimum negative conductance near the optimum frequency of 6.75 GHz, the structure exhibits a second conductance minimum at about 15 GHz. At such a high frequency, the power generation due to the space charge current is compensated by the power loss due to the velocity modulation component and hence no negative conductance is displayed by this structure. The second minimum in G is seen to occur at a frequency about 2.22 times the fundamental one. From transit time considerations, the second minimum should occur at 7/3 of the fundamental frequency; hence an additional but insignificant phase delay is also present.

The susceptance B (dashed curves in Fig. 8.2) has been normalized to the geometrical susceptance B_0 of the structure ($B_0 = \omega C_0$). For a given current density, B is less than B_0 in most of the frequency interval of negative conductance. The structure susceptance does, however, exceed B_0 at frequencies slightly higher than the optimum frequency. This transition of the electronic

susceptance from inductive to capacitive, which was experimentally reported, cannot be predicted by simple theories [e.g., 5,10]. In these theories, the electronic susceptance is always inductive for transit angles in the range $\pi - 2\pi$. The capacitive nature of the electronic susceptance is due to an additional phase delay mechanism associated with the charge-transport in the injection and low-field regions of the structure.

According to Fig. 8.3 the predicted negative conductance of the MSM structure is relatively small. Therefore, it can be easily masked by the positive conductance of the MS contacts and the inactive region of real structures. Perhaps one of the most important physical parameters which determines the microwave activity of active devices is the quality factor Q defined [65] as the time average of the stored ac field energy, $\langle E \rangle$, divided by the ac power dissipation, $\langle dE/dt \rangle$, per radian, i.e.

$$Q \equiv \frac{\omega \langle E \rangle}{-\langle \frac{dE}{dt} \rangle} = \frac{B}{G} \qquad (8.2)$$

If the conductance is negative, then Q is negative. The Q factor gives information about the threshold and the build-up rate of oscillation when the negative conductance device is operated as an oscillator. The growth factor of oscillations, g, is related to Q as [65]

$$g = -\frac{1}{2Q} \qquad (8.3)$$

Thus a smaller magnitude of negative Q is preferred for proper and

efficient operation of active structures. For a given structure, the negative Q depends on the dc current density, operating frequency and temperature. Since the structure susceptance varies only slightly from its geometrical value B_o, the negative Q is primarily determined by the negative conductance of the structure. Curves C of Figs. 8.6 and 8.8 show the variation of the negative Q with dc bias current and operating frequency, respectively. The frequency-dependence of negative Q is plotted for $J_o = 35\ Acm^{-2}$ at which optimum microwave activity is obtained. The minimum Q of this structure, Q_{min}, is about 17 and occurs at f = 6.5 GHz.

8.2 Temperature-Dependence of the Small-Signal Admittance

It has been shown in the previous chapter that the MSM structure always dissipates dc electric energy. The thermal energy, into which the dissipated energy is converted, then heats the structure. The MSM structures are usually operated at current densities in the range of $10 \sim 100\ A\,cm^{-2}$ and at bias voltages of about 15 - 100 V. Depending on the contact area of the structure, the dc power dissipation may vary in the range of 0.5 - 8 W. Assuming a collecting contact thermal resistance of about 20°C/W, the semiconductor temperature may thus be more than 100°C above room temperature at high current levels. Snapp and Weissglas [12] have shown experimentally that the semiconductor temperature significantly affects the microwave activity of punched-through structures (the peak of the negative conductance shifts towards

lower frequencies and reduces in amplitude with increasing temperature). They have also reported that structures with Schottky barrier injecting contacts are more sensitive to temperature variation. The most important differences between p^+np^+ structures and the structure with MS injecting contact reported in ref. 12 are as follows:

(1) Optimum microwave activity of p^+np^+ structures occurs at a temperature well below 300°K (e.g. 100°K), while structures with a Schottky barrier injecting contact fail to exhibit any negative conductance at 100°K.

(2) At room temperature, the negative conductance of MSM structures is significantly less than the negative conductance of p^+np^+ structures.

(3) At higher temperatures (above 300°K) the microwave behavior of both structures is almost identical.

Because of the importance of temperature effects on the microwave behavior of MSM structures, the temperature-dependence of the small-signal admittance of the structure has been numerically investigated. In this section, the results of a numerical study on two representative PtSi-nSi-PtSi structures (structures A and B of Table 8.1) are graphically presented and discussed for two different crystal temperatures (T_c = 300°K and 423°K).

The frequency-dependence of the small-signal conductance and susceptance of the structure B is shown in Fig. 8.3 for J_o = 50 Acm^{-2}, at which optimum negative conductance is obtained, and for two different temperatures. For a given current density,

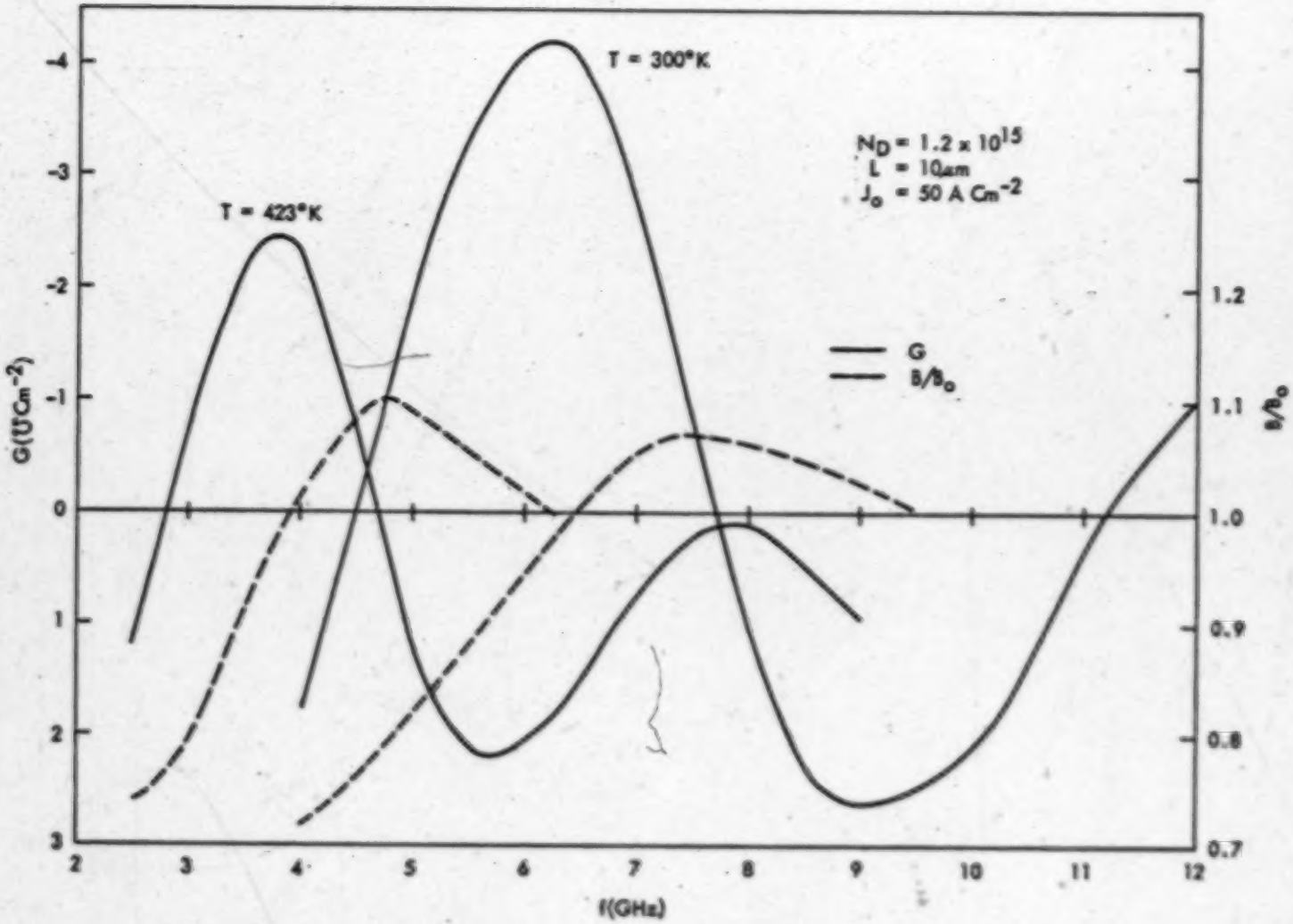

Fig. 8.3: Frequency Dependence of the Small-Signal Device Conductance and Normalized Susceptance of Structure B, for Two Different Temperatures.

the active frequency interval decreases with increasing temperature. It is also seen that the peak of the negative conductance decreases and shifts to lower frequencies; the temperature tuning coefficient, defined as

$$\alpha_T = \frac{1}{f} \frac{\Delta f}{\Delta T} \qquad (8.4)$$

is of the order of -10^{-3}/°C. If the crystal temperature is increased sufficiently, the width of the diffusion affected region increases and the carrier velocity in the high field region is greatly reduced. Both of these effects increase the carrier transit-time and hence reduce the optimum operating frequency. A reduction in the peak of negative conductance will also result from the above effects. At higher temperatures, mobile carriers do not attain scattering limited velocity in most of the semiconductor bulk. The carrier velocity is then a function of electric field throughout the entire semiconductor and thus, under ac conditions, allows more velocity modulation to occur. The power dissipation associated with velocity modulation current results in large ohmic losses which significantly reduce the negative conductance.

The small-signal susceptance of the structure B is shown by the dashed curves in Fig. 8.3. At the higher temperature, the structure susceptance shifts to lower frequencies because of the increase of the transit time of injected holes. For a given frequency, the structure susceptance increases with an increase of temperature. The capacitive nature of the electronic susceptance

becomes more pronounced at the higher temperatures which clearly indicates an additional phase delay associated with the carrier transport in the injection and low-field regions of the structure.

It is known that the width of the injection and low field region increases with a decrease of semiconductor doping concentration and/or an increase of temperature [43]. Since most of the power dissipation occurs within these regions the microwave activity of a structure with a lightly doped semiconductor can be significantly reduced at high temperatures. To show the effect of the crystal temperature on the negative conductance of lightly doped structures, the computations were repeated for the structure A. Fig. 8.4 shows the frequency-dependence of the structure conductance for $J_0 = 30\ Acm^{-2}$, at which maximum microwave activity is obtained, and for the same temperature as described in the previous figure. According to Fig. 8.4, the magnitude of the negative conductance is greatly reduced by increasing temperature. Further, the active frequency interval becomes narrower than that of structure B. If the crystal temperature of lightly doped MSM structures ($N_D \sim 10^{14}\ cm^{-3}$) is increased considerably, conditions can occur in which the velocity of charged carriers does not saturate anywhere in the semiconductor bulk. Consequently, large ohmic losses will occur, and the microwave activity of the structure is degraded significantly.

8.3 Effects of the Physical Parameters on the Small-Signal Behavior

To design an MSM oscillator or amplifier, there are many

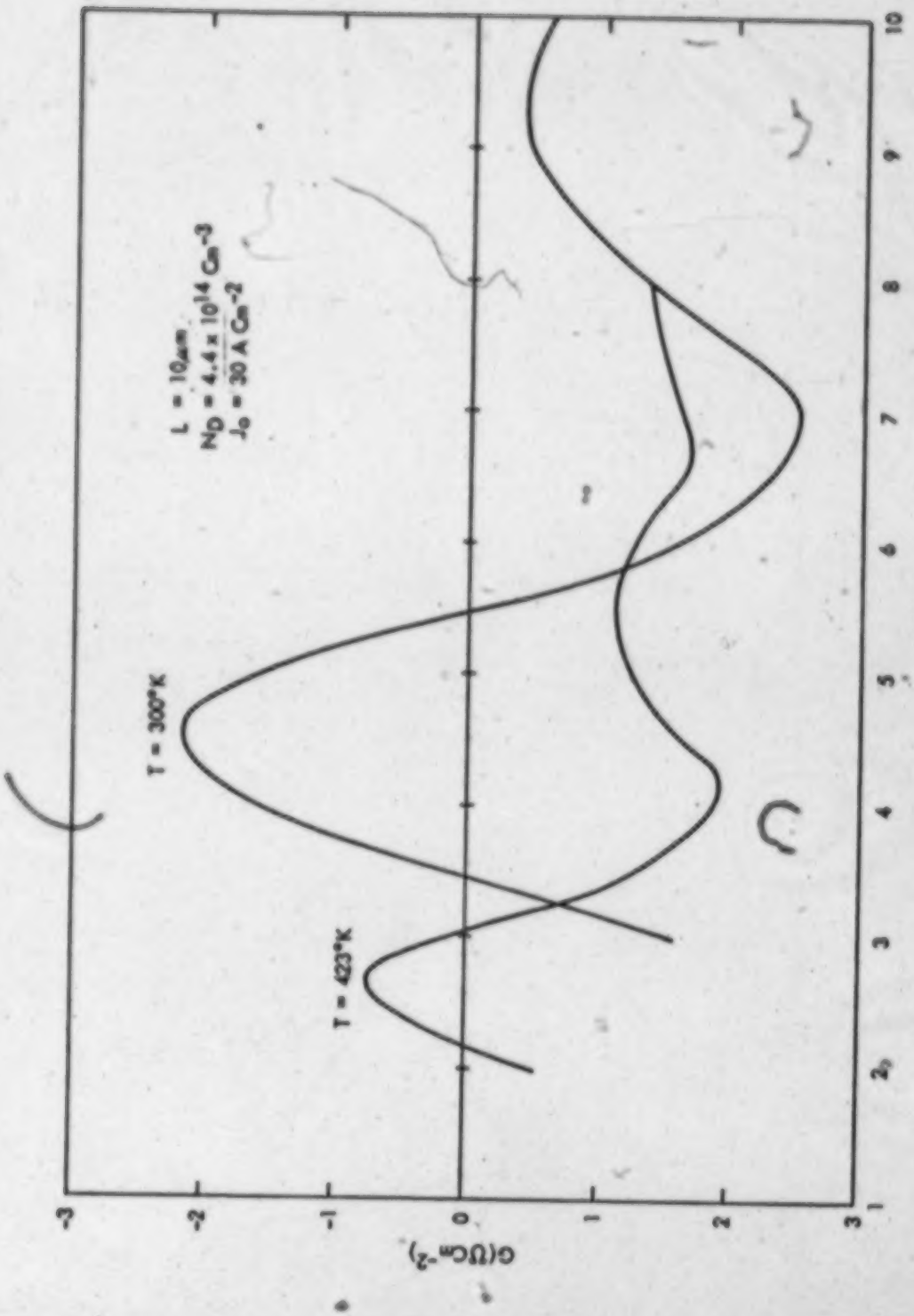

Fig. 8.4: Frequency-Dependence of the Small-Signal Device Conductance of Structure A, for Two Different Temperatures.

parameters that can be adjusted to obtain optimum performance. The semiconductor width, the doping concentration, the barrier heights of the MS contacts and the device area are the most important initial design parameters. The semiconductor width will, of course, be of prime importance in determining the frequency of operation. The low-frequency resistance of the injection and low-field regions will not only be influenced by the doping concentration and its profile, but also by the barrier height of the MS contacts. High injection of minority carriers is required for efficient operation and hence contacts with low barrier heights for minority carriers are preferred. The barrier height, however, depends mainly on the type of metal and semiconductor being used. PtSi-nSi-PtSi structures (investigated in the present study) have the lowest barrier height for injected holes and therefore they are most commonly used. Consequently, the semiconductor width L and the doping concentration N_D are the adjustable physical parameters.

The choice of optimizing the negative conductance G or the negative resistance R of the structure will depend on the device application. The parallel admittance is more appropriate for most applications; thus the optimization of the negative conductance G is mainly considered here. To establish design criteria for a punch-through structure, the dependence of the small signal behavior of the device upon N_D and L have been investigated. The results are graphically presented and discussed in this section.

The computed negative conductance, G, as a function of the dc current density, is shown in Fig. 8.5 for structures A, B, C

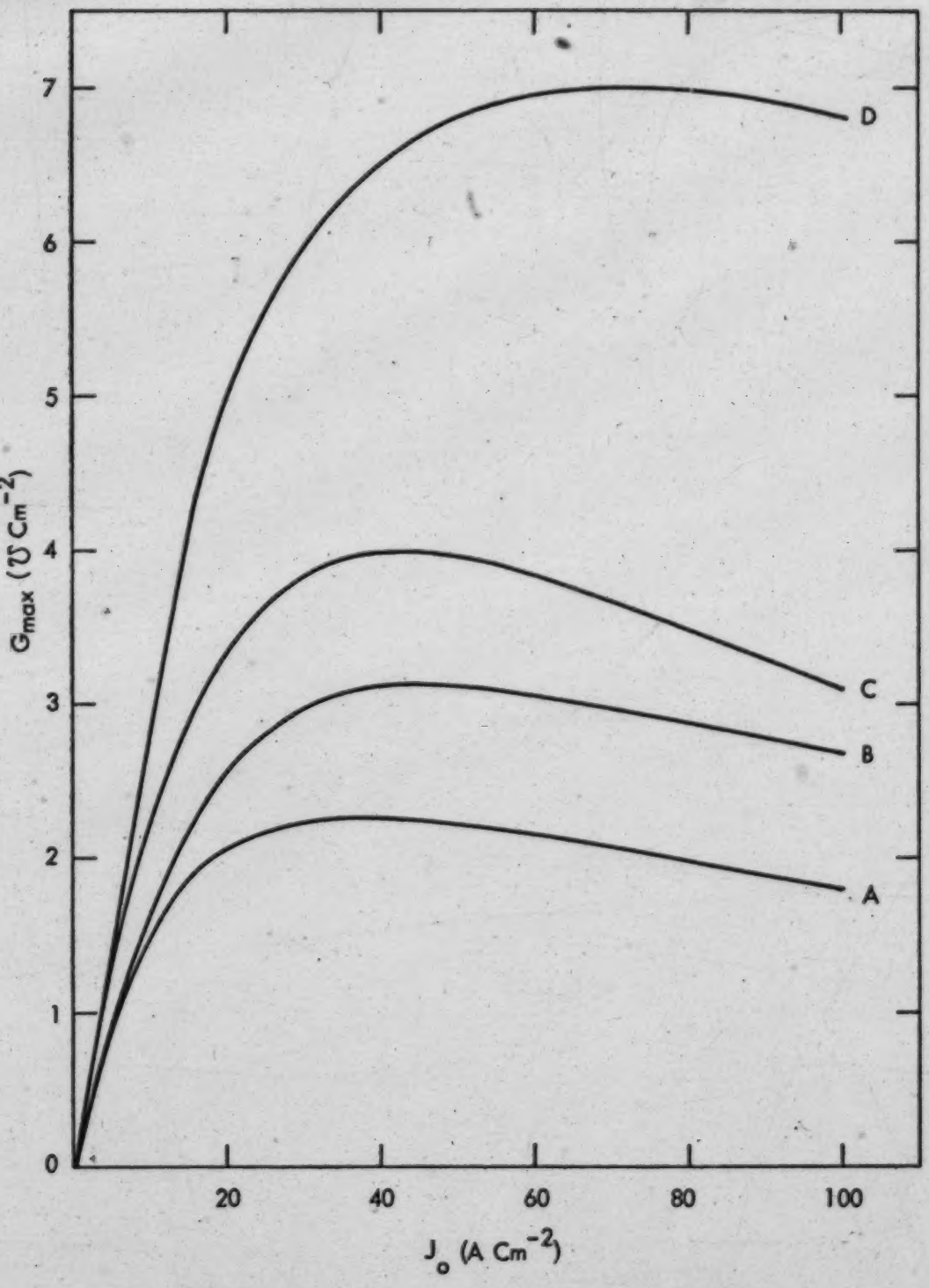

Fig. 8.5: Constant Frequency, Small-Signal Conductance G Versus Current Density for Structures A, B, C and D.

and D. The curves are evaluated at the optimum frequency of a given structure. In most structures, the negative conductance increases rapidly with current density and reaches a broad maximum at relatively low current densities (less than 50 Acm^{-2}). The optimum current density increases with an increase of frequency, from 30 Acm^{-2} at 4 GHz for the structure A to 80 Acm^{-2} at 12 GHz for structure D. Figure 8.5 also shows that the optimum negative conductance is larger for higher frequency structures. This might imply that the microwave activity of high frequency devices is better than those operating at relatively lower frequencies. This conclusion is not always true, since an increase of the operating frequency results in an increase of the device susceptance as well as the negative quality factor. Structures with higher quality factors are greatly affected by the conductive losses occurring in the semiconductor substrate, contacts, etc. These losses can be represented by a small resistance connected in series with the equivalent circuit of the structure [12]. The effects of the series losses upon the computed microwave behavior of various structures, as described above, are shown in Figs. 8.6, 8.7 and 8.8. In these figures, a series resistance of 0.15 $m\Omega\text{-}cm^2$ independent of frequency is assumed for all structures [12].

Figure 8.6 shows the minimum quality factor as a function of the dc current density for the structures A, B, C and D. The minimum quality factor, Q_{min}, for a particular structure occurs at a current density very close to the value at which optimum negative conductance occurs (see Fig. 8.5). Figure 8.6 also

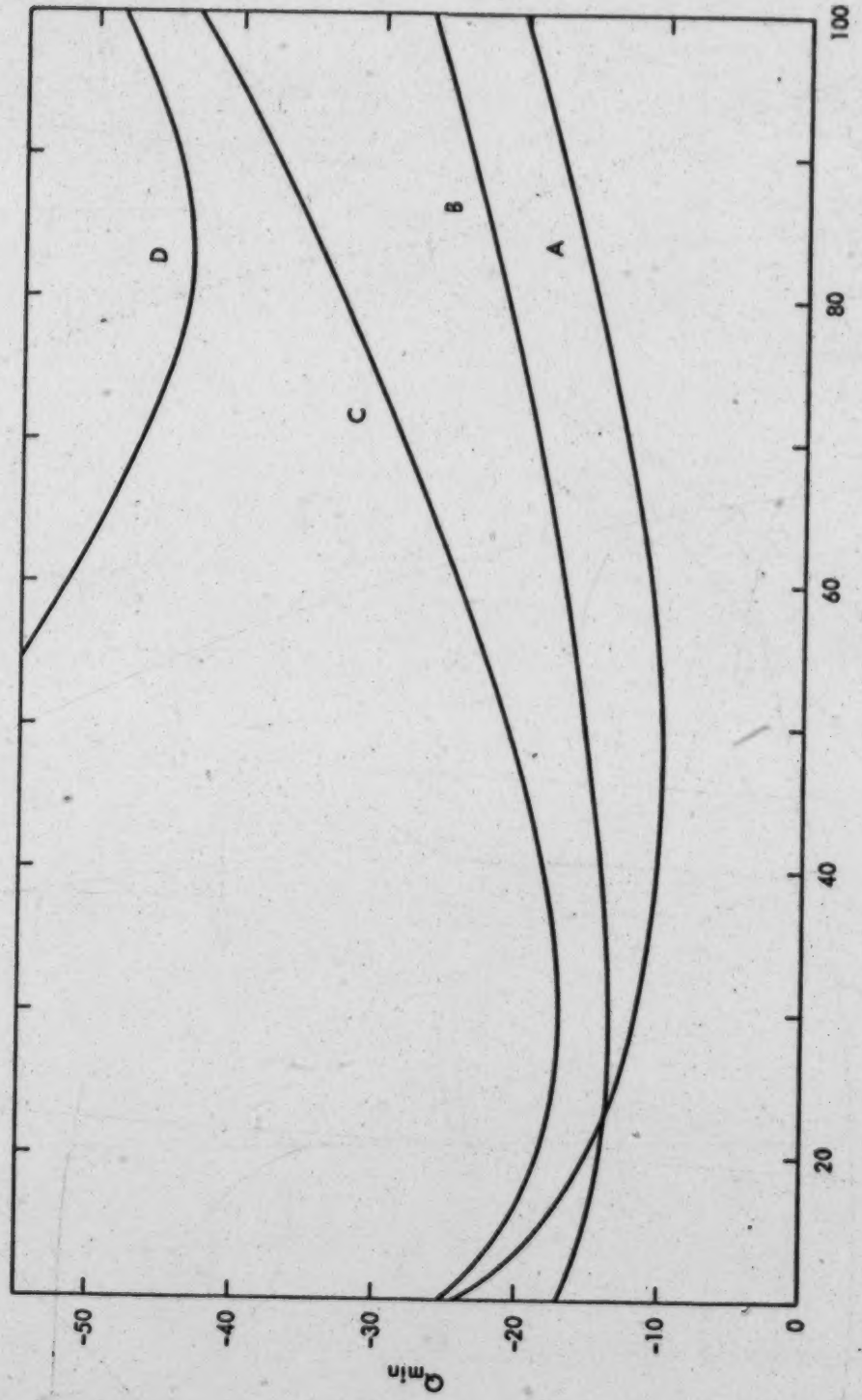

Fig. 8.6: Minimum Negative Quality Factor Versus Current Density, for Structures A, B, C and D.

indicates that Q_{min} increases appreciably for the higher frequency structures (e.g. structure D).

The effect of the series losses upon the structure performance can be clearly seen in Fig. 8.7. This figure shows the frequency dependence of negative conductance of the same structures described in Fig. 8.6. Dashed curves in the figure show the actual behavior (where R_s = 0.15 mΩ cm^2 is included) while solid curves correspond to ideal behavior (where the effect of R_s is disregarded). These curves are evaluated at the optimum dc current density of a given structure. According to this figure, the investigated structures show a negative conductance throughout almost an octave frequency range. The active frequency interval as well as the peak of the negative conductance are greatly reduced in the case of high frequency structures (structure D), while the behavior of low-frequency structures (structure A) is slightly affected.

The pronounced effect of the series loss resistance R_s upon the microwave capability of high frequency structures is directly related to the small negative resistance which can be obtained from those structures. To clarify this point we have calculated the negative resistance of the previously described structures and the results are graphically presented in Fig. 8.8. This figure shows the frequency dependence of the negative resistance calculated at the optimum current density of the particular structure. The figure also shows the negative quality of each structure as a function of frequency. The negative resistance curves are more indicative in describing the power capability of the structure. The figure clearly indicates that the

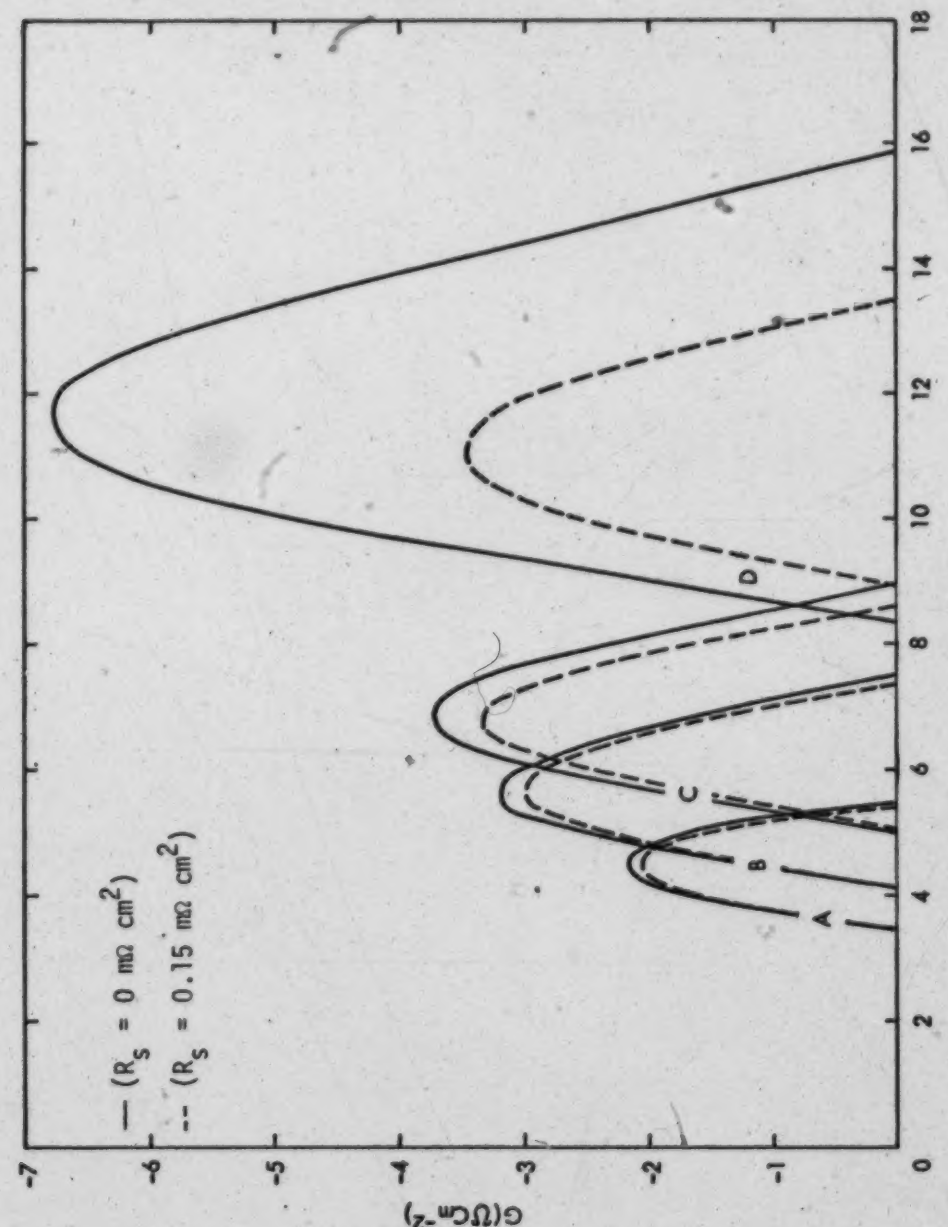

Fig. 8.7: Frequency Dependence of the Small-Signal Conductance of Real (Dashed Curves) and Ideal (Solid Curves) Structures A, B, C and D.

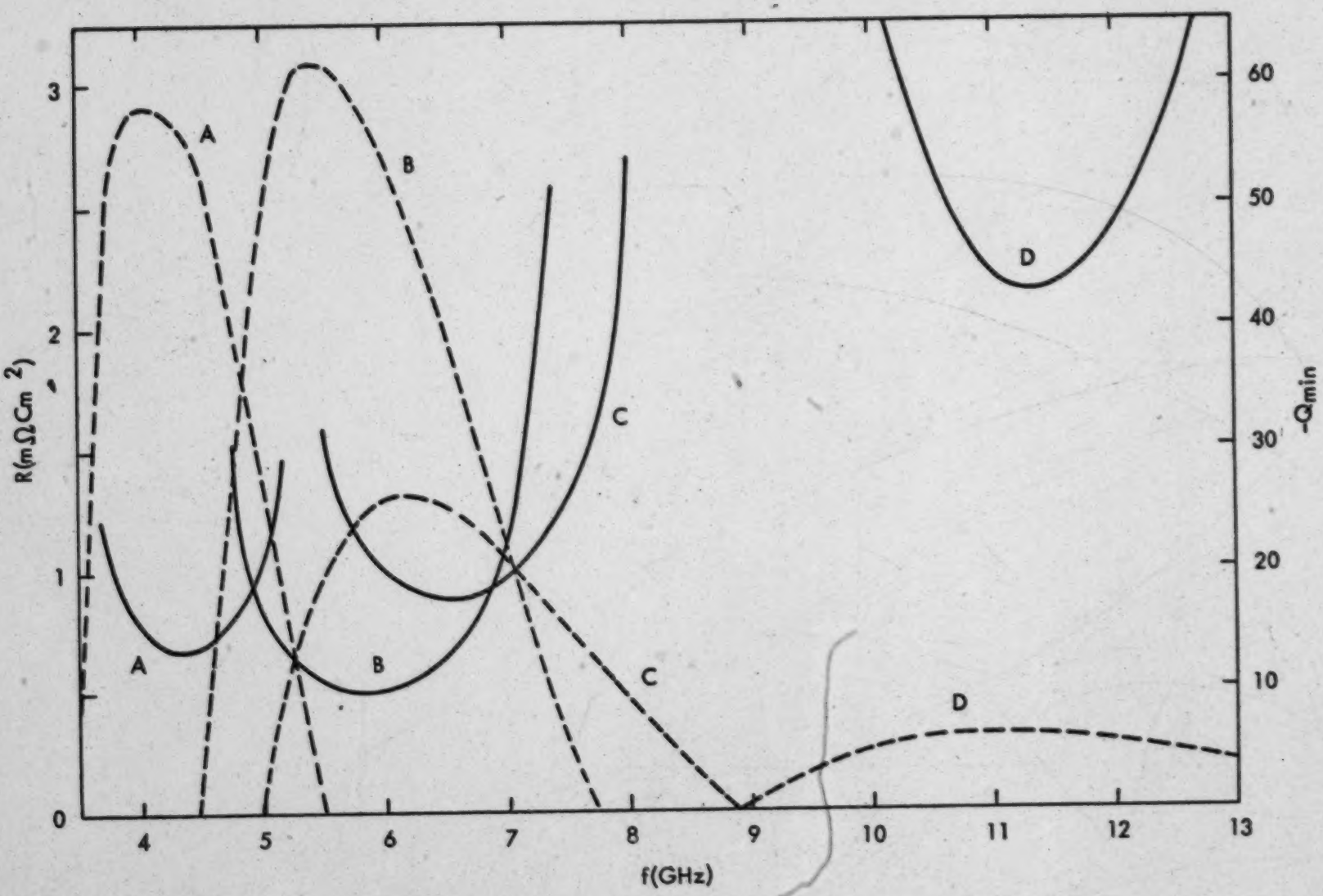

Fig. 8.8: Frequency Dependence of the Small-Signal Resistance (dashed curves) and the Negative Quality Factor (solid curves) for Structures A, B, C and D.

structure negative resistance is greatly reduced in structures operating at higher frequencies. The effect also results in larger Q_{min} for high frequency structures.

The frequency dependence of the susceptance of the structures A, B, C, and D is shown in Fig. 8.9. The capacitive effects in lightly doped structures (e.g. structure A) are more pronounced than in the case of highly doped structures (e.g. structure D). Compared to other solid-state devices (e.g. IMPATT diodes), the electronic contribution to the susceptance of punch-through structures, near the optimum operating frequency is insignificant. As a result, the device susceptance deviates only slightly from its geometrical value, which is a great advantage of these devices.

In addition to the characteristic features described above, a comparison between various structures (which differ in semiconductor width and/or doping concentration) shows that the peak of the negative conductance as well as the operating frequency are functions of the physical parameters L and N_D. For example, comparison of curves A and B in Fig. 8.6 indicates that the peak of the negative conductance and the corresponding frequency increases with increasing doping concentration. Curves B and C in the same figure show that a reduction in the semiconductor width yields a higher operating frequency and a larger negative conductance. To help establish a design criterion for the punch-through structures, the effect of each parameter has been numerically studied and the computed results are graphically presented in Figs. 8.10 and 8.11.

Figure 8.10 shows the frequency dependence of the negative

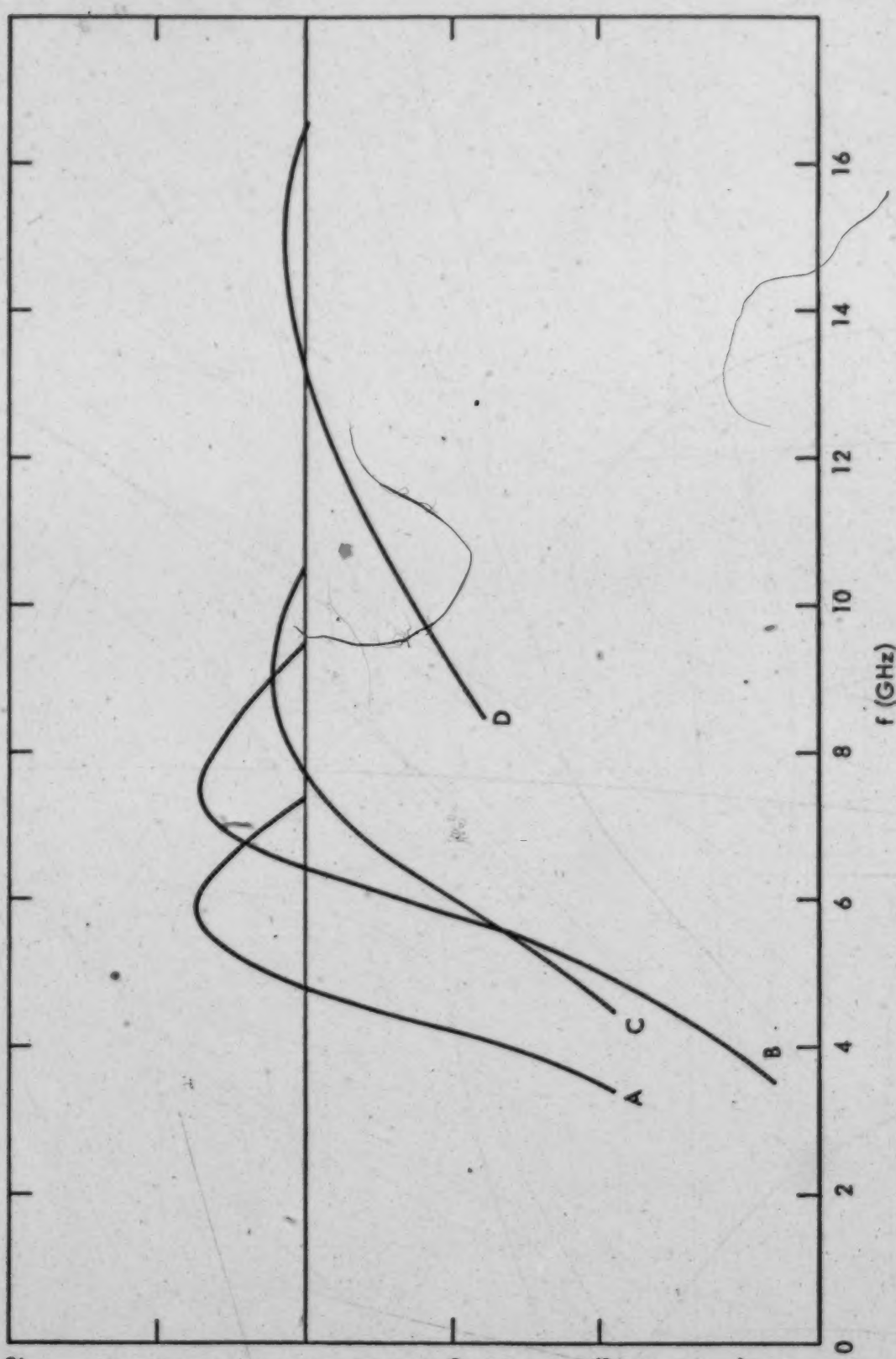

Fig. 8.9: Frequency Dependence of the Normalized Structure Susceptance for Structures A, B, C and D.

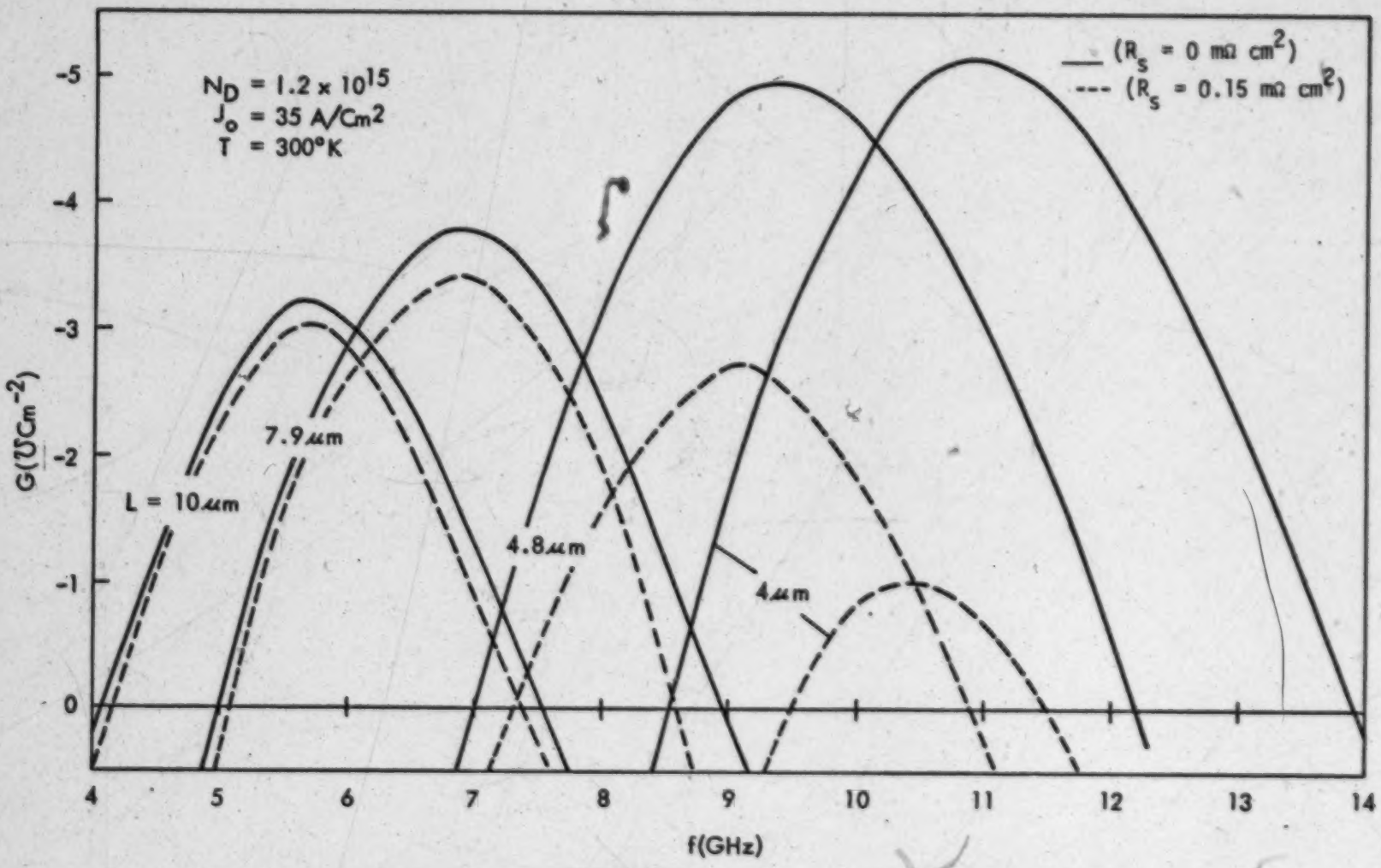

Fig. 8.10: Frequency Dependence of Negative Conductance for Four Structures Having the Same Doping Concentration and Differing in Semiconductor Width. Solid curves represent ideal structures (R_s = 0 mΩ cm^2) and dashed curves represent real structures (R_s = 0.15 mΩ cm^2).

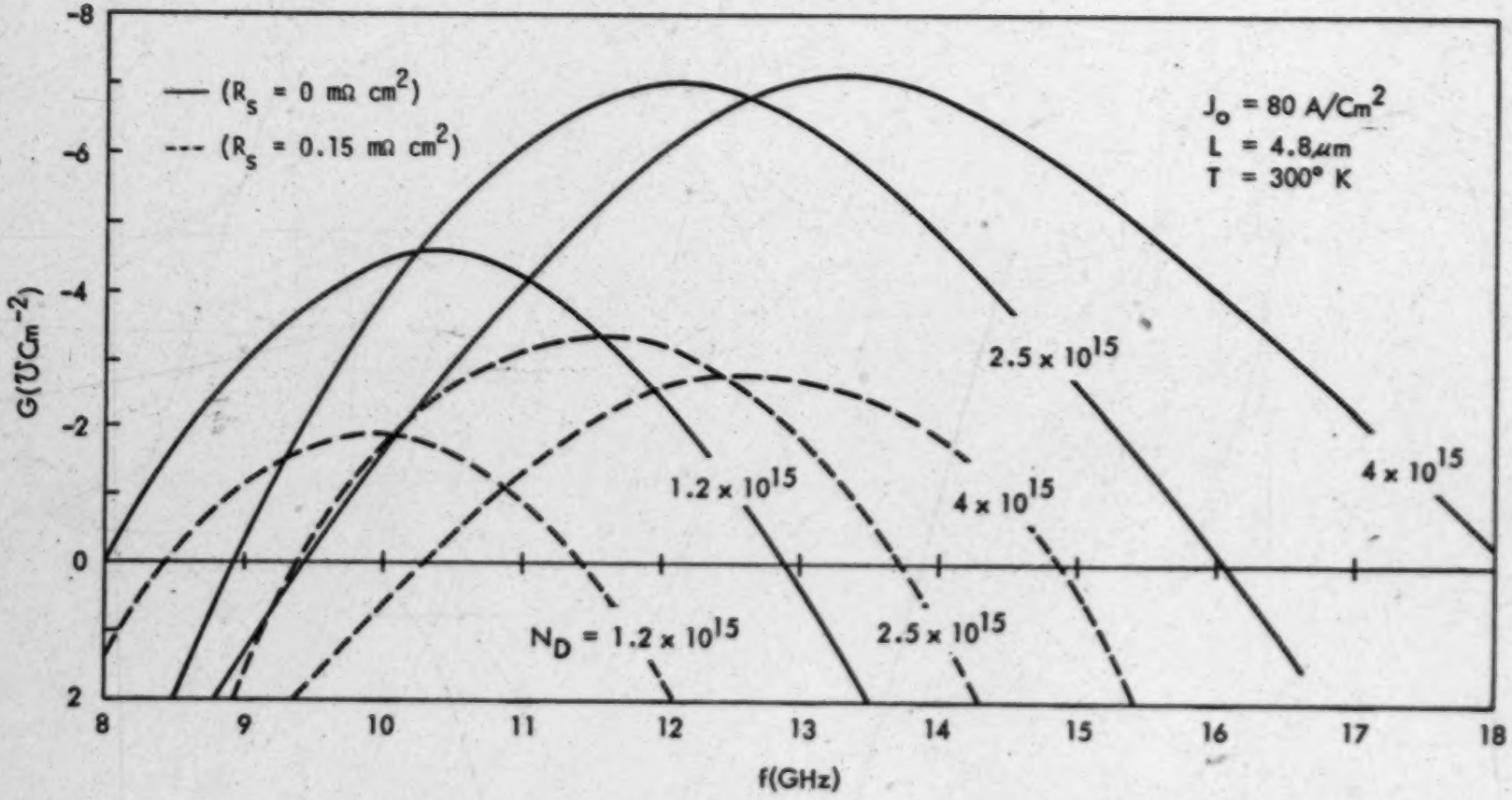

Fig. 8.11: Frequency Dependence of the Negative Conductance for Three Structures (L = 4.8 μm) Which Differ in Doping Concentration. Solid curves represent ideal structures (R_s = 0 mΩ cm^2) and dashed curves represent real structures (R_s = 0.15 mΩ cm^2).

conductance G for the four structures having the same doping concentration, $N_D = 1.2 \times 10^{15}$ cm^{-3} (most commonly used in actual devices), and differing in the semiconductor width L. Figure 8.11 shows the same dependence as in Fig. 8.10, for three structures which differ in the semiconductor doping but have the same semiconductor width, L = 4.8 μm. The solid curves in these figures represent the idealized structures ($R_s = 0$ mΩ cm^2) while the real structures ($R_s = 0.15$ mΩ-cm^2) is described by the dashed curves.

According to Fig. 8.10, the negative conductance of idealized structures increases as the width of the semiconductor decreases. However, the negative conductance of real structures is greatly reduced as the semiconductor width is sufficiently decreased. The reduction of the negative conductance at excessively smaller widths is due to the small negative series resistance that can be obtained from the structure as previously described in Fig. 8.8.

Figure 8.11 indicates that the peak of the negative conductance initially increases with an increase of doping concentration and reaches a maximum at a doping concentration somewhat greater than 2.5×10^{15} cm^{-3}. Further increase in the doping concentration results in a slight reduction of the peak of the negative conductance. The reduction of the negative conductance at lower doping concentrations is expected to occur because of the increase of the injection and low field regions of the structure (as described in Chapter VI).

To aid the optimization of the microwave activity of MSM structures, the results of extensive calculations are summarized in Figs. 8.12 and 8.13. According to Fig. 8.12 the semiconductor

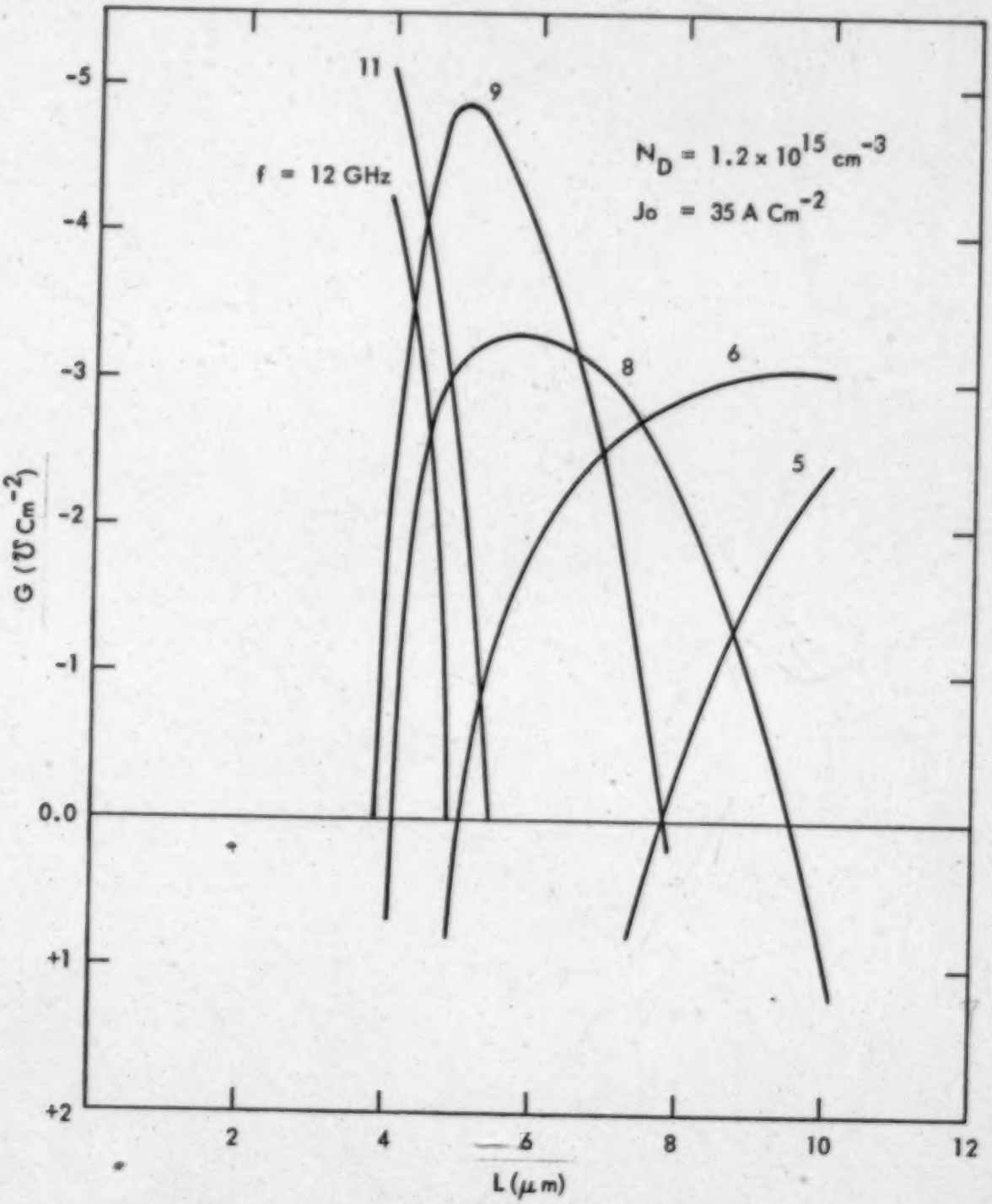

Fig. 8.12: Small-Signal Conductance Versus the Structure Width L, with Fixed Doping Concentration $N_D = 1.2 \times 10^{15} cm^{-3}$.

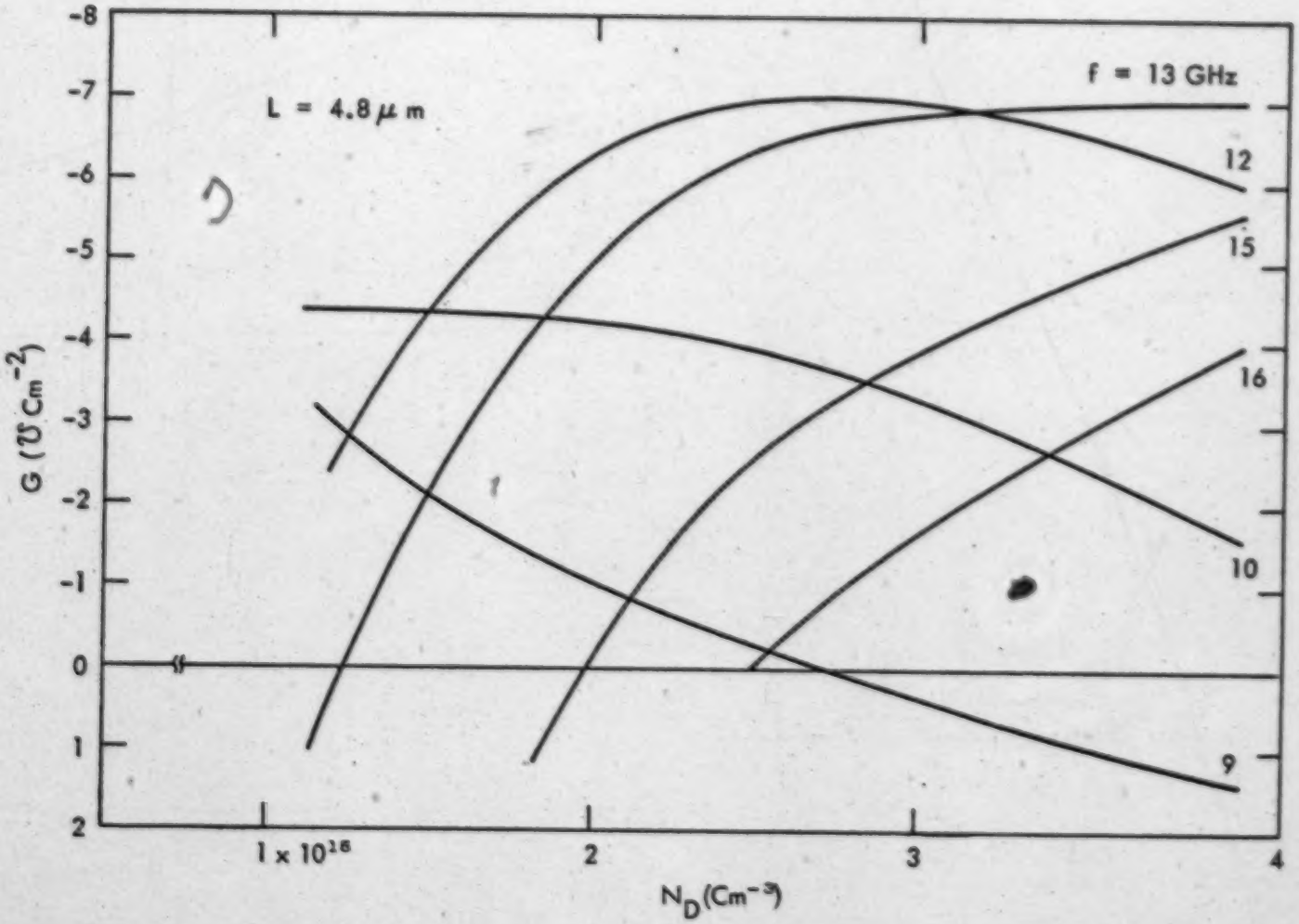

Fig. 8.13: Small-Signal Conductance Versus Doping Concentration, N_D, with Fixed L = 4.8 μm.

width becomes a very critical parameter at higher frequencies while at relatively lower frequencies a wide range of semiconductor widths can equally well be employed. It is seen in Fig. 8.13 that for doping concentrations exceeding 10^{15} cm^{-3}, the microwave behavior is not very sensitive to variation of doping concentration. If the structure will be operated at relatively high frequency and in a narrow frequency range the optimum doping concentration can be determined from Fig. 8.13. Structures which are expected to operate at low frequencies (less than 4 GHz) will permit a very limited choice of both L and N_D. Since the operating frequency primarily determines the semiconductor width, very low-frequency devices require a large semiconductor width. Consequently, a relatively lower doping concentration ($\sim 10^{14}$ cm^{-3}) must be employed in order to maintain the bias voltage well below avalanche breakdown. For doping concentration of the order of 10^{14}, the ohmic losses in the injection and low-field regions become excessively large and the microwave activity of the structure is greatly degraded. These losses set the lower frequency limit at which punch-through MSM structures can be efficiently used for microwave applications.

In summary, the MSM structure can be employed for energy generation and amplification in the frequency range 1 - 15 GHz. Near the lower frequency limit, the choice of both L and N required for optimization purposes is very limited; the former is determined from the operating frequency while the latter is determined from the biasing requirement. In the frequency range

(~ 3 - 8 GHz), where both the semiconductor width and doping concentration are no longer critical parameters, the MSM structure can be constructed for a wide range of bias voltages by proper choice of these parameters (as described in Chapter VI). At higher frequencies, the semiconductor width is determined by the operating frequency and the semiconductor doping and bias current density are left for various optimization procedures.

CHAPTER IX

COMPARISON OF VARIOUS MODELS AND MEASURED DATA

The study undertaken in this thesis has been carried out with the intent of substantiating the validity of various theoretical models in describing the actual behavior of punch-through MSM devices. Detailed investigation of the injection and low-field regions (Chapter VII) indicates that the diffusion of injected holes as well as the physical conditions of the injecting contact can significantly affect the small-signal properties of the structure. In particular, it is shown in Figs. 7.3 and 7.6 that neglecting carrier diffusion and/or assuming current-independent boundary concentration yields results which overestimate the microwave capability of the MSM structure. This is more pronounced in devices operating at high current densities.

In order to verify the validity of various models, the computed results are compared with the experimental results of Snapp and Weissglas [12] which are the only published data on structures with a Schottky barrier injecting contact. In addition, comparison of the exact numerical model (which includes all the significant physical processes) with other models has also been made to show the effects of the two simplifying assumptions made above upon the terminal small-signal behavior.

The frequency dependence of the computed small-signal conductance (resistance) of an MSM structure (semiconductor width

$L = 7.9\ \mu m$, doping concentration $N_D = 1.2 \times 10^{15}\ cm^{-3}$ and contact area $A = 3 \times 10^{-4}\ cm^2$) is compared with the measured data of Snapp and Weissglas [12] in Fig. 9.1. The results are displayed for a dc current density of 35 A cm^{-2} at which optimum microwave activity occurs. The figure shows the actual behavior of the structure as predicted by various models by including a series loss resistance $R_s = 0.5\Omega$ measured by Snapp and Weissglas [12]. The solid curve in the figure corresponds to the exact numerical model; dashed-dot curve is the computed results of a simplified numerical model which assumes current-independent boundary concentration $\tilde{p} = 0$ at both contacts. The dashed curve represents the analytical model which neglects the effect of carrier diffusion and also assumes that $\tilde{p} = 0$ in the entire injection region.

According to this figure, the computed frequency range is in close agreement with the measured data of Snapp and Weissglas [12]. The optimum operating frequency, f_{opt}, of the experimental results is seen to be higher by less than 10% as compared to f_{opt} given by various models. Since an increase in the semiconductor temperature results in lowering f_{opt} [12,43], it is clear that this discrepancy is not due to thermal effects. There appear to be two reasons for this difference. Firstly, there is uncertainty in the measurement of the structural parameters, for example, the semiconductor width L and the contact area A. The error in the determination of L results in an error of the same order of magnitude in calculating carrier transit time and hence operating frequency. The contact area determines the doping density; an error in A will also cause a proportionate error in N_D as well as the current density J_o.

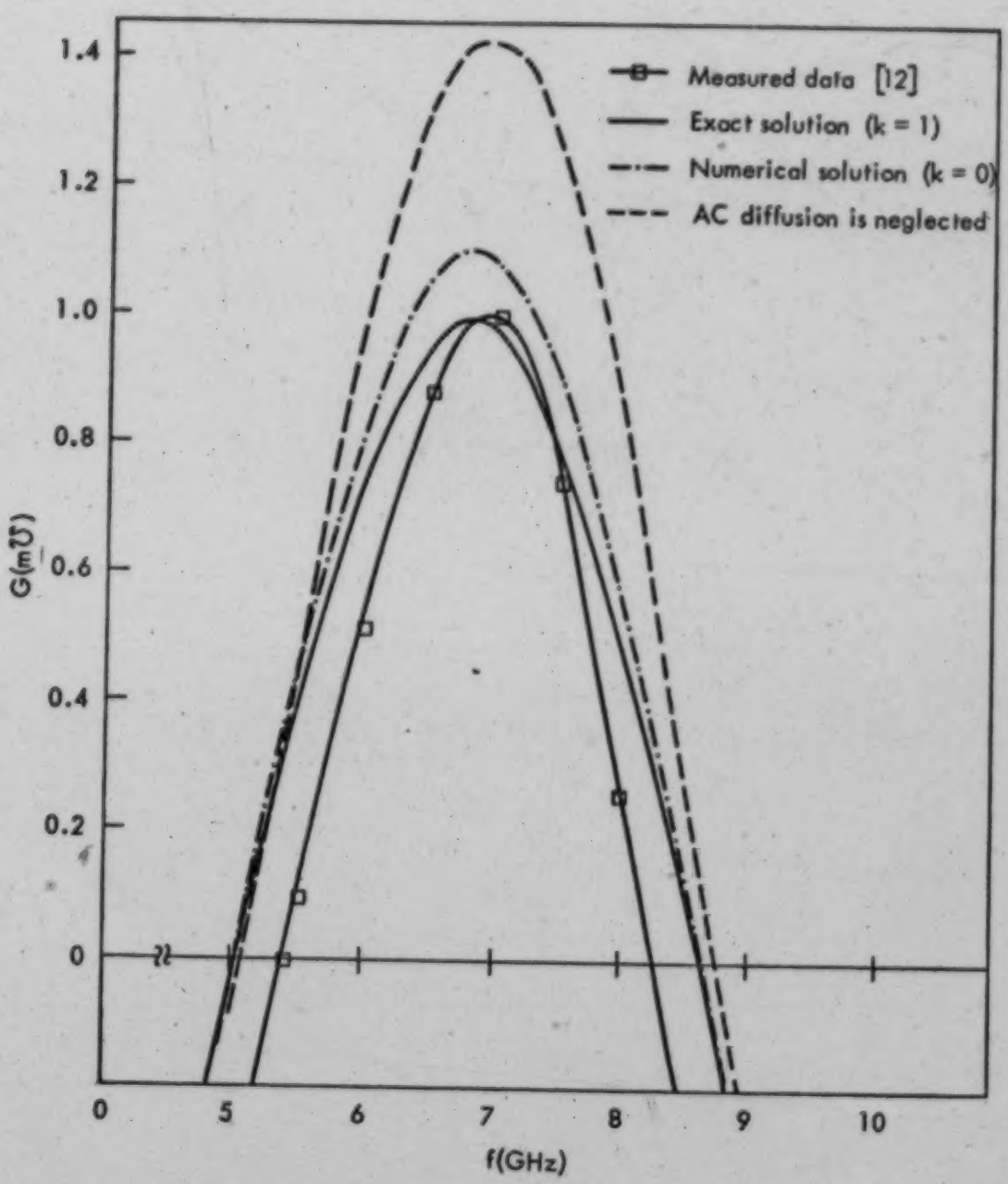

Fig. 9.1a: Small-Signal Device Conductance as a Function of Frequency

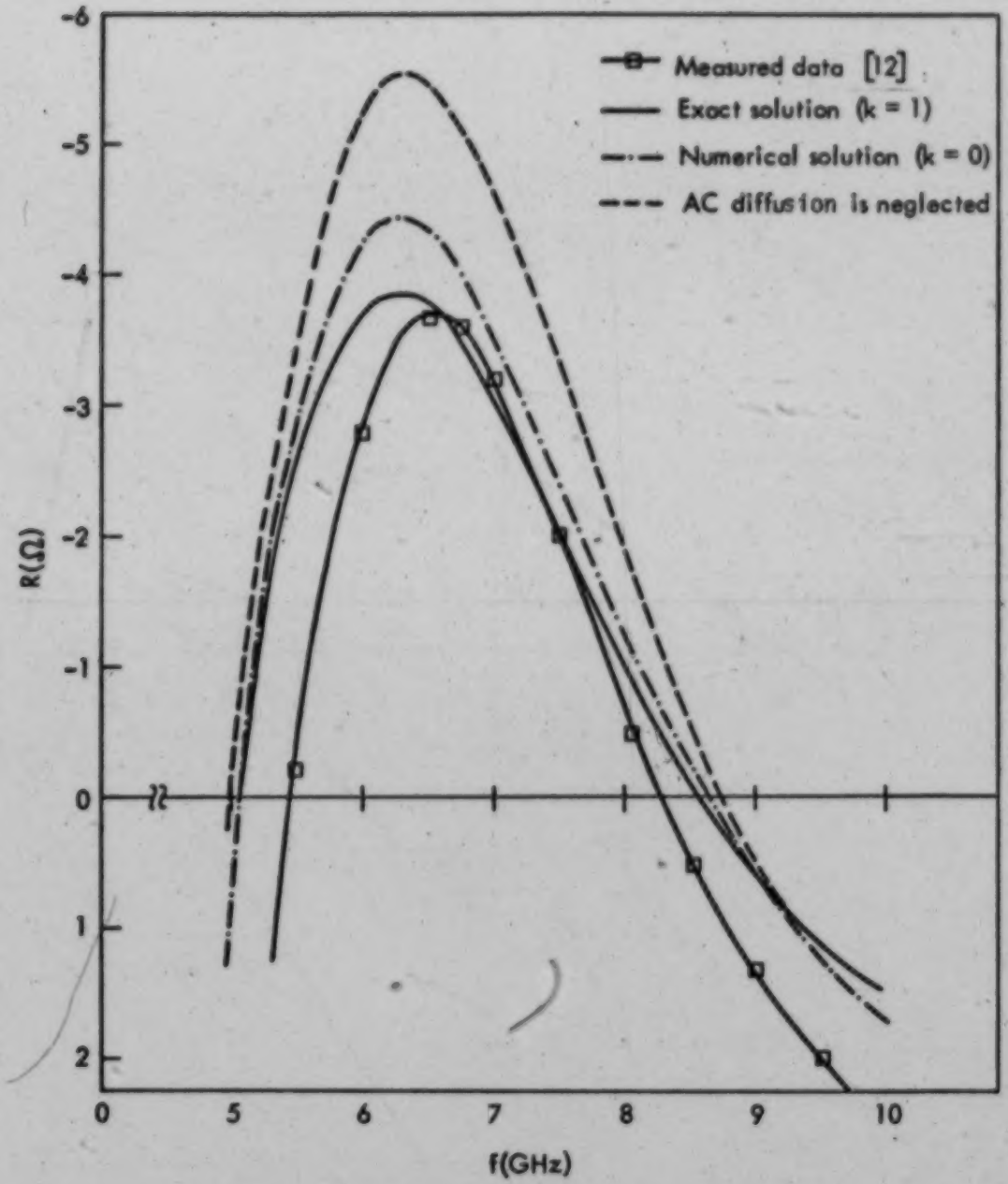

Fig. 9.1b: Small-Signal Device Resistance as a Function of Frequency.

N_D and J_o affect the electric field profile and hence the carrier drift velocity; the latter primarily determines the transit time and also the operating frequency. Secondly, Eq. 5.5, the mobility expression used in the theoretical results, is an empirical relationship based upon measured data; an error in carrier mobility will lead to an error in the computed value of f_{opt}.

It is also seen in Fig. 9.1 that the exact as well as the simplified theoretical models proposed in the present work predict identical active frequency ranges, that is, the ranges over which the conductance is negative. Since all the models are based on the exact charge transport properties of the structure (Chapter III), the agreement between various models in predicting the active frequency range clearly indicates that the operating frequency is predominantly determined by the dc conditions of the structure. Therefore, analytical small-signal studies which consider the effect of dc diffusion processes upon the carrier velocity in the injection and low-field regions describe accurately the operating frequency range of punch-through devices.

In Fig. 9.1, the optimum dc current density, J_o ($35\ Acm^{-2}$), is small compared with the saturation current density J_{sat}. Under this condition, the exact and simplified numerical models give results which are in close agreement. According to Eq. 4.28, the boundary concentration of injected holes decreases significantly as J_o becomes comparable to J_{sat}. This operating condition is usually encountered in high frequency structures. The reduction of the concentration of injected holes at the forward biased contact can cause a significant degradation of the microwave performance of the

structure. Therefore, simplified boundary conditions become rather too restrictive in describing the high current operation of punch-through MSM structures. This fact is further emphasized in Fig. 9.2

It is also seen in Fig. 9.1 that neglecting carrier diffusion results in overestimating the magnitude of the negative conductance that can be exhibited by the structure. The diffusion processes affect the formation of the bunch of ac holes and hence the small-signal properties of the structure (Chapter VII). It is shown in Fig. 7.6, that the carrier diffusion reduces the magnitude of the ac conduction current as well as the ac electric field. As a result, neglecting carrier diffusion will result in a negative conductance which is too large as compared to the value obtained when ac diffusion is taken into account. The above effects become progressively more pronounced at higher current densities where the space charge is significantly large. At very low dc current densities, on the other hand, the ac conduction current is a small fraction of the total ac current and the structure acts essentially as an insulator. Thus the charge transport processes (including diffusion) have only a small effect on the overall behavior of the structure.

The effects of the injecting contact boundary condition and the diffusion processes of mobile holes upon the calculated negative conductance peak at various operating current densities discussed above is shown in Fig. 9.2. ΔG_p is the difference between the negative conductance computed from the exact model, G_p, and that

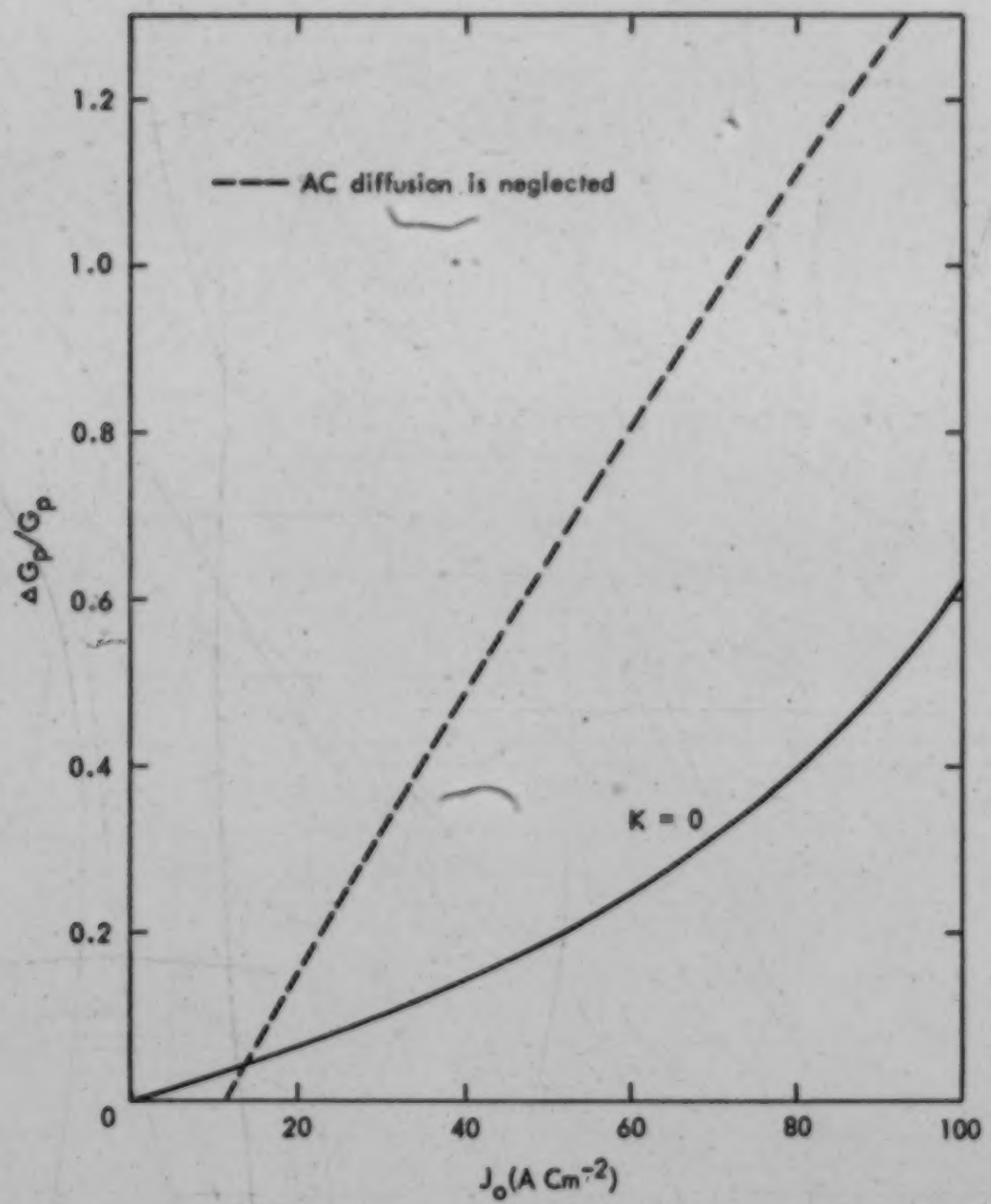

Fig. 9.2: The Normalized Difference $\Delta G_p/G_p$ as a Function of Current Density. ΔG_p is the Difference Between the Negative Conductance Computed From the Exact Model, G_p, and that Obtained From Various Simplified Models.

obtained by employing the simplified boundary condition (solid curve) or by neglecting diffusion processes (dashed curve). As an example, if 10% deviation is considered adequate in describing the device behavior accurately, numerical models employing simplified boundary conditions are valid up to $J_0 = 30\,A\,cm^{-2}$, whereas neglecting ac carrier diffusion restricts this value of J_0 to $15\,A\,cm^{-2}$.

CHAPTER X

SUMMARY AND CONCLUSIONS

The dc and small-signal ac behavior of punch-through MSM structures have been investigated. A numerical model of the structure which takes into account carrier diffusion, a realistic dependence of the carrier velocity upon electric field and properly defined boundary conditions has been formulated. The model has been applied to the calculation of both dc and small-signal ac characteristics of various PtSi-nSi-PtSi structures.

The dc properties of the MSM structures are the following:

(1) The current increases exponentially with an increase of the applied voltage for current densities less than about 10 Acm^{-2}. At higher current densities, the J-V characteristics deviate from the exponential dependence because of the space charge effects of injected holes.

(2) Close to the saturation current, the J-V characteristic levels off very rapidly due to finite carrier injection at the forward-biased MS contact.

(3) The maximum attainable (saturation) current is limited by the semiconductor temperature and the injecting contact barrier height for mobile holes.

(4) At technically important current-density levels (10 - 80 Acm^{-2}) and in the temperature range 300 - 423°K, the J-V characteristics are relatively insensitive to temperature variation. However, the physical conditions in the injection and

low-field regions (which determine the ac properties of the structure) exhibit an appreciable temperature dependence.

The small-signal properties of punch-through MSM structures are summarized as follows:

(1) The MSM structure possesses negative conductance (resistance) in the microwave frequency range because of the combined effects of the barrier control of charge injection and finite transit time of charge carriers. Most of the phase delay occurs in the high-field drift region and arises from the transit time of injected holes which move with nearly constant velocity. Additional phase delay associated with the charge transport in the injection and low-field regions is also present.

(2) The negative conductance (resistance) is relatively small and the electronic susceptance which is a small percentage of the device susceptance varies from inductive to capacitive within the active frequency interval.

(3) At high temperatures, the microwave activity of the structure is greatly degraded; the negative conductance reduces in magnitude, shifts to lower frequency, and the active frequency range becomes very narrow.

(4) The isothermal calculations indicate that the negative conductance increases in magnitude and shifts to higher frequencies with an increase of the dc current density and reaches a maximum at relatively low current densities (less than 50 Acm^{-2} for most of the investigated devices). At higher current densities the magnitude of the negative conductance decreases because of the

space charge effects.

(5) The negative quality factor of the structure is relatively large (in the range 15 - 30 and more) which indicates that the small negative conductance of the structure can be easily offset by positive conductance due to losses as well as external circuitry.

The computed small-signal negative conductance and resistance are found to be in close agreement with the available experimental data of Snapp and Weissglas [12]. Comparison between the computed results of the exact model and other simplified models described in this thesis indicated that carrier diffusion and the reduction of the injecting contact boundary concentration of mobile holes greatly reduce the microwave activity of the structure. Detailed investigation of the injection and low field regions revealed that neglecting carrier diffusion in these regions, especially at high current levels, would yield results which are considerably different from the actual behavior.

The computed results of various structures investigated in this study, supplemented by the available experimental data, suggest that MSM structures can be employed for energy generation and amplification in the frequency range 1 - 15 GHz. The negative conductance (resistance) of each structure is relatively small and hence the power capabilities of these devices are much smaller than those of other microwave devices (e.g. IMPATT and Gunn diodes). However, the inherent low-noise properties of BARITT diodes [9], combined with their structural simplicity and less strenuous

operating conditions make these devices ideally suited for low power applications such as local oscillators and reflection type amplifiers. The microwave performance of BARITT diodes can be optimized if the physical parameters (N_D and L) of the structure are properly selected. At low frequencies (1 - 2 GHz) a limited choice of semiconductor width and doping concentration can be made; they are determined by the operating frequency and applied bias voltage. At frequencies approaching the upper limit, the semiconductor width is a very critical parameter and is primarily determined by the operating frequency while doping concentration and bias voltage are left for various optimization procedures.

In general, BARITT diodes made of Si semiconductors are simple to construct using existing technology and thus are of great practical importance. They are found to be extremely stable and have proved to be reliable and consistent in operation [8-12]. Present indications are that they will find wide practical application in systems where moderate power and low noise levels are required at low cost. Thus, the exact numerical model described in this thesis is of prime importance. The model, with its general characteristic, is useful for the design of BARITT diodes specially in the situation where many aspects of performance must be explored as functions of the diode structure and operating conditions [45]. It can be used for further investigation of the noise properties, large signal analysis and dynamic behavior of punch-through MSM structures. With a slight modification, the model can be used for a detailed study of other punch-through semiconductor structures such as p^+np^+, p^+nvp^+, etc.

REFERENCES

1. W.E. Wilson, "Pulsed LSA and TRAPATT Sources for Microwave Systems", Microwave Journal, Vol. 14, pp. 33-41, August 1971.

2. V.J. Higgins and J.J. Baranowski, "The Utility and Performance of Avalanche Transit Time Diodes and Transferred Electron Oscillators in Microwave Systems", Microwave Journal, Vol. 13, pp. 37-42, July 1970.

3. W. Shockley, "Negative Resistance arising from Transit Time in Semiconductor Diodes", Bell Sys. Tech. J., Vol. 23, pp. 799-826, July 1954.

4. H. Yoshimura, "Space Charge Limited and Emitter Current Limited Injection in Space Charge Region of Semiconductors", IEEE Trans. Electron Devices, Vol. ED-11, pp. 414-422, September 1964.

5. G.T. Wright, "Punch-Through Transit Time Oscillator", Electron Lett., Vol. 4, pp. 543-544, November 1968.

6. H.W. Rüegg, "A Proposed Punch-Through Microwave Negative Resistance Diode", IEEE Trans. Electron Devices, Vol. ED-15, pp. 577-585, August 1968.

7. U.B. Sheorey, I. Lundstrom and E.A. Ash., "Analysis of Punch-Through Injection for a Transit Time Negative Resistance Diode", Int. J. Electronics, Vol. 30, pp. 19-32, January 1971.

8. D.R. Coleman, Jr. and S.M. Sze, "A Low-Noise Metal-Semiconductor-Metal (MSM) Microwave Oscillator", Bell Sys. Tech. J., Vol. 50, pp. 1695-1699, May-June 1971.

9. C.A. Lee and G.C. Dalman, "Local Oscillator Noise in a Silicon Pt-n-p^+ Diode Source", Electron Lett., Vol. 7, pp. 565-566, September 9, 1971.

10. G.T. Wright and N.B. Sultan, "Small-Signal Design Theory and Experiment for the Punch-Through Injection Transit-Time Oscillator", Solid-State Electron., Vol. 16, pp. 535-544, 1973.

11. S.G. Liu and J.J. Risko, "Low-Noise Punch-Through p-n-ν-p, p-n-p and p-n-Metal Microwave Diodes", RCA Review, Vol. 32, pp. 636-644, December 1971.

12. C. Snapp and P. Weissglas,"On the Microwave Activity of Punch-Through Injection Transit-Time Structures", IEEE Trans. Electron Devices, Vol. ED-19, pp. 1109-1118, October 1972.

13. R.T. Davis (editor), "New Low-Noise Mode of Operation Discovered for Silicon Diodes", Microwaves, pp. 9-10, September 1971.

14. K.P. Weller, "Small-Signal Theory of a Transit-Time Negative Resistance Device Utilizing Injection from a Schottky Barrier", RCA Review, Vol. 32, pp. 372-383, September 1971.

15. H.A. Hans, H. Statz and R.A. Pucel, "Noise Measure of Metal-Semiconductor-Metal Schottky Barrier Microwave Diodes", Electron Lett., Vol. 7, pp. 667-668, November 4, 1971.

16. D.J. Coleman, Jr., "Transit Time Oscillations in BARITT Diodes", J. Appl. Phys., Vol. 43, No. 4, pp. 1812-1818, April 1972.

17. P. Antognetti, A. Chiabrena and G.R. Bicio, "Small-Signal Theory of Transit-Time Diodes", Solid-State Electronics, Vol. 16, pp. 345-350, 1973.

18. D.J. Coleman, Jr., J.L. Chu and S.M. Sze, "BARITT Microwave Oscillator Diodes, Large-Signal Analysis", International Electron-Device Meeting, Edmonton, Canada, 1972.

19. E.P. Eer Nisse, "Small-Signal Negative Conductance in BARITT Devices", Appl. Phys. Lett., Vol. 20, No. 8, pp. 301-304, April 15, 1972.

20. M. Matsumura, "Small-Signal Admittance of BARITT Diodes", IEEE Trans. Electron Devices, Vol. ED-19, pp. 1131-1133, October 1972.

21. M. El-Gabaly and P.A. Goud, "On the Temperature Dependence of the Small-Signal Admittance of Punch-Through Injection, Transit-Time Structures, a Paper presented at The 1973 European Microwave Conference, Brussels, Belgium.

22. A. Sjölund, "Small-Signal Analysis of Punch-Through Injection Microwave Devices", Solid-State Electron., Vol. 16, pp. 559-569, 1973.

23. S.M. Sze, D.J. Coleman, Jr., and A. Loya, "Current Transport in Metal-Semiconductor-Metal (MSM) Structures", Solid-State Electron., Vol. 14, pp. 1209-1218, December 1971.

24. J.L. Chu, G. Persky and S.M. Sze, "Thermionic Injection and Space-Charge Limited Current in Reach-Through p^+np^+ Structures", J. Appl. Phys., Vol. 43, pp. 3510-3515, August 1972.

25. D.L. Scharfetter and H.K. Gummel, "Large-Signal Analysis of a Silicon Read Diode Oscillator", IEEE Trans. Electron Devices, Vol. ED-16, pp. 64-77, January 1969.

26. H.K. Henisch, Rectifying Semiconductor Contacts, Chapters 7 and 8, Oxford at the Clarendon Press, Oxford 1957.

27. E. Spenke, Electronic Semiconductors, Chapter 4, McGraw-Hill Book Company, Inc., New York 1959.

28. A.M. Goodman, "Metal-Semiconductor Barrier Height Measurement by the Differential Capacitance Method - One Carrier System", J. Appl. Phys., Vol. 34, pp. 329-338, 1963.

29. H.A. Bethe, "Theory of the Boundary Layer of Crystal Rectifiers", MIT Radiation Laboratory, Report 43-12, 1942.

30. C. Wagner, "Zur Theorie der Gleichrichterwirkung", Phys. Z., Vol. 32, p. 641, 1931.

31. W. Schottky and E. Spenke, Wiss. Veröff a.d. Siemens-Werken, Vol. 18, p. 225, 1939.

32. C.R. Crowell, The Richardson Constant for Thermionic Emission in Schottky Barrier Diodes", Solid-State Electron., Vol. 8, pp. 395-399, 1965.

33. F.A. Padovani, Semiconductor and Semimetals, Application and Devices, Chapter 2, Vol. 7, Part A, Academic Press, New York and London, 1970.

34. S.M. Sze, Physics of Semiconductor Devices, Wiley, New York, 1969.

35. J.R. Macdonald, "Solution of an Idealized One-Carrier Problem", Solid-State Electron., Vol. 5, pp. 11-37, 1962.

36. R. Stratton, "Diffusion of Hot and Cold Electrons in Semiconductor Barriers", Phys. Rev., Vol. 126, pp. 2002-2014, June 15, 1962.

37. W. Schultz, "Zur Theorie der Gleichrichtung am Kontakt Mettall-Halbleiter", Z. Physik, Vol. 138, p. 598, 1954.

38. C.R. Crowell and S.M. Sze, "Current Transport in Metal-Semiconductor Barrier Diodes", Solid-State Electron., Vol. 8, pp. 1035-1048, 1966.

39. C.R. Crowell and S.M. Sze, "Electron-Phonon Collector Backscattering in Hot Electron Transistors", Solid-State Electron., Vol. 8, pp. 673-683, 1965.

40. C.R. Crowell and S.M. Sze, "Electron Optical Phonon Scattering in the Emitter and Collector Barriers of Semiconductor-Metal-Semiconductor Structures", Solid-State Electron., Vol. 8, pp. 979-990, 1965.

41. C.R. Crowell and S.M. Sze, "Quantum Mechanical Reflection at Metal-Semiconductor Barriers", J. Appl. Phys., Vol. 37, pp. 2683-2689, 1966.

42. J.M. Andrews and M.P. Lepselter, "Reverse Current-Voltage Characteristics of Metal-Silicide Schottky Diodes", Solid-State Electron., Vol. 13, pp. 1011-1023, 1970.

43. M. El-Gabaly, J. Nigrin and P.A. Goud, "Stationary Charge Transport in Metal-Semiconductor-Metal (MSM) Structures", J. Appl. Phys., Vol. 44, No. 10, pp. 4672-4680, October 1973.

44. D.L. Scharfetter, "Minority Carrier Injection and Charge Storage in Epitaxial Schottky Barrier Diodes", Solid-State Electron., Vol. 8, pp. 299-311, 1965.

45. M. El-Gabaly and J. Nigrin, "Design Considerations for BARITT Diodes", a Paper presented at The Computers, Electronics and Control International Symposium, Calgary, Alberta, May 1974.

46. H. Statz, R.A. Pucel and H.A. Hans, "Velocity Fluctuation Noise in Metal-Semiconductor-Metal Diodes", Proc. IEEE, Vol. 60, pp. 644-645, 1972.

47. J.L. Moll, Physics of Semiconductors, p. 207, McGraw-Hill, New York, 1964.

48. T.W. Sigmon and J.F. Gibbons, "Diffusivity of Electrons and Holes in Silicon", Appl. Phys. Lett., Vol. 15, No. 10, pp. 320-322, November 15, 1969.

49. F. Stöckman, Halbleiter Probleme, edited by F. Sauter (Vieweg and Sohn, Braunschweig, 1961), p. 298.

50. D. Dascălu, "Trapping and Transit-Time Effects in High-Frequency Operation of Space-Charge Limited Dielectric Diodes", Solid-State Electron., Vol. 11, pp. 491-499, 1968.

51. D. Dascălu, "Space-Charge Waves and High-Frequency Negative Resistance of ScL Diodes", Int. J. Electron., Vol. 25, No. 4, pp. 301-330, 1968.

52. H.Y. Fan, "Theory of Rectification of an Insulating Layer", Phys. Rev., Vol. 74, pp. 1505-1513, 1948.

53. J.P. Kelvey, Solid-State and Semiconductor Physics, Chapter 5, Harper and Row, New York, 1966.

54. H. Lawrence and R.M. Warner, Jr., "Diffused Junction Depletion Layer Calculations", Bell Syst. Tech. J., Vol. 39, pp. 389-403, 1960.

55. K.G. Breitschwerdt, "Characteristics of Diffused P-N Junctions in Epitaxial Layers", IEEE Trans. Electron Devices, ED-12, pp. 13-19, 1965.

56. J.J. Sparkes, "A Reappraisal of Certain Aspects of Transistor Theory", J. Electron. Control, Vol. 16, pp. 153-168, 1964.

57. J.F. Holt, "Numerical Solution of Nonlinear Two-Point Boundary Problems by Finite Difference Methods", Communications of the A.C.M., Vol. 7, pp. 366-373, 1964.

58. D.D. Morrison, J.D. Riley and J.F. Zancanaru, "Multiple Shooting Method for Two-Point Boundary Value Problems", Communications of the A.C.M., Vol. 5., pp. 613-614, 1962.

59. J.H. Ahlberg, E.N. Nilson and J.L. Walsh, The Theory of Splines and Their Applications, Chapters 2 and 3, Academic Press, New York, 1967.

60. T.N.E. Greville, Mathematical Methods for Digital Computers, Vol. II, Chapter 8, John Wiley, New York, 1967.

61. P.B. Bailey, L.F. Shampine and P.E. Waltman, Non-Linear Two Point Boundary Value Problems, Chapter 8, Academic Press, New York, 1968.

62. F.B. Llewellyn, Electron Inertia Effects, Cambridge, 1941.

63. G.T. Wright, "Transit-Time Effects in the Space-Charge Limited Silicon Diode", Solid-State Electron., Vol. 9, pp. 1-6, 1966.

64. H. Kroemer, "Detailed Theory of the Negative Conductance of Bulk Negative Mobility Amplifiers, in the Limit of Zero Ion Density", IEEE Trans. Electron Devices, ED-14, pp. 476-492, 1967.

65. T. Misawa, "Negative Resistance on p-n Junction Under Avalanche Breakdown Conditions, Part I and II", IEEE Trans. Electron Devices, ED-13, pp. 137-151, 1969.

66. C. Canali, G. Ottaviani and A.A. Quaranta, "Drift Velocity of Electrons and Holes and Associated Anisotropic EFfects in Silicon", J. Phys. Chem., Vol. 32, pp. 1707-1720, 1971.

67. H.K. Gummel, "A Self-Consistent Iterative Scheme for One-Dimensional Steady-State Transistor Calculations", IEEE Trans. Electron Devices, Vol. ED-11, pp. 455-465, 1964.

68. A. De Mari, "An Accurate Numerical Steady-State One-Dimensional Solution of the P-N Junction", Solid-State Electron., Vol. 11, pp. 33-58, 1968.

69. S. Gill, "A Process for the Step-by-Step Integration of Differential Equations in an Automatic Computing Machine", Proc. Cambridge Phil. Soc., Vol. 47, pp. 96-108, 1951.

70. Brice Carnahan, H.A. Luther and James O. Wilkes, Applied Numerical Methods, Chapter 6, Wiley, New York, 1969.

71. P. Henrici, Discrete Variable Methods in Ordinary Differential Equations, Wiley, New York, 1962.

72. L. Fox (editor), Numerical Solution of Ordinary and Partial Differential Equations, Addison-Wesley. Reading, Massachusetts, 1962.

73. F.B. Hildebrand, Introduction to Numerical Analysis, McGraw-Hill, New York, 1953.

74. L. Collatz, The Numerical Treatment of Differential Equations, Third Edition, Springer-Verlag, Berlin, 1960.

APPENDIX A

ACCURACY AND STABILITY OF THE NUMERICAL SOLUTION (USING THE INITIAL-VALUE METHOD)

One of the most important questions about any numerical method is its accuracy. Different numerical schemes have been devised for solving the transport equations in semiconductors [e.g. 67, 68, 25, 35]. Most of these methods are based on finite-difference techniques which involve the approximation of boundary value problems. Using the finite-difference method, we replace the boundary value problem (the dc problem discussed in section 5.3) for the unknown function $p(x)$ $[E(x)]$ of the continuous variable x by a "corresponding" problem for an unknown function P_j (or E_j) of the discrete variable j in the following way: Replace x in Eqs. 5.1 and 5.2 by x_j, $p(x)$ by $P_j(E_j)$ and the differential operator $(\frac{d}{dx})$ by the difference operator Δ. Thus the continuous problem (Eqs. 5.7 and 5.8) is replaced by a discrete one. The discrete problem is simply a set of (N-1) albegraic equations in (N-1) unknowns, where N is the number of points dividing the total width L. If the boundary-value problem is linear then the system of algebraic equations is also linear, and its solution can be easily found. If the original problem is non-linear, then the corresponding discrete problem (the system of algebraic equations) is also non-linear, and its solution is more difficult than the linear case. The charge-transport equations in semiconductors are generally non-linear differential equations; therefore, the

corresponding system of algebraic equations is non-linear. The solution of the non-linear charge transport problem by finite difference technique may be very difficult especially when many base points (required for accurate solution) are used.

In bipolar charge transport devices, initial value methods (which are easier to use) are usually unstable while finite-difference methods have proven to be extremely stable and hence are usually used. In unipolar charge transport devices on the other hand, stable solutions can be found by using initial-value methods. Initial-value techniques (e.g. Runge Kutta, Euler method, ... etc) have the advantage over the finite difference approach, that no special procedure is required in the programming and hence it is easier to use. The accuracy of any numerical method depends mainly on the step-size interval of integration. Step-size can be easily changed during the course of integration procedure in the case of one-step methods while it is a difficult task and requires special treatment in finite difference methods.

The main disadvantage in the RK fourth order method (used in this study) is that the time of computation involved in the frequent computation of the derivatives may be lengthy; however, for the type of equations used here and by the use of fast computing machines this difficulty does not exist in our case. More fundamental is the difficulty of estimating the local truncation error at each step, since its formal expression (for RK fourth order algorithm) is excessively complicated. Associated with the error is the problem of determining a suitable step size interval and of changing it in the course of the computation in such a way that

the truncation error remains negligibly small at an economic interval.

To ensure that the main source of errors is the truncation error, the round-off error is almost eliminated by using double precision and by excluding the round-off error made in the preceding step in the calculations of the next step (this is obtained by using the RK algorithm modified by Gill [69]). The step size control, is obtained by assuming that the local truncation errors have the form $k\,h^5$ with k being constant and h the step size. Furthermore, the local truncation error, committed in traversing one step dominates the change in the total error for the step. Then an estimate of the local truncation error can be found by integrating between two points say x_n and x_{n+1}, using two different step sizes h_1 and h_2 to evaluate Y_{n+1}. Let the corresponding solutions be $Y_{n+1,1}$ and $Y_{n+1,2}$, then if Y^*_{n+1} is the true solution, and by using Richardson extrapolation technique [70], we have

$$Y^*_{n+1} - Y_{n+1,1} = kh_1^5 \frac{(x_{n+1}-x_n)}{h_1} \qquad (A.1)$$

$$Y^*_{n+1} - Y_{n+1,2} = kh_2^5 \frac{(x_{n+1}-x_n)}{h_2} \qquad (A.2)$$

In Eqs. A.1 and A.2, the righthand sides are the total error estimate for the integration between x_n and x_{n+1}. The total error is equal to the error per step (local error) multiplied by the number of steps, i.e.

$$E_{n1} = kh_1^5 n_1 = kh_1^5 \frac{(x_{n+1}-x_n)}{h_1}$$

and $$E_{n2} = kh_2^5 n_2 = kh_2^5 \frac{(x_{n+1}-x_n)}{h_2}$$

Dividing Eq. A.1 by Eq. A.2 and solving for Y^*_{n+1} yields

$$Y^*_{n+1} = \frac{Y_{n+1,1} - Y_{n+1,2}(h_1/h_2)^4}{1 - (h_1/h_2)^4} \qquad (A.3)$$

If we choose $h_2 = \frac{h_1}{2}$, Eq. A.3 becomes

$$Y^*_{n+1} = \frac{Y_{n+1,1} - 2^5 Y_{n+1,2}}{(1 - 2^5)} \qquad (A.4)$$

and an estimate of the local truncation error for the solution $Y_{n+1,1}$ assuming $x_{n+1} - x_n = h_1$ is given by Eqs. A.1 and A.3 as

$$e_t = kh_1^5 = \frac{2^4(Y_{n+1,2} - Y_{n+1,1})}{2^4 - 1} = \frac{16}{15}(Y_{n+1,2} - Y_{n+1,1})$$

(A.5)

Equation A.5 may be used in the numerical method, for automatic step-size control, by setting an upper limit to the maximum permissible truncation error as input. Unfortunately, by using Eq. A.5 as a monitoring procedure for the integration step size on every integration interval and for each iteration process, the total number of calculations is approximately trebled for each iteration over the number required for integration using just one step size. As a compromise, the monitoring procedure can then

be modified by checking the error less frequently, for instance, for every k^{th} step.

Another criterion for adjusting the step-size, is to integrate backwards, i.e., from x_{n+1} to x_n with h replaced by -h after having integrated across the step in the forward direction. The truncation error is estimated as half the difference between Y_n and Y_n^*, where Y_n^* is the solution found as a result of the reverse integration. Unfortunately, the method fails for the fourth order method used here, since the truncation errors in one direction exactly cancel those in the other direction, aside from the round-off errors, $Y_n = Y_n^*$. Finally, it is shown [71] that all RK methods are convergent to the true solution, i.e., $\lim_{h \to o}(Y_i - Y(x_i)) = 0$ where $Y(x_i)$ is the true value x_i and Y_i is the numerically estimated value at the same point [71].

Another important criterion for selecting an algorithm for the solution of a differential equation or system of equations with given initial conditions is its stability. Stability is a somewhat ambiguous term and it appears in the literature with a variety of qualifying adjectives (inherent, partial, relative, weak, strong, absolute, etc.). In general, a solution is said to be unstable if errors introduced at some stage in the calculations (e.g. from erroneous initial conditions or local truncation error or round-off errors) are propagated without bound through subsequent calculations.

The general solution of a system of linear or non-linear differential equations is always of exponential nature. Certain

equations with specified initial conditions cannot be solved by any step-by-step integration procedure without exhibiting instability, and are said to be inherently unstable. For example, consider Eq. 4.7,

$$\frac{dp}{dx} = v\,p(x) - J \qquad (A.6)$$

For simplicity we have assumed that v is constant (which is nearly true in the high field region, where the velocity approaches scattering limited velocity). The analytical solution of Eq. A.6 has the form

$$p(x) = e^{vx}[c + \frac{J}{v} e^{-vx}] \qquad (A.7)$$

where c is the constant of integration. With the initial condition $p(x_0) = p_0$ at $x = x_0$, Eq. A.7 becomes

$$p(x) = (p_0 - \frac{J}{v})e^{v(x-x_0)} + \frac{J}{v}, \quad x_0 \leq x < L \qquad (A.8)$$

If $p_0 = \frac{J}{v}$ (A.9)

then the analytical solution of Eq. A.3 reduces to

$$p(x) = \frac{J}{v} \qquad (A.10)$$

Consequently, the exponential term in the general solution (Eq. A.8) vanished because of the particular choice of the initial condition

(note that the initial condition as given by Eq. A.9 is a typical condition in the high field region where the drift current is approximately equal to the total conduction current). Even a very tiny change in the initial condition will eventually cause a drastic change in the magnitude of the solution for large values of x. Therefore, even though the multiple of the exponential term is quite small, the contribution of the exponential term will eventually swamp the contribution of the constant term in the solution. When such an equation is solved by using step-by-step methods, each new step can be regarded as the solution of a new initial value problem. Even if the initial condition is error free in the first step, the initial conditions for the subsequent steps will inevitably contain errors introduced by truncation and round-off in the preceding steps; the calculated solution for large x will bear no resemblance to the true solution. If the initial conditions are chosen at x = L, on the other hand, the solution of Eq. A.7 is now given by

$$p(x) = \left(p_o(L) - \frac{J}{v}\right)e^{-v\,(L-x)} + \frac{J}{v} \qquad x < L \quad (A.11)$$

From Eq. A.11, if any error is introduced at the initial or subsequent steps, the solution p(x) becomes extremely stable under any choice of initial condition because of the exponentially decaying term. In other words, the total errors incurred during the integration procedure will be limited to those made at each step and no propagation of errors from one step to another will take place.

Hence, inherent instability is associated with the equations being solved and the initial conditions specified, but does not depend on the particular algorithm being used. Depending on the equations being solved, their initial conditions and the particular step-by-step method being used, another form of instability, "partial instability" [72], may be observed, even when the solution is not inherently unstable. This phenomena is related to the step size chosen and is perhaps seen most easily by examining the Euler algorithm [63]. The total error ε_{i+1} (Euler's method) at x_{i+1} is related to the total error, ε_i at x_i by

$$\varepsilon_{i+1} = \varepsilon_i + h[f(x_i,y_i) - f(x_i,y(x_i)] - \frac{h^2}{2} f'(\xi,y(\xi)) \qquad (A.12)$$

where $x_i < \xi < x_{i+1}$, $\frac{dy}{dx} = f(x,y)$ and $f' \equiv \frac{\partial f}{\partial x}$. From the differential mean-value theorem [70], we have

$$f(x_i,y_i) - f(x_i,y(x_i)) = (Y_i - Y(x_i)) \left.\frac{\partial f}{\partial y}\right|_{x_i,\alpha}$$

with α in $(y_i,y(x_i))$. Since $[y_i - y(x_i)]$ is just ε_i, Eq. A.12 may be written as

$$\varepsilon_{i+1} = \varepsilon_i\left(1 + h \left.\frac{\partial f}{\partial y}\right|_{x_i,\alpha}\right) - \frac{h^2}{2} f'(\xi,y(\xi)) \qquad (A.13)$$

with $\xi\varepsilon(x_i,x_{i+1})$ and $\alpha\varepsilon(y_i,y(x_i))$.

The first term on the right hand side of Eq. A.13 is the contribution of the propagated error to the error at x_{i+1}, while the second term is the local truncation error. Clearly, if $\frac{\partial f}{\partial y}$ is negative, then a value of positive h can always be found which will make $[1 + h(\frac{\partial f}{\partial y})] < 1$, and the error tends to diminish or die out, and hence the solution will be stable. If $[1 + h(\frac{\partial f}{\partial y})] > 1$, i.e. for $\frac{\partial f}{\partial y}$ and h are positive, the error at x_i will be amplified in traversing the i^{th} step and the solution will tend towards instability. Even in this case, however, it may be possible to keep the propagation error under control, by keeping the propagation factor $[1 + h(\frac{\partial f}{\partial y})]$ close to unity.

Applying the preceding argument on Eq. 4.7, we have

$$\frac{\partial f}{\partial y} = v'$$

and the propagation factor is $(1 + hv)$. In the injection region, v is non-positive quantity, hence a positive h makes the propagation factor less than unity and no propagation of errors takes place resulting in a stable solution under forward integration in this region. Beyond the injection region $x_m < x$ the velocity v becomes positive, hence the propagation factor exceeds unity. Consequently, the error at subsequent integration steps will be amplified resulting in an unstable solution. For backward integration on the other hand, h is negative which makes the propagation factor less than unity and the propagation error tends to diminish and the solution will be stable. In the injection region, the carrier

velocity is negative and the propagation factor (1 + hv) is larger than unity. In this region, the error will have the tendency to grow exponentially. However, it is possible to keep the propagation error under control by choosing a sufficiently small h that keeps (1 + hv) close to 1. Since the solution is an exponentially increasing function of position, in the injection region, the important criterion is not the absolute error ε_i to be bounded but that the relative error $\frac{\varepsilon_i}{y_i}$ not to grow appreciably. The error can be made extremely small in the injection region by reducing h which is always possible since the injection region is only a small fraction of the total semiconductor width.

Similar, though more complicated propagation factors can be developed for higher order one-step methods (e.g. Runge Kutta fourth order algorithm [73]). The quantity $(h \frac{\partial f}{\partial y})$, sometimes called the step factor, contributes to these propagation factors in a manner comparable to that of Euler's method. Collatz [74] suggests that the step factor be kept essentially constant during the course of integration, leading to another method of controlling the step size.

In view of the above discussions, backward integration of the system of equations (5.1) - (5.3) for the dc and small-signal cases has been used here. The solutions have proven to be extremely stable. The accuracy is checked less frequently by using Eq. A.5, and the solution in the injection region has been extensively examined to obtain an estimate for the relative, rather than absolute error. The present author would like to point out that forward integration procedure might be possible, by keeping the step factor

$(h \frac{\partial f}{\partial y})$ very small through the total integration interval. However, h in this case will be excessively small and will result in extremely large computing time.